Feasibility of Prosthetic Knee Construction using 3D Printed Lattice Structures

Timothy Long Moser

(Student number: 2513593)

School of Mechanical, Industrial and Aeronautical Engineering

University of the Witwatersrand

Johannesburg, South Africa.

Supervisors:

Taahirah Mangera

Dean Van Aswegen

An investigational research project submitted to the Faculty of Engineering and the Built Environment, University of the Witwatersrand, in partial fulfilment of the requirements for the degree of Master of Engineering.

31 January, 2022

PLAGIARISM DECLARATION FOR HIGHER DEGREE STUDENTS

I, _____Timothy L Moser_____ (Student number: _____2513593_____)
am a student registered for the degree of MEng Professional (ECA05), in the year __2021_____.

I hereby declare the following:

- I am aware that plagiarism (the use of someone else's work without their permission and/or without acknowledging the original source) is wrong.
- I confirm that ALL the work submitted for assessment for the above course is my own unaided work except where I have explicitly indicated otherwise.
- I have followed the required conventions in referencing the thoughts and ideas of others.
- I understand that the University of the Witwatersrand may take disciplinary action against me if there is a belief that this in not my own unaided work or that I have failed to acknowledge the source of the ideas or words in my writing.

Signature:  Date: 31 January 2022

ABSTRACT

The World Health Organization (WHO) estimated in 2005 that 30 million people in the developing world need a prosthetic. Estimates indicate this figure will double by 2050, yet only 5% of amputees have access to prosthetic options [1,2]. With nearly one in five South African citizens currently living below the international poverty value of R28.27 a day [3] (approximately $1.90) it can be assumed that there is a significant need within the country for low-cost, lower-limb prosthetics.

Through the development 3D printed prosthetics, the amputee community has received bespoke, low-cost devices in turn improving quality of life. Through open-source sharing, 3D printing volunteers around the world have produced 3D printed prosthetics and have enabled individuals in developing countries to regain functionality, mobility, and to assimilate into their communities. However, current research of a 3D printed prosthetics is focused on feet, arms, and hands while 3D printed knee joint (PKJ) solutions are limited.

In this research report, a low-cost, single-axis PKJ is designed specifically for fused filament fabrication (FFF) 3D printing and implements a conformable lattice structure. Literature review was performed to outline design considerations that must be met when developing a PKJ and identifies best practices for FFF 3D printing. The PKJ assembly was first modeled in Autodesk Fusion 360 software for both visualization and dimensioning of the design. nToplogy software was utilized to generate lattice structures within the PKJ and was used to characterize the lattice by its stiffness. The characterization model allows for specific optimization of the lattice parameters based off the user's weight to create structure properties such as responsive or cushioned.

Furthermore, this report simulated the designed PKJ against industry load requirements and experimentally tested 3D printed prototypes. Simulation data indicated no part failure, however, experimental testing of the 3D printed parts demonstrated failures unforeseen through simulation via layer delamination and bolt shear tear-out. This report demonstrated successful fabrication of complex lattice structures via FFF 3D printing despite the relative manufacturing limitations of FFF when compared to other 3D printing processes.

While this research project's designed PKJ failed to meet performance requirements, this report serves to transfer knowledge and motivate the prosthetic research community to develop a PKJ that can be produced with a low-cost desktop printer.

TABLE OF CONTENT

LIST OF FIGURES

LIST OF TABLES

LIST OF ABBREVIATIONS

Abbreviation	Explanation
ABS	Acrylonitrile Butadiene Styrene
CAD	Computer Aided Design
DFAM	Design for Additive Manufacturing
FOS	Factor of Safety
FEM	Finite Element Methods
FFF	Fused Filament Fabrication
F_{SU}	Ultimate Static Test Force
PKJ	Prosthetic Knee Joint
PLA	Polylactic Acid
R	Currency: South African Rand
ROM	Range of Motion
SLA	Stereolithography
SLS	Selective Laser Sintering
TPMS	Triply Periodic Minimal Surface
TPU	Thermoplastic Polyurethane
UTM	Universal Test Machine

1. RESEARCH BACKGROUND/CONTEXT

1.1 Amputees Demographic

It is estimated that less than every 30 seconds an amputation occurs worldwide [4]. In South Africa, the current number of amputees has not been determined. However, the World Health Organization (WHO) estimated in 2005 that 30 million people in the developing world need a prosthetic. Estimates indicate this figure will double by 2050, yet only 5% of amputees have access to prosthetic options [1,2]. Of this estimate, which does not include individuals born without limbs (a condition referred to as "Amelia"), 90% of amputees suffer lower-limb loss. With nearly one in five South African citizens currently living below the international poverty value of R28.27 a day [3] (approximately $1.90) it can be assumed that there is a significant need within the country for low-cost, lower-limb prosthetics.

The cause of amputations in developing countries can often be traced back to low-income citizens being exposed to traumatic situations such as: dangerous labor conditions, vehicular trauma from hazardous transportation, or untreated infection from lack of health care [5]. Despite developing countries composing a significant portion of the amputee demographic, the prosthetic industry promotes expensive devices. The cost of a commercial prosthetic leg, which includes a PKJ, ranges from R74,400 to over R744,000 (approximately $5,000 to $50,000) [6]. At R74,400, a person living on R28.27 a day would be required to invest all their income for seven years to afford the prosthetic. This estimate does not include costs for physical therapy, fitting consultations, and is not realistic when most devices are manufactured for only three to five years of use [6].

Conversely, if one forgoes the financial burden of owning a prosthetic, they are faced with social stigma. In 2018, Brigitte Rohwerder [6], a research officer for the Institute of Development Studies, published *Disability stigma in developing countries* stating that in "many cultures, one's human status is judged by the extent to which people can participate in valued activities within that society." Furthermore, "such [people with disabilities] are not only seen as a financial and resource liability within their own family but also by the larger community resulting in shaming and isolation" [8]. From birth, a physically impaired person experiences unwarranted exclusion because their worth is determined by their physical capacity. There are deep-rooted beliefs that disabled individuals cannot contribute to society and therefore they are not supported by the community to develop independence.

While prosthetics are known as a mobility device with residual effects for emotional healing, they

can also act as protective devices, allowing for individuals to assimilate. Janet Njelesani's [9], an Assistant Professor in the Department of Occupational Therapy, published interviews from Guinea community leaders stating "children with disabilities are victims of several types of abuse: they are beaten in the streets, they are ridiculed and rejected not only by their peers but also by some adults" [9]. However, Njelesani's findings iterate that physically impaired children that could utilize a mobility aid "were thought to experience less violence in Niger and Togo." The addition of a prosthetic, particularly for lower limbs, is vital in developing countries to provide individuals with independence. The ability to perform simple tasks such as walking to a job, carrying food, or visiting a neighbor enables the disabled to integrate into their community.

1.2 Prosthetics Knee Joint

A prosthetic knee joint (PKJ) is required for transfemoral amputees to walk with a proper gait and efficient locomotion. The functionality and cost of a PKJ can be grouped into three major categories with price increasing respectively: monocentric, polycentric, and bionic. Polycentric knees and bionic knees contain ability to move in multiple planes of direction, whereas a monocentric (single-axis) knee can only pivot in one direction [10]. While the prosthetic industry has captured life-like movement through advanced R365,000 (approximately $25,000) bionic knees utilizing microprocessors, most low-income individuals will be restricted to the single-axis knee beginning in price around R1,460 (approximately $100) [11,12].

The single-axis PKJ is the simplest and most affordable design, allowing the knee to hinge around a single-axis based on the user's stance. Since the single-axis PKJ consists of less parts compared to the polycentric and bionic knees, the design offers lightweight, durability, and reduced size [10]. Some single-axis knees consist of pneumatics, hydraulics, or springs which allow for the knee swing-rate to be modified during flexion and extension. Most amputees in developing countries acquire single-axis knees that swing freely without rate-control. Figure 1-1 displays a common single-axis knee found in India:

Figure 1-1. A monocentric (single-axis) knee displayed by Krista Donaldson, CEO of D-Rev [13].

When bent, the shape of the single-axis knee shown in Figure 1-1 resembles the bent human knee, yet anatomical similarities such as stability, smooth locomotion, and proper posture are not always present. While affordable, this single-axis knee sacrifices the user's experience with potentially hazardous situations and has been identified in independent studies as requiring significant improvements to be a viable option [14]. The goal of providing functional prosthetics to those restrained by income has been spearheaded primarily not by the prosthetic industry but rather hobbyist, non-profits, and researchers with 3D printers.

1.3 Additive Manufacturing

Additive manufacturing, commonly known as 3D printing, "grows" 3-dimensional objects by stacking thin cross-sectional layers of material varying from plastic to rubber to titanium [15]. Additive manufacturing differs from conventional manufacturing which subtracts material from a body of material using dedicated machinery, like a sculptor removing material to reveal a statue. Within the category of additive manufacturing there are numerous types of printers that vary in operation, material, and application; however, the most common process is fused filament fabrication (FFF) [16].

FFF is the process of melting thermoplastic filament through a nozzle to build a part layer by layer demonstrated in Figure 1-2. FFF is accessible to consumers due to its low-cost and the availability of desktop 3D printers that support the operation (see Figure 1-3). As a result, online open-source websites, such as e-Nable and Thingiverse, focused on sharing FFF prosthetics designs have been

enacted. This research project will also design for FFF to create a PKJ whose manufacturing method aligns with majority of 3D printer users.

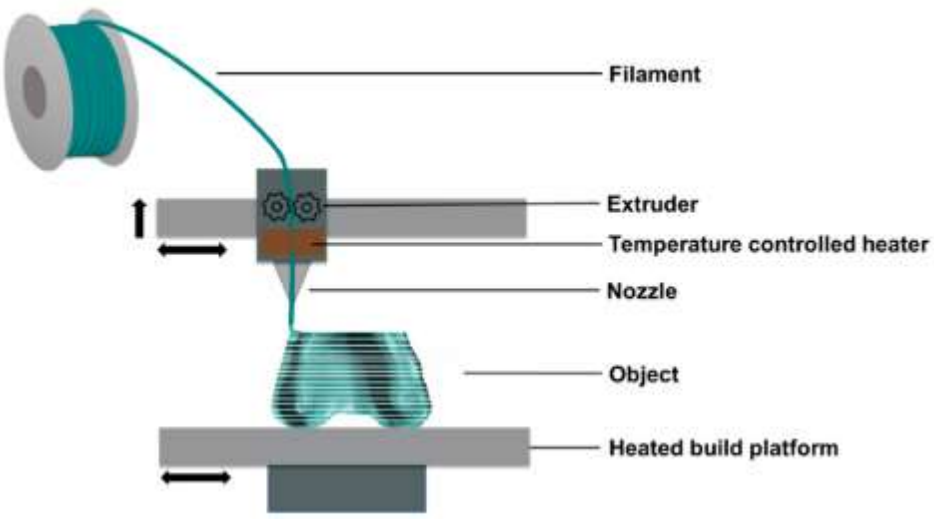

Figure 1-2. Diagram of additive manufacturing fused filament fabrication [17].

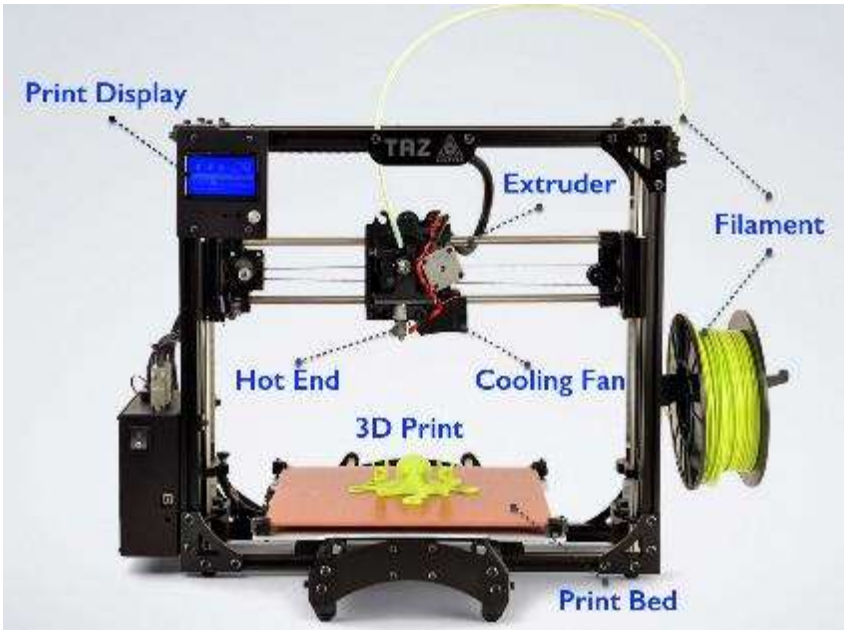

Figure 1-3. Diagram of desktop 3D printer components [18].

1.3.1 Additive Manufacturing: Prosthetics

In 2011, the prosthetic industry was revolutionized by 3D printing when mechanical specialist Ivan Owen, of the United States, was contacted by Richard Van As, of South Africa, with hopes to restore dexterity of his four severed fingers [19]. The goal was to replace Van As's homemade wooden

fingers with mechanical fingers, but the global collaboration was not made possible until the pair utilized 3D printing. Through computer aided design (CAD) the pair was able to instantaneously share design concepts through the internet and rapidly prototype the prosthetic [20]. The final product became famously known as Robohand and caught worldwide attention of researchers, medical professionals, and hobbyist printers alike. Since 2011, the 3D printing community has propelled the innovation of low-cost 3D printed prosthetics (see Figure 1-4) of which can be downloaded from open-source websites for free [21].

Figure 1-4. 3D printed Raptor Hand Reloaded designed by e-NABLE [22].

1.3.2 Additive Manufacturing: Lattice Structures

Recent research in fields parallel to human prosthetics have successfully implemented the use of 3D printed lattice structures due to their deformation and elasticity. Bionic Pets, a company specialized in animal prosthetics, previously manufactured canine feet by heating and bending plastic or rubber. The company states that aside from taking "too much time to fabricate," the handmade product would often break [23]. The transition to 3D printing now allows the company to save the design file of each product, analyze the structural strength, and customize dimensions easily. The implementation of 3D printing most notably allowed the company to utilize lattice structures (see *Figure 1-5*) providing increased energy return in comparison to previous products [23].

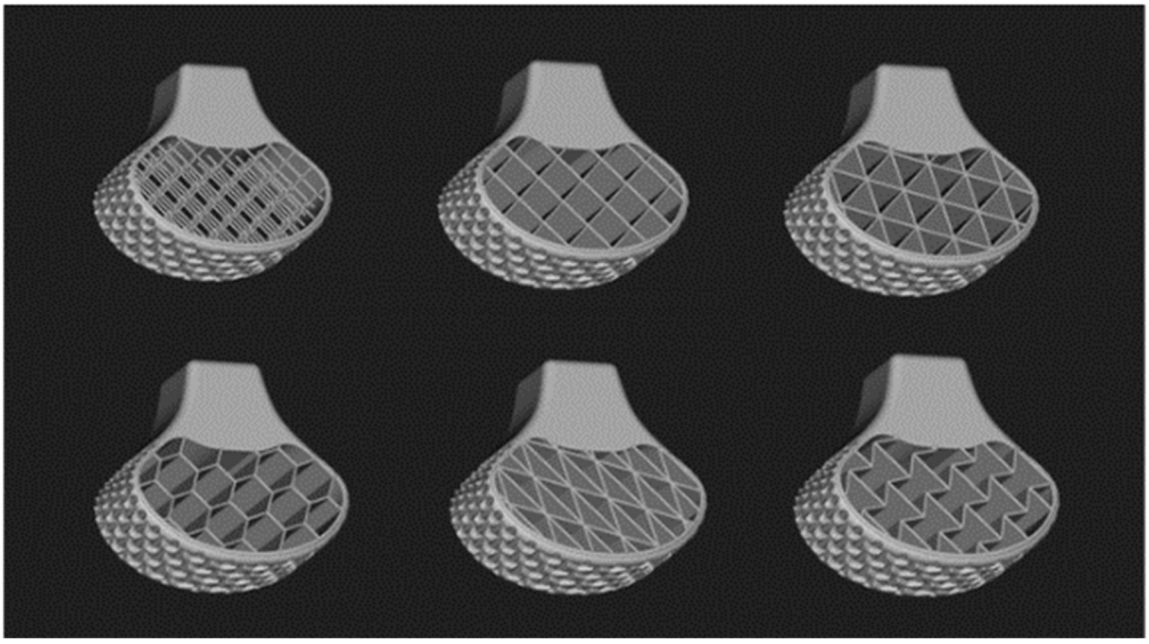

Figure 1-5. Iterations of canine prosthetic feet design with nTopology software *[23]*.

Similarly, additive manufacturing company Carbon collaborated with foot ware company Adidas to produce a novel midsole which utilizes 3D printed lattice structures of varying scale throughout the shoe's sole (see Figure 1-6). The implementation of additive manufacturing removed traditional manufacturing limitations and consolidated the shoe midsole from multiple parts of varying density to one monolithic structure, thus decreasing production and supply chain costs. Carbon states the collaboration enables tuned "cushioning properties throughout the shoe, and ultimately provide bespoke athletic footwear" [24].

Figure 1-6. Varied lattice structure used in Adidas monolithic midsole [24].

Both Bionic Pets and Adidas's collaboration with Carbon demonstrates 3D printing's ability to shift manufacturing away from conventional methods resulting in enhanced performance, customizability, and inspires the question of what traditional products can be redesigned with 3D printed lattices.

1.4 Low-Cost Manufacturing Methods

Injection molding and additive manufacturing are manufacturing methods used to produce complex parts at a low-cost. Injection molding is a standard in the manufacturing industry for making complex, high-quality, high-volume parts. Since both injection molding and additive manufacturing can efficiently produce anatomical geometries required for prosthetics, an evaluation must occur to determine the feasibility of implementing each process within developing countries.

Determining which method is selected involves discussion of initial cost, production volume, and design customizability. Figure 1-7 below, cited from *The International Journal of Advance Manufacturing Technology,* provides "break-even analysis" in which the cost of each process is compared against produced units [25]:

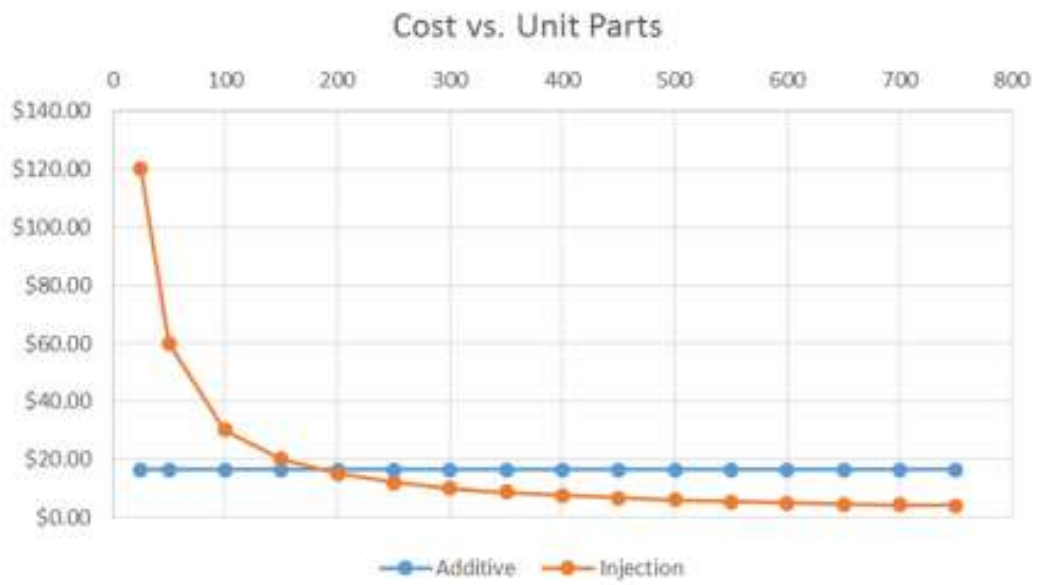

Figure 1-7. Cost vs Unit Part analysis for additive manufacturing and injection molding [25].

Figure 1-7 displays that at cost lower than additive manufacturing, injection molding is able to produce a high volume of parts, however, the implementation of injection molding requires the purchase of a large operating facility and specialized machinery ranging from R87,500 to R4,370,000 (approximately $6,000 to $300,000). [25]. As a result of high initial cost, design firms cannot afford their own injection molding equipment and contract their work to outside companies. In contrast, 3D printing machines, such as the MakerBot Replicator 2 used to develop RoboHand discussed in Section 1.3.1 [26], can be acquired for less than R14,900 (approximately $1,000), and operate fully from an office desktop. The impact of injection molding requiring fixed equipment and a supply chain is emphasized when a design requires iteration.

Injection molded products require custom metal molds of which molten plastic fills and conforms to the cavity as it cools. This is efficient for when large batches of parts need to be replicated, however, inefficient if a part needs modification, such as rescaling a prosthetic. For each design iteration, a unique mold must be manufactured, often by a supplier specialized in tooling before the injection molding can occur. This modification to design not only costs thousands of dollars just for the mold but also delays production schedule. In contrast, 3D printing caters to the bespoke geometry of the human body through rapid prototyping. Designs can be modified with computer software and be sent directly to a 3D printer to begin production. In the instance of a child needing a 3D printed hand, the purchase of a 3D printer and production of one hand (or multiple rescaled hands as the child grows) could be significantly cheaper than any other option and would fulfil the amputee's need.

Despite a 3D printer having lower production volume than an injection molding machine, 3D printing's ease of implementation has allowed for manufacturing services and independence in communities that otherwise would have none. The omission of expensive factories and supply chains allow communities to "locally manufacture products with 3D printing (LM3D)…[this] could result in lower costs, shorter delivery times, and the ability to customize products to unique settings" [27]. 3D printing's ability to provide relief to areas that cannot acquire industrial production facilities has been emphasized during the COVID19 pandemic. The rapid installation of 3D printers in hospitals and communities mitigated a shortage of personal protective equipment through the non-centralized production of millions of 3D printed devices [28].

This research investigation focuses on the design of a 3D printed PKJ with intentions of helping developing communities become closer to manufacturing PKJs without reliance on industrial knowledge or facilities.

2. PROPOSED RESEARCH

2.1 Problem Statement / Motivation

The prosthetic market is largely composed of low-income amputees that cannot afford the most basic prosthetics offered and are sometimes forced to use a bamboo cane in place of a prosthetic leg [11]. Since 2011, the field of prosthetics has experienced a surge of innovation worldwide replacing high-end devices with 3D printed solutions at a fraction of the price. Through open-source development, professionals and hobbyists alike have collaborated and produced innumerable prosthetic designs. Along with the creation of the first 3D printed hand, inventor Ivan Owen continued supporting developing communities through the creation of non-profit organization e-Nable [29]. These prosthetics are produced on consumer desktop printers by fused filament fabrication (FFF). However, researchers in the field of prosthetics, who develop 3D printed designs, have focused primarily on hands, arms, and feet without many advancements of the prosthetic knee joint (PKJ).

The price of a PKJ unquestionably excludes individuals living in poverty from obtaining proper aid and is a financial burden to non-profit organizations seeking to donate. In addition to the PKJ serving as a vital rehabilitation tool for amputees to regain walking ability [30], a PKJ presents an amputee with the ability to assimilate into society through independence. Functional 3D printed hands, arms, and feet have demonstrated positive impacts in developing countries due to high accessibility and low-cost.

A search of website Thingiverse, a 3D printing open-source library, provides thousands of free prosthetic hand designs with attributes such as integration for robotics and growth with children, but a similar search for PKJs results in no accessible designs [31]. Despite an influx of low-cost prosthetic feet, transfemoral (above the knee) amputees are still left immobile and unable to obtain a PKJ required to complete their prosthetic leg. While there have been some developments in producing low-cost PKJs (see Section 2.4.6), these researchers do not utilize 3D printing or the associated benefits that made other prosthetics accessible to all. The addition of a low-cost PKJ would allow transfemoral amputees to make use of prior research and innovations of the prosthetic foot. Developing a PKJ design specific for 3D printing will have positive effects on both amputees in need and advancing the prosthetic research community.

2.2 Critical Research Question (CRQ)

The aim of this research is to design a PKJ for manufacturing on a desktop FFF 3D printer while evaluating the feasibility of implementing 3D printed lattice structures within the PKJ. This research in turn will promote a low-cost PKJ design without compromise to functionality that can be produced by the decentralized 3D printing community.

The critical research question for this research project are:

1. How can the single-axis PKJ with a lattice structure be redesigned for a FFF, desktop 3D printer?

2.3 Research Objectives

The objectives of this research are to:

1. Develop a suitable single-axis PKJ design which can be 3D printed via FFF and includes a suitable lattice structure.
2. Characterize the performance of a 3D printed single-axis lattice PKJ design through FEA simulation and mechanical testing according to ISO 10328:2016.
3. Discuss feasibility for the 3D printed single-axis lattice PKJ with respect to cost and FFF manufacturability.

2.4 Literature Review / Design Considerations

2.4.1 Lattice Structures and Fused Filament Fabrication

3D printed lattice structures are designed based off their cell geometries, which govern the mechanical properties of the entire structure. Figure 2-1 defines the components of a 3-dimensional beam lattice structure of which the beam orientation, size and shape can be modified to change the cell.

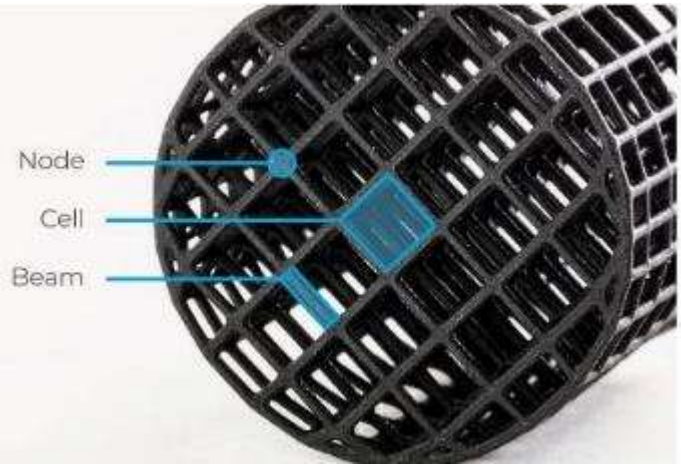

Figure 2-1. Components of 3 Dimensional Lattice Structure [32].

Alternatively, to beamed structures, lattices can be a 2-dimensional structure opting for solid walls (see Figure 2-2) or a 3-dimensional triply periodic minimal surface (TPMS) (see Figure 2-3). A TPMS unit cell can vary in wall thickness as shown in Figure 2-4.

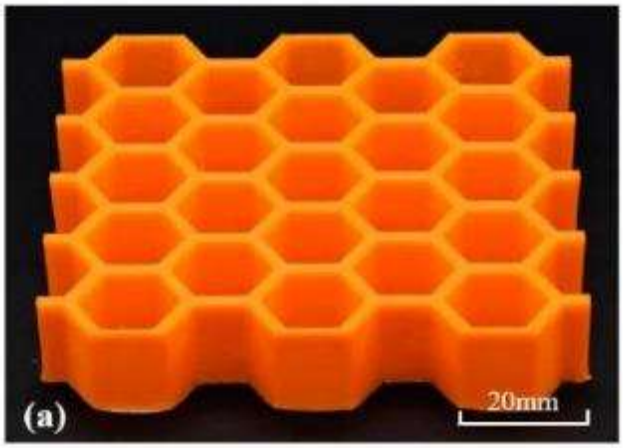

Figure 2-2. 2-dimensional honeycomb lattice structure [33].

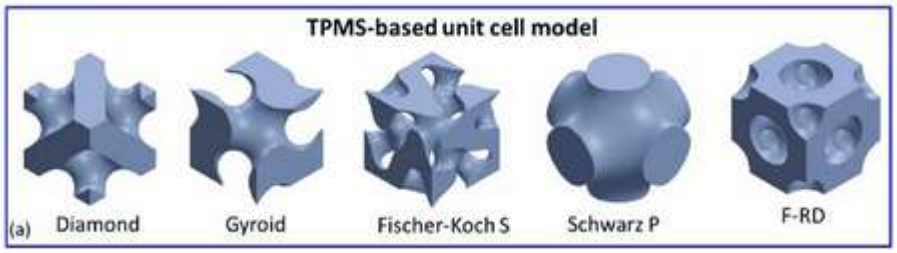

Figure 2-3. TPMS unit cell examples [34].

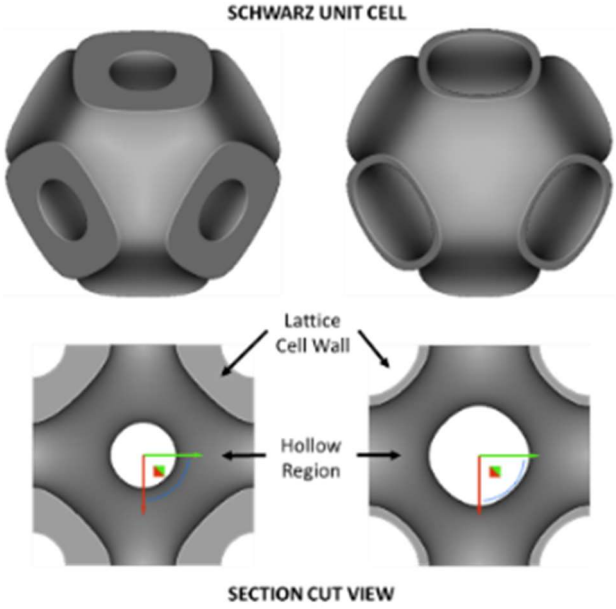

Figure 2-4. Schwarz unit cell section cut view illustrating change in cell wall thickness versus hollow region.

The complex nature of lattice geometry often requires additive manufacturing methods of stereolithography (SLA) or selective laser sintering (SLS)[1]. SLS and SLA processes utilize microscopic material, respectively powders or liquid resin, allowing for increased dimensional accuracy. Figure 2-5 displays lattice structures of varying design produced by SLS and SLA printers:

[1] For more information on 3D printing methods, see reference: *"3D Printing Technology Comparison: FFF vs. SLA vs. SLS"* [35]

Figure 2-5. Lattice structures produced by selective laser sintering (SLS) and stereolithography (SLA) [32].

FFF is not commercially used for manufacturing lattice structures due to FFFs limitations when printing cavities, beams that span over unsupported overhangs (see Figure 2-6) and the relatively low dimensional accuracy when compared to SLA and SLS processes [36]. For these reasons the following research was performed to identify FFF's capability of printing miniature lattice structures.

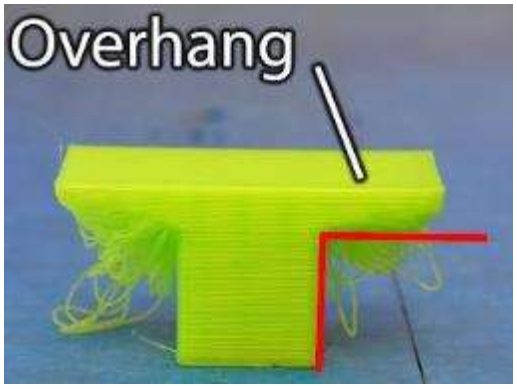

Figure 2-6. Demonstration of loss in fidelity resulting from unsupported overhangs [37].

Research was conducted on consumer grade FFF printers and successfully printed the microscopic beam lattices shown in Figure 2-7. Additionally, the research characterized the printed structures' performances through compression tests identifying that "the lattice structures showed partial elastic recovery (up to 80% of their original height) after the load was removed" [36]. The lattice materials tested were acrylonitrile butadiene styrene (ABS) and polylactic acid (PLA) which are stiff plastics and commonly used with FFF. The results of the stiff materials demonstrating elastic properties indicates that the design of lattice influences the entire structure's mechanical properties.

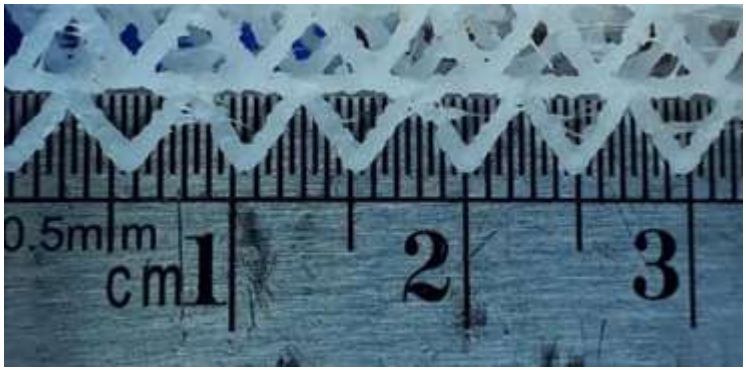

Figure 2-7. Miniature lattice structures produced by fused filament fabrication [36].

The demonstration of FFF printer capability to produce miniature lattice structures establishes that FFF printers remain candidate for production of a PKJ that utilizes lattice structures. For further discussion on TPMS cells produced by FFF and a performance comparison to beam structures (see Section 2.4.2).

2.4.2 3D Printed Schwarz Lattice Cells

Researchers have demonstrated that the Schwarz cell utilizes structural biomimicry of sea urchins (see Figure 2-8) creating a "dome-type structure economical in materials as compressive stress is transferred very effectively from the surface of the dome to the margin of the dome" [38]. In tie to additive manufacturing, research of 3D printed TPU Schwarz structures demonstrate "better stiffness and almost equal energy-absorbing capabilities compared" [38] to both EVA foam and alternative beamed lattice structures.

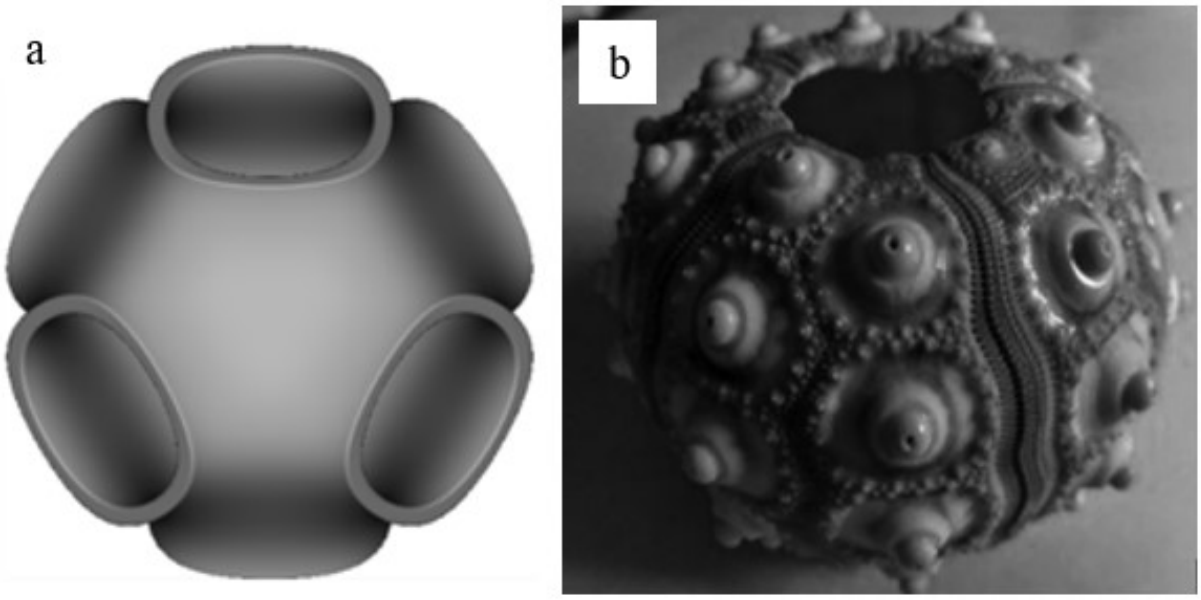

Figure 2-8. (a) Schwarz unit cell generated with nTopology software. (b) sea urchin shell related to dome structure of Schwarz cell [38].

The Schwarz cell geometrically complements design for additive manufacturing (DFAM). The structure consists of self-supporting arches of sloping continuous surfaces eliminating severe overhangs and the need for support structures: "fabrication time of the supportless lattice was 3h less when compared with specimens printed with support and 11-h reduction of postprocessing hours …. The cost for printing this was three times less compared with specimen printed with support" [38].

2.4.3 Elastic Filament

Thermoplastic polyurethane (TPU) is a highly elastic material that can be printed on desktop 3D printers via FFF. Published research classifies that TPU hexagonal cells (see Figure 2-9) can be utilized for energy absorption and still elastically recovery. This property is "comparable to that of traditional expanded closed cell polyurethane foams" found in shoes and can be incorporated into a single-axis knee [39]. For 3D printed lattice structures to be used within a single-axis knee, the structure must be able to deform as the knee bends and then return to its original shape. The lattice structure will provide cushioning to the user as load is applied and has potential to provide rate-control assisting the knee return to a straight position.

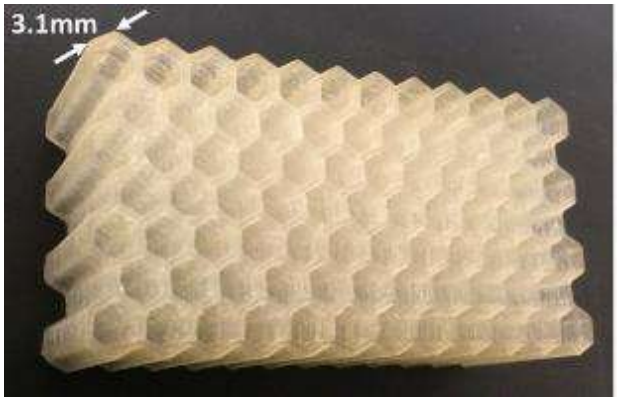

Figure 2-9. Fused filament fabricated lattice structure made from elastic materials [39].

Additional studies have also analyzed honeycomb lattices with 3 different density zones shown in Figure 2-10.

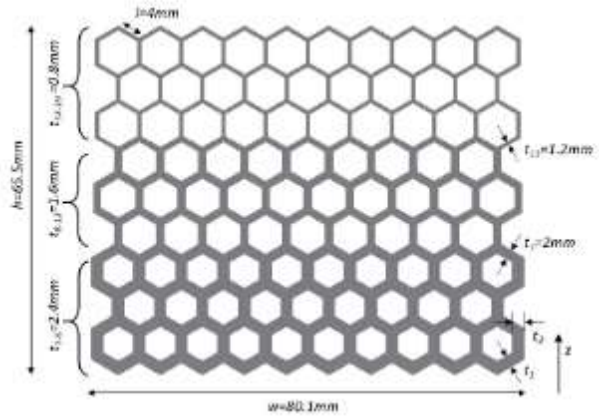

Figure 2-10. Lattice structure consisting of three different density zones [40].

Figure 2-11 displays how *(b)* deforms in steps per density zones whereas *(a)* deforms uniformly across the entire structure. As 3D printing allows for modification of dimensions and parameters of the cells, the design of lattice structure densities will be considered for varied stiffness during different phases of walking such as heel strike versus toe-off or for deformation during knee-bend.

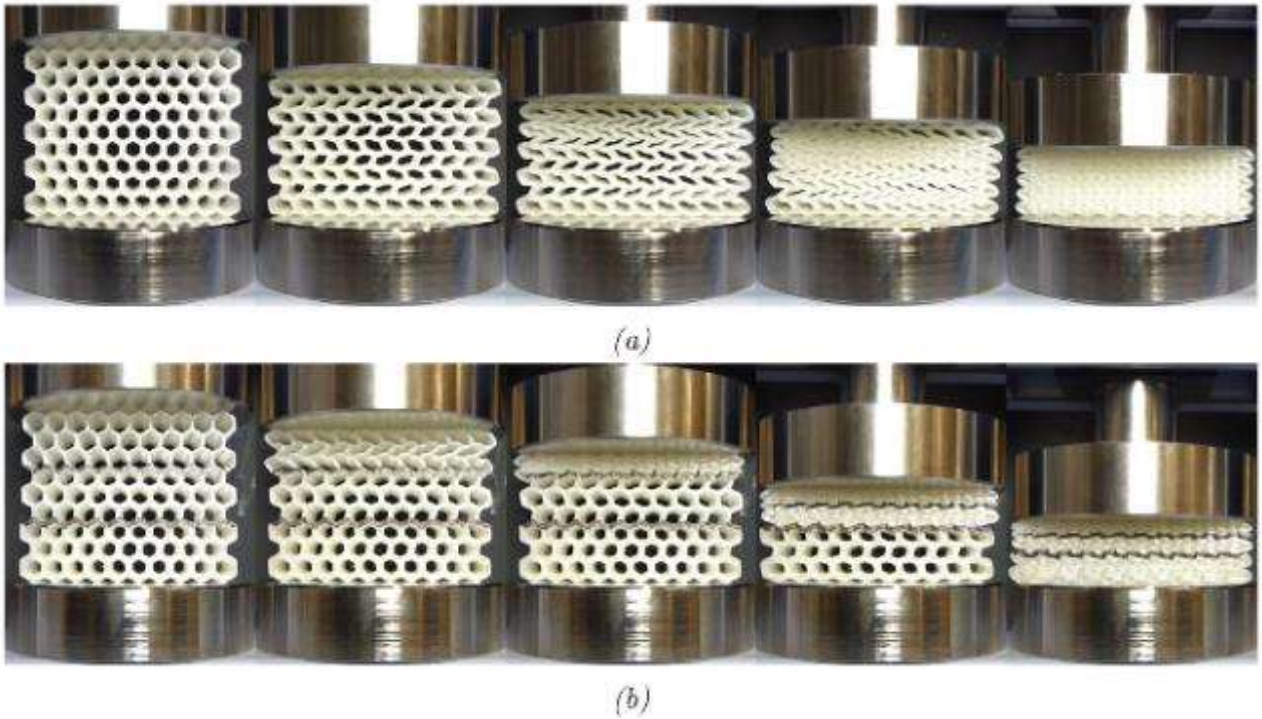

Figure 2-11. (a) displays consistent compression throughout structure due to uniform cell density. (b) displays zonal compression due to varied cell density [40].

2.4.4 Modified PLA Filament

Polylactic Acid (PLA) is a thermoplastic filament for FFF 3D printing and is widely used due to its stiffness, ease of printability, low-cost, and high static strength (see Figure 2-12). PLA filament is compatible with low-end, consumer desktop printers as the material does not require a heated build enclosure and does not produce toxic fumes making the material a preferred material for use by hobbyists and developing countries.

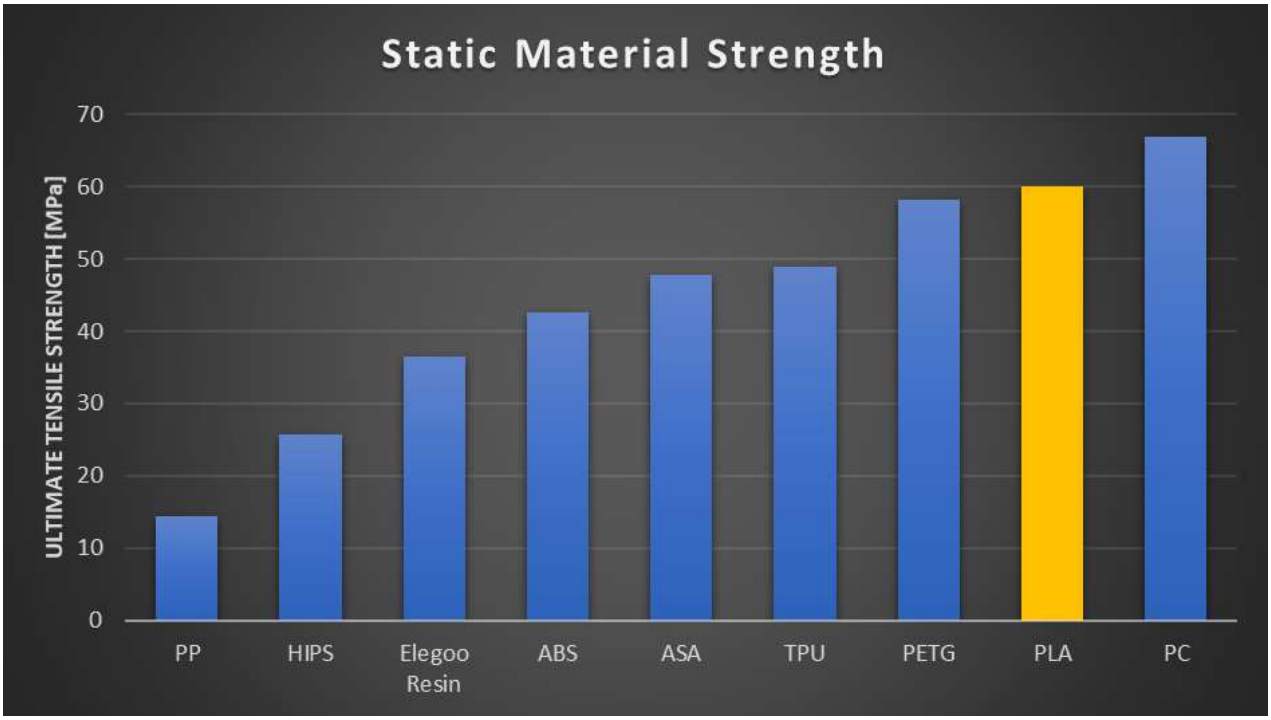

Figure 2-12. Static strength comparison of FFF filaments [41].

However, PLA is a brittle material that fails catastrophically without warning or yielding (see Figure 2-13). Filament manufacturers have recently introduced modified PLA filaments with claims of improved surface finish, increased toughness, UV resistance, increased shear strength, etc. all varying and dependent on the manufacturer's proprietary addition of additives [42,43]. Manufacturers often market the modified PLA under a unique trademarked name such as '"PLA+", "PLA Plus", or "PLA Pro"' [42].

Independent research has demonstrated that modified PLA named PolyMax (sold by brand PolyMaker) yields before failure compared to the company's standard PLA which snaps upon failure as shown in Figure 2-13 [41].

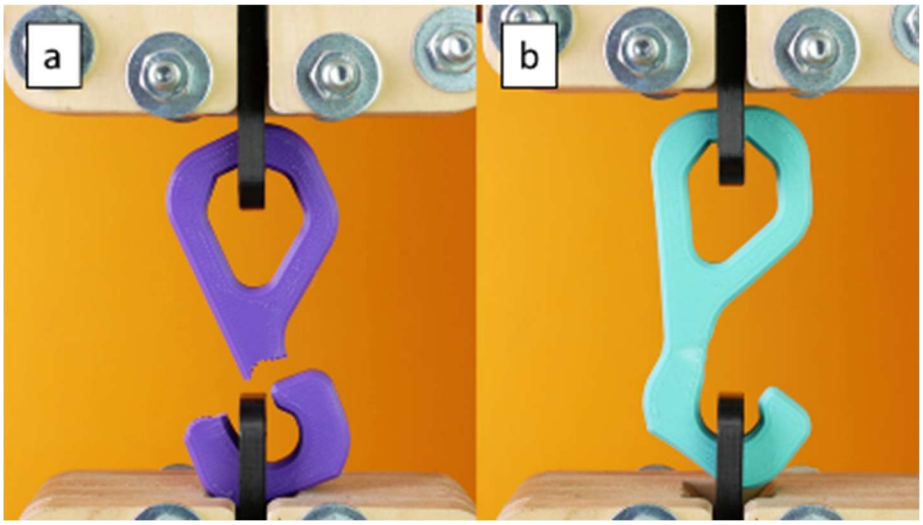

Figure 2-13. Tensile Test Specimens (a) Brittle failure of PolyMaker PolyLite PLA (b) Ductile failure of PolyMaker PolyMax PLA [41].

The research demonstrated that the yielding of modified PLA allows for increased toughness as it redistributes the loads and takes up more energy as shown in Figure 2-14 Load vs Displacement curves [41].

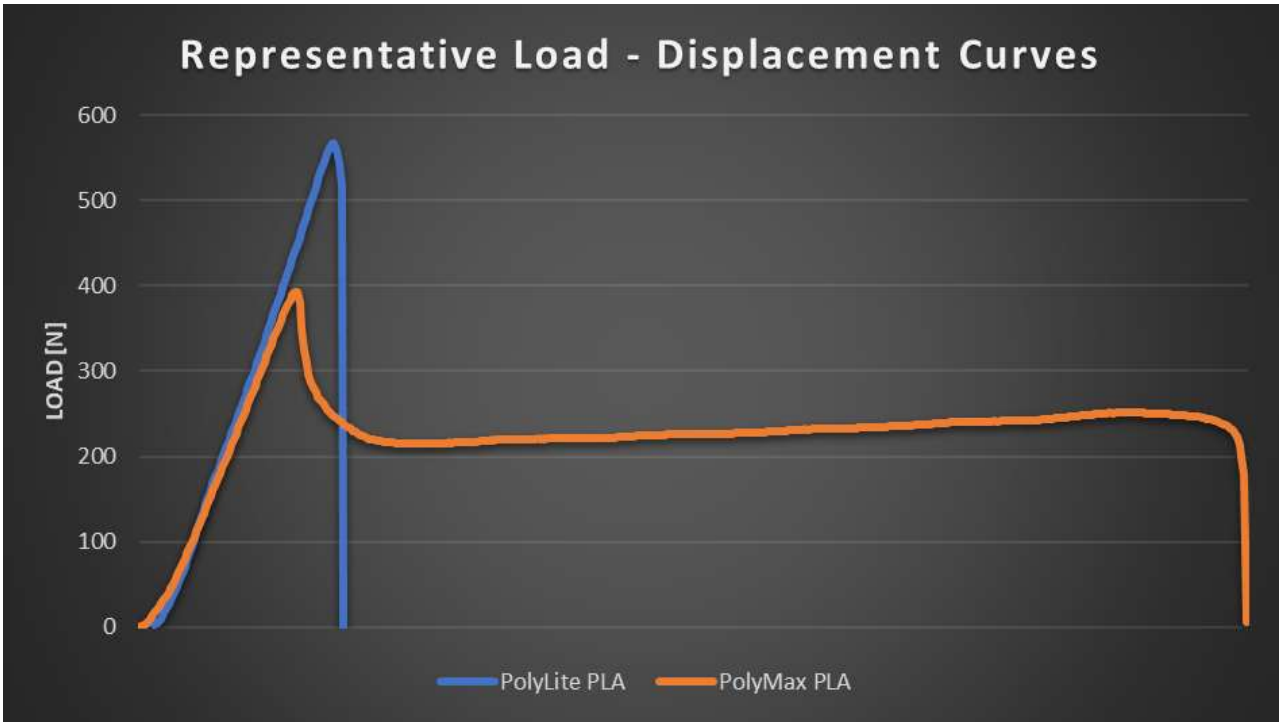

Figure 2-14. "Representative Load - Displacement curve of 3D printed coupons" [41].

Additional independent researchers developed their own modified PLA filament by adding specific additives to increase PLA impact strength. The modification resulted in 109% increase in Charpy impact strength with "improved damping performances, especially at high frequencies" [44].

With specific regards to the design of a PKJ, increased toughness is desired to eliminate potential catastrophic failures when the product undergoes severe loads or the product life-cycle is complete. However, the use of modified PLA should be cautious for it has been demonstrated that not all modified PLA filaments will perform with improved mechanical properties [42] and in many cases manufacturers do not quantify their advertised claims raising concern that companies are simply changing their product's name to become "PLA PLUS."

2.4.5 Low-Cost Knee Joint Solutions

One of the most prevalent advancements of affordable PKJs is the ReMotion knee (see Figure 2-15) designed by D-Rev, a non-profit company, for the JaipurFoot Organization priced at R1,170 and mimics R14,600+ polycentric knee designs (respectively, approximately $80 and $1,000+) [45]. Polycentric knees are mechanical assemblies with linkages and springs to replicate anatomical movement and dampening. Additionally, the JaipurKnee designed by Stanford was developed with strict budget constraints and can be acquired for R292 (approximately $20) [46]. However, according to Krista Donaldson of D-Rev, end users often need to modify the product to avoid clicking noises and to avoid edges catching on clothing [11]. Both knees when fitted to amputees in India "immediately improved gait quality and patient satisfaction" [45] demonstrating that performance does not correlate directly to the price of the prosthetic.

Figure 2-15. Design iterations of the ReMotion knee [47].

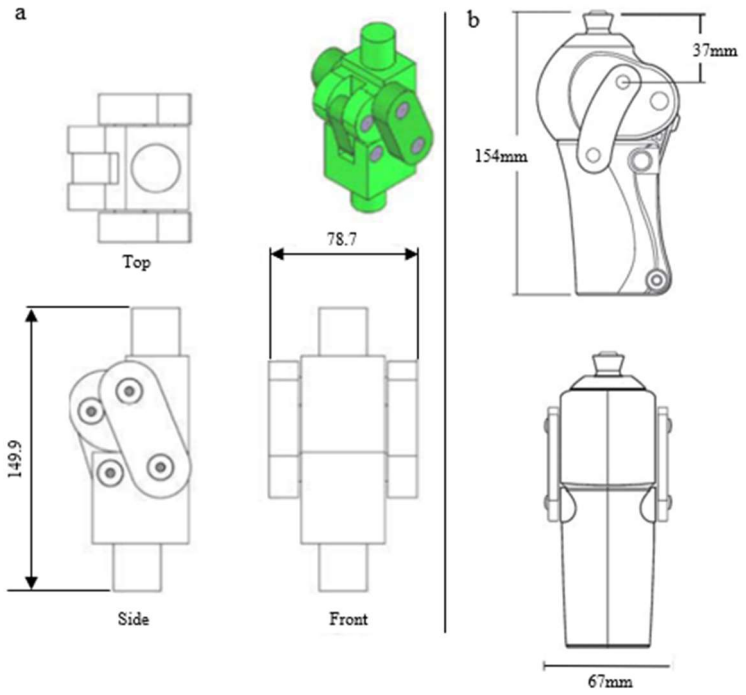

Figure 2-16. (a) Dimensions of the JaipurKnee [48]. (b) Dimensions of the ReMotion knee [49].

Both the ReMotion Knee and JauipurKnee are available in a single size that is designed as a one-size-fits-all design (see Figure 2-16). Both products are mass produced by method of injection molding and have made a positive global impact on amputees, however, the barriers of entry for injection molding (see Section 1.4) leaves developing countries dependent on external manufacturing from companies such as D-Rev.

2.4.6 3D Printed Knee Joint Solutions

In 2017, Tyagi Ramakrishnan, Mechanical Engineer at the University of South Florida, designed a 3D printed knee that utilized gears to hinge the knee joint (see Figure 2-17) [50]. Since the knee was designed for 3D printing, the knee can be scaled up or down dependent on the patient's anatomy.

Figure 2-17. 3d printed geared prosthetic knee joint [50].

The design does not consist of any form of pneumatics or hydraulics to dampen the loads due to walking, however, the design utilizes gears whose ratio can set the speed at which the lower-limb swings while walking. The study compared the 3D printed design to a tried and tested commercial prosthetic (Ossur Total Knee 2000) and identified that the 3D printed knee was bulkier due to fabrication with carbon fiber, yet the design allows for customization of size and gearing of the prosthetic to each individual user. Internal springs are located within the prosthetic whose gage and position can be optimized to further improve gait.

This knee demonstrates that there is potential through 3D printing to reimagine the mechanism of a PKJ, however, research in this field is limited and requires additional input.

2.4.7 Prosthetic Knee Joint Standard Components

A wide range of industry standard adapters are commercially available to adapt a prosthetic knee joint to the user's prosthetic socket and foot.

Figure 2-18. Components of a prosthetic leg [51].

The PKJ pylon shown in Figure 2-18 is secured by a 30mm tube clamp (see Figure 2-19) which can be adapted to or integrated into the knee joint.

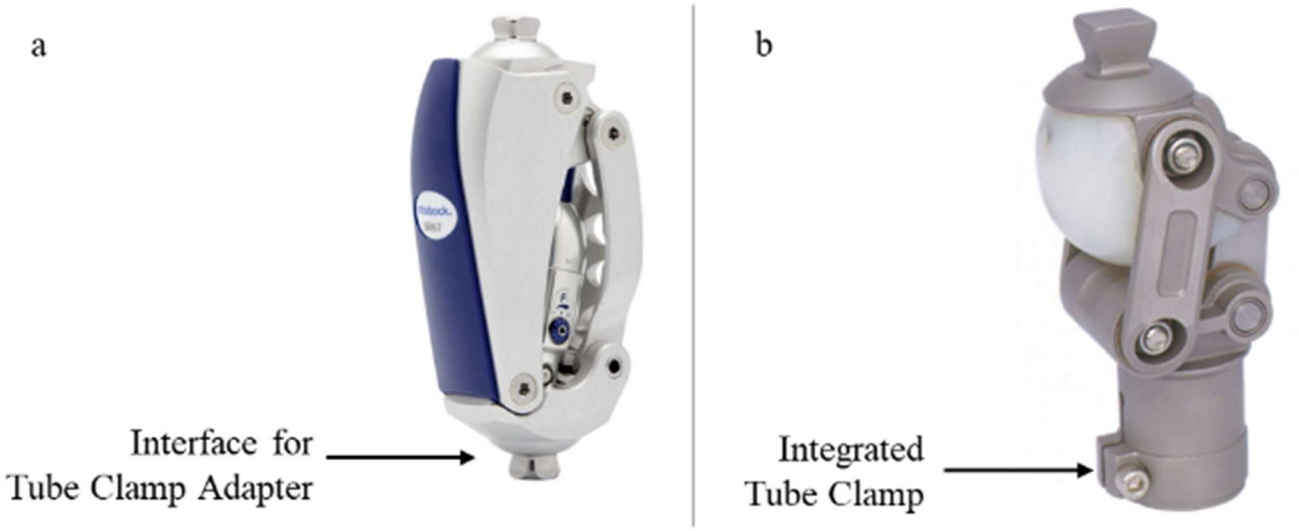

Figure 2-19. (a) Prosthetic knee joint with pyramid interface requiring tube clamp adapter[52]. (b) Prosthetic knee joint with integrated tube clamp[53].

The prosthetic knee joint can be connected to the user's socket by a titanium pyramid adapter. Pyramid adapters can either be connected to the PKJ by a standard 4-hole pattern (see Figure 2-20 or can be integrated directly into the PKJ as shown in previous Figure 10-19. A 4-hole pattern allows for modularity in design.

Figure 2-20 (a) Standard 4-Hole titanium pyramid adapter [54]. (b) 4-hole rotating pyramid adapter [55]. (c) 4-hole offset pyramid adapter [55].

2.4.8 3D Printing for Strength

3D printed parts exhibit anisotropic properties related to the orientation during fabrication. Research has demonstrated that parts display maximum strength when layers are oriented parallel to the load as shown in Figure 2-21.

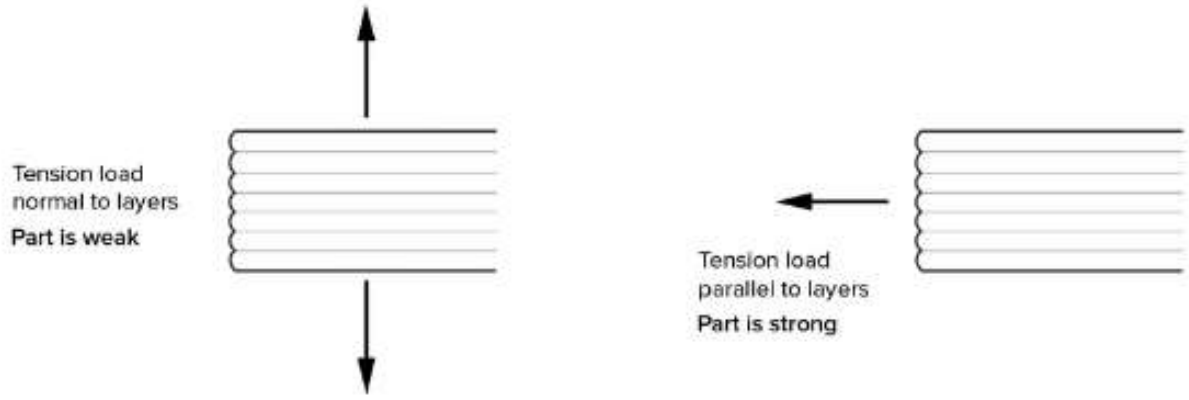

Figure 2-21. Identification of 3D printed layer strength in relation to tension load [56].

Flatwise (YXZ) and edgewise (YZX) orientations, defined in Figure 2-22, result in layers being placed in tension when loaded and display increased strength compared to upright (ZYX) orientation.

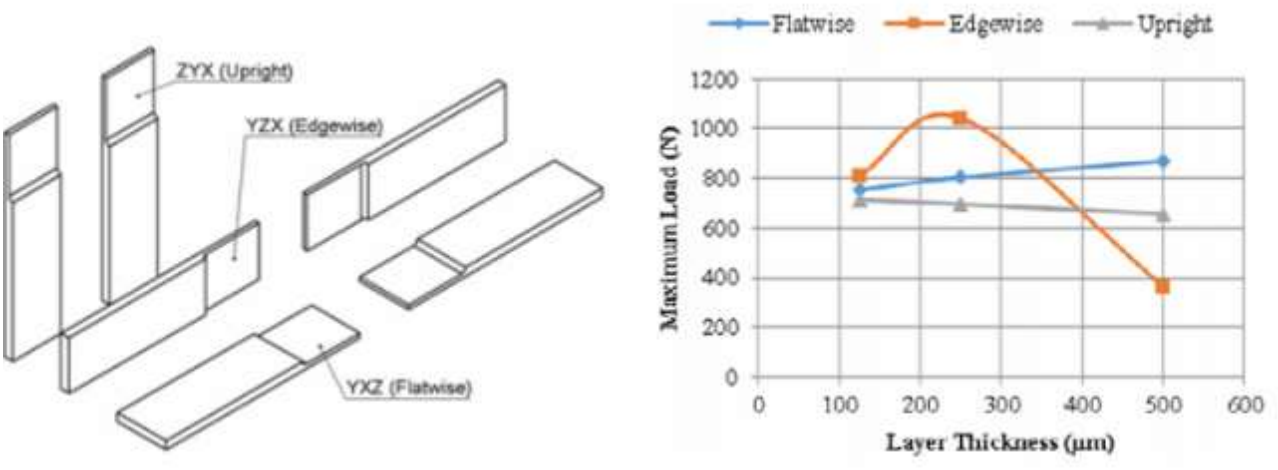

Figure 2-22. Definition and comparison of part load capabilities vs orientation [56].

Part strength additionally varies based on layer height and nozzle size which equates to a larger line extrusion width (see Figure 2-23).

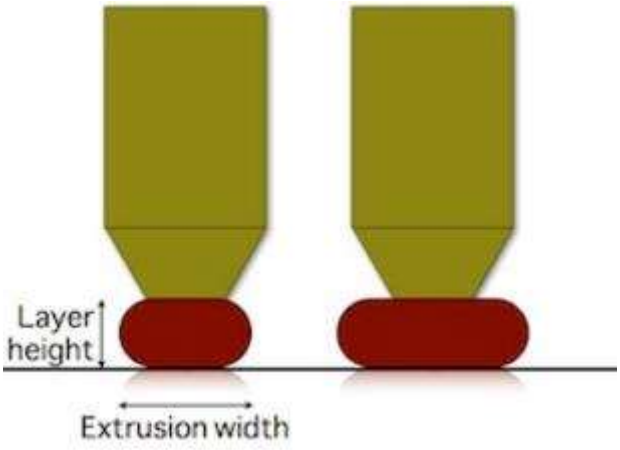

Figure 2-23. Definition of layer height and extrusion width [57].

Researcher Vladimir E Kuznetsov has demonstrated that part strength increases as layer height decreases and nozzle size increases (see Figure 2-24) [58]. Kuznetsov states that as layer size increases, the "threads" of extruded filament retain a circular cross-section resulting in less surface area for cohesion between layers [59].

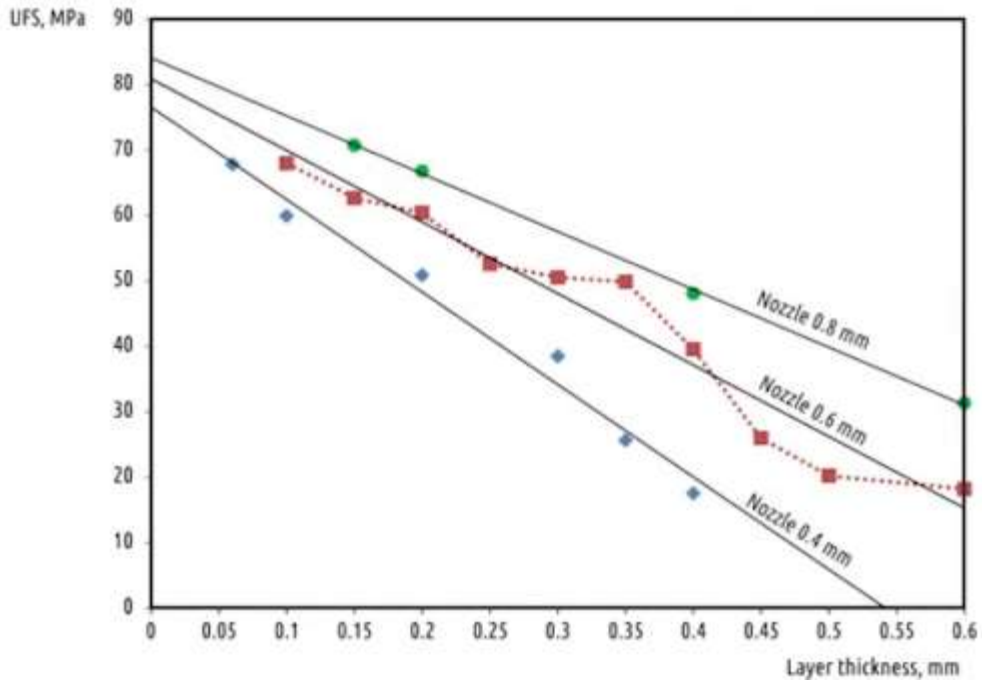

Figure 2-24. Flexural strength (UFS) of test samples versus layer height and nozzle size [59].

Figure 2-25 provides microscopic images taken by Kuznetsov displaying that a decrease nozzle size extrudes creates a rectangular cross-section and decreases air gaps between lines of filament creating strong cohesion between layers.

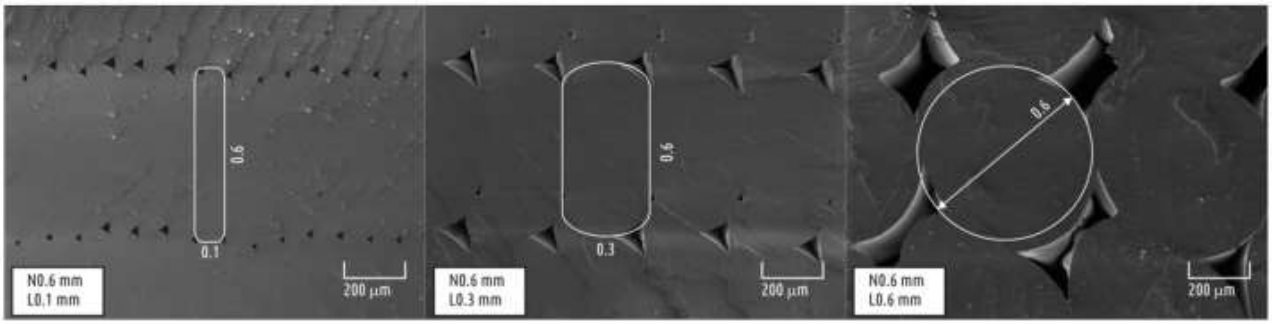

Figure 2-25. Photo and caption from Vladimir E Kuznetsov*: "Transformation of an individual thread cross-section with layer thickness increase" [59].*

2.4.9 Human Knee Biomechanics

The human knee can bend forward (extension) or backwards (flexion). A gait cycle occurs during walking requiring the human knee to transition from extension to flexion relatively labelled as the heel-strike and push-off in Figure 2-26.

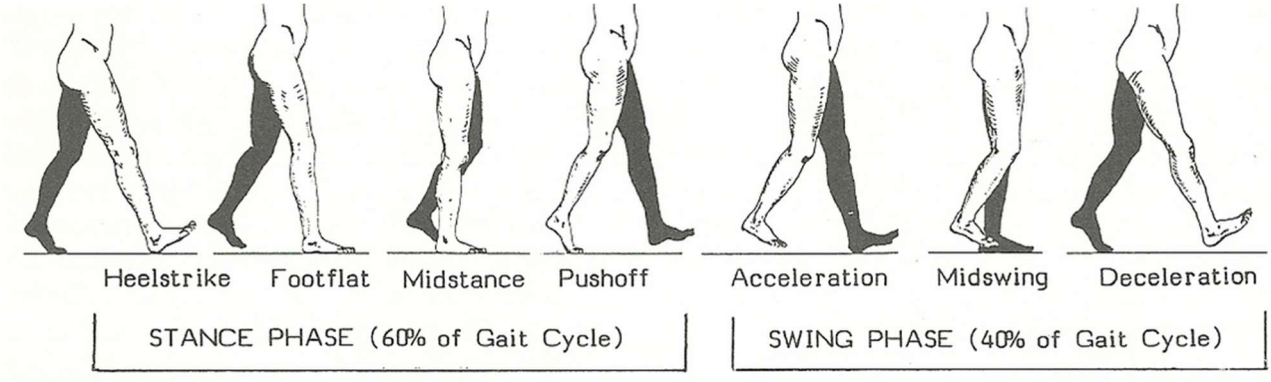

Figure 2-26. Phases of the human gait cycle [60].

A range of motion (ROM) from 10-degree extension to 120-degree flexion is identified as acceptable for most normal functional activities shown in Figure 2-27 below:

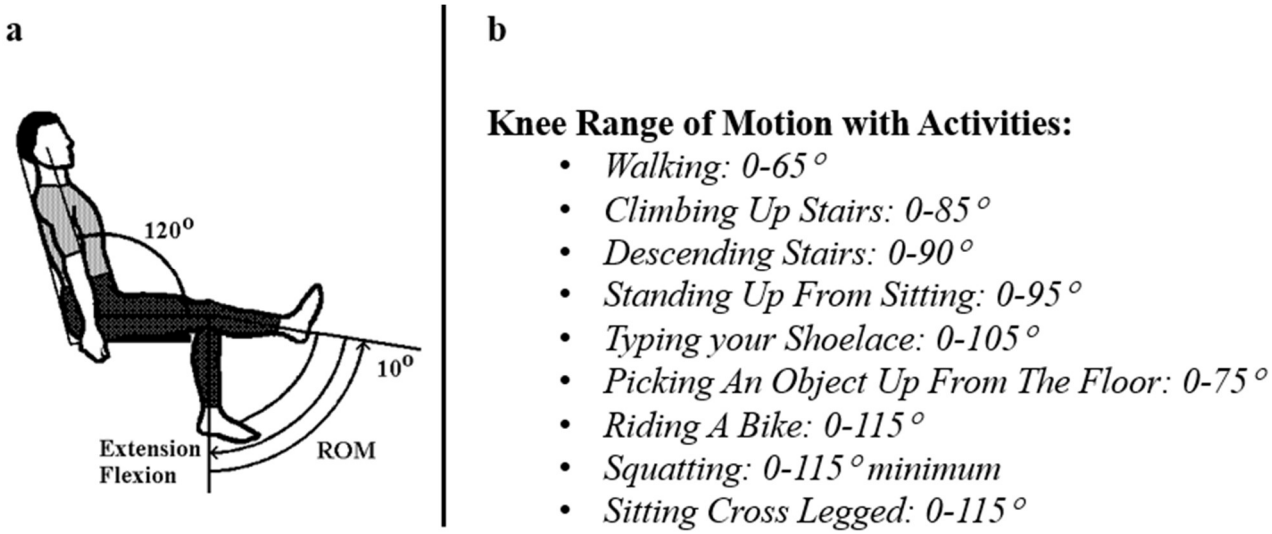

Figure 2-27. (a) ROM of Human Knee [61]. (b) Knee ROM activity list [62].

2.4.10 Static Load Requirements

The following nomenclature of Loading Condition I, Loading Condition II, and Loading Condition III will be referenced throughout the rest of the report and are summarized in Table 2-1. Summary of Static Load Conditions.

Load condition I and load condition II represent ultimate static strength tests defined by ISO 10328:2016 as ultimate loads imparted during late and early phases of the human gait cycle. Load condition III represents a 100 kg body standing at rest on one leg resulting in 980 N applied to the PKJ.

Table 2-1. Summary of Static Load Conditions

Test	Description	Force	Force Location	Constraints
Loading Condition I	ISO 10328:2016 Ultimate Static Strength Test	3360 N	Remote Load	Remote Fixed Constraint
Loading Condition II	ISO 10328:2016 Ultimate Static Strength Test	3019 N	Remote Load	Remote Fixed Constraint
Loading Condition III	Representative of user standing on one leg	980 N	Direct Normal Load	Direct Fixed Constraint

ISO 10328:2016

The International Organization for Standardization defines ISO 10328:2016, titled *'Prosthetics — Structural testing of lower-limb prostheses — Requirements and test method'* as " a result of concern…about the need to provide prostheses that are safe in use" [63].

ISO 10328:2016 defines loading conditions for lower limb prosthetic devices relating to ultimate load scenarios along with normal wear and tear from daily use. The scope of this research project will test only perform ultimate strength tests on the designed PKJ assembly as defined by ISO 10328:2016: "Section 16.2.2.2 Performance Requirements" (see Figure 2-28).

Table 2 — Categories of strength addressed in this International Standard, together with the related performance requirements and test methods for their verification

Category of strength	Related performance requirement [a]	Test method for verification
Ultimate strength (see 3.2)	Structure shall sustain static loading by ultimate test forces at prescribed values	Principal static ultimate strength test (16.2.2), separately applied in two test configurations, separate static ultimate strength test for ankle-foot devices and foot units (17.2.4), separately applied in heel and forefoot loading, separate static ultimate strength test in maximum knee flexion for knee joints and associated parts (17.3), separate static ultimate strength test for knee locks (17.4.4), applied in a single test configuration

Figure 2-28. ISO 10328:2016 Ultimate strength performance and testing requirement [63].

The ultimate strength test is defined as "static load representing a gross single event, which can be sustained by a the prosthetic device/structure but which could render it thereafter unusable" and states performance requirement that the "structure shall sustain static loading by ultimate test forces at prescribed values" [63].

Test Definition

The ultimate static test force (F_{SU}) is calculated by ISO 10328 for P5 test conditions defined by "data from all amputees including a few whose body mass exceeded 100 kg" [63].

ISO 10328:2016 requires two separate loading conditions are required for completion of the ultimate strength test:

(I) Test loading condition I is related to the instant of maximum loading occurring early in the stance phase of walking.

(II) Test loading condition II is related to the instant of maximum loading occurring late in the stance phase of walking [63].

To represent the phases of walking, remote offsets are used to define locations of loads and boundaries. Figure 2-29 below defines the coordinate reference system used to define remote offsets:

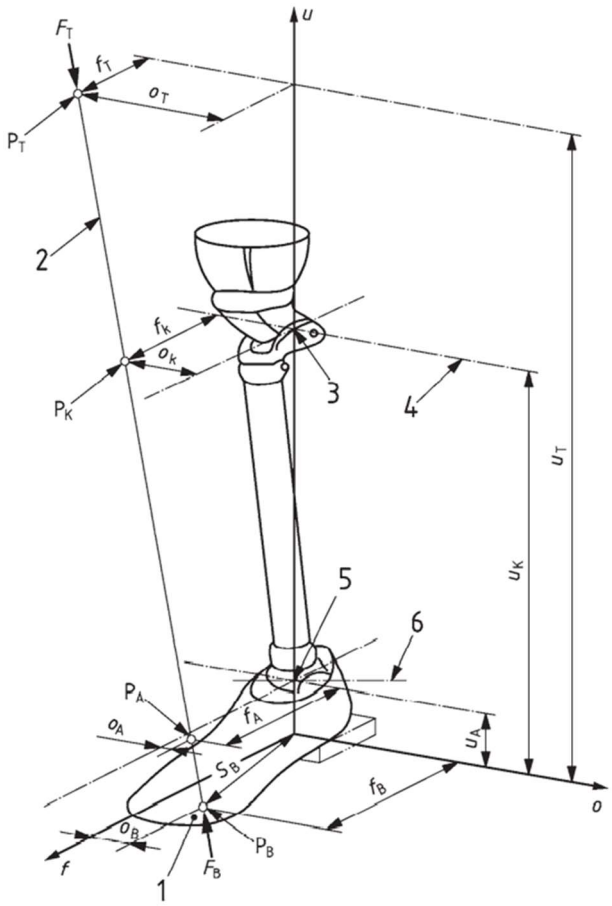

Key

1	left foot
2	load line
3	effective knee-joint centre
4	effective knee-joint centreline
5	effective ankle-joint centre
6	effective ankle-joint centreline
P_K	knee load reference point
P_A	ankle load reference point
P_B	bottom load application point
P_T	top load application point

Figure 2-29. Remote offset alignment and coordinate system example for left prosthetic [63].

Table 2-2 lists the required offsets to be used for load condition I and load condition II with respect to the reference coordinate system defined in Figure 2-29.

Table 2-2. Values of Test Forces and Offsets for Ultimate Strength Test

	Units	Load Condition I	Load Condition II
$F_{SU,\ upper\ level}$	N	4480	4025
$F_{SU,\ lower\ level}$	N	3360	3019
O_T	mm	-79	-40
F_T	mm	82	55
U_T	mm	650	650
O_K	mm	-50	-35
F_K	mm	52	72
U_K	mm	500	500
O_A	mm	30	-22
F_A	mm	-32	120
U_A	mm	80	80
O_B	mm	45	-19
F_B	mm	-48	129

Performance Requirement

To pass the static ultimate strength requirements the test sample must be loaded to $F_{SU,\ lower\ level}$ at a rate between 100 N/s and 250 N/s without loss of structural integrity. Compliance conditions are met if two test samples for each load conditions I and II meet the previously stated requirements. For more details refer to ISO 10328:2016 “Section 16.2.2.2 Performance Requirements” and “Section 16.2.2.3 Compliance conditions” [63].

3. RESEARCH METHODS

Research was performed with quantitative analysis and experimental investigation. The 3D printed PKJ assembly was designed specifically for FFF 3D printing using CAD software and contains deformable lattice structures. Static load tests were performed through CAD simulation to characterize the lattice structure and the PKJ assembly's structural performance guided by ISO 10328:2016. Experimental lab tests were performed on 3D printed prototypes to validate simulation data. The following sections detail this research project's methodology:

3.1 Materials

All components of the designed PKJ were sourced within South Africa to align with the research projects aim of producing a low-cost PKJ for developing countries. Modified PLA filament was selected for designed PKJ components requiring rigidity and TPU filament was selected for the compressible lattice structure

Due to the anisotropic nature of additive manufacturing, 3D printing filaments were subjected to tensile testing guided by ISO 527-2-1BA to identify material properties required for simulation. All test specimens were printed with settings and orientations identical to the designed PKJ's 3D printed parts to ensure accurate simulation inputs.

3.2 Modelling

Fusion 360

The PKJ assembly was first modeled in Autodesk Fusion 360 software for both visualization and dimensioning of the design. The bounding geometry of the successful Jaipur Knee was used as a starting size for the PKJ design (see Figure 2-16) and were modified until simulation results met ultimate static load requirements set by ISO 10328:2016 for a body mass exceeding 100 kg. The PKJ design was modeled with smooth, curved surfaces creating anatomical resemblance and functionality to enable the device to slide freely through clothing.

The PKJ is designed to interface with standard commercial prosthetic components such as the 30mm pylon and 4-hole adapters allowing for integration with commercial components readily available for amputees (see Section 2.4.7). Required procured components of various nuts and bolts were added to the CAD model assembly to create mounting features.

Fusion 360 software was additionally utilized for motion simulation to ensure that the PKJ could rotate freely around the defined single axis without component interferences. Parts designed in Fusion 360 requiring lattice structures were next imported into nTopology software.

nTopology

nToplogy software was utilized to quickly generate lattice structures on desired regions of the CAD part designed in Fusion 360. Various beam and TPMS lattice structures were modeled into the CAD part and visually examined to identify feasible structures that conformed to the geometry of the CAD part. Congruently, examination was performed to ensure any conforming lattice structure also contained a geometry that could be produced by FFF.

After identifying and modeling a feasible lattice structure, the modeled part was subjected to simulation within nTopology to characterize the stiffness and strength of the structure. Simulation loads were with respect to ultimate load conditions and normal load conditions defined in Table 2-1. Simulation results were used to optimize the lattice parameters. Lattice modeling and simulation were performed in an iterative loop with ongoing adjustments of parameters until desired mechanical properties were achieved.

3.3 Simulation

Static load simulations were performed via ANSYS Mechanical software to identify structural strength of the PKJ assembly and how interactions between bolted connections and components of various materials will distribute applied stress.

This research project simulated P5 test conditions (body mass of 100 kg) as P5 represents the heaviest amputee demographic defined by ISO 10328:2016. Simulation of P5 test conditions for load conditions I, II, and III are defined in Table 2-1. Load condition I and load condition II represent ultimate static strength tests defined by ISO 10328:2016 as ultimate loads imparted during late and early phases of the human gait cycle. Load condition III represents a 100 kg body standing at rest on one leg resulting in 980 N applied to the PKJ.

Remote boundary conditions were utilized for load condition I and load condition II defined by ISO 10328:2016.

The following simulation software was utilized:

- nTopology was used to generate lattice structures and perform static load simulations on the modeled structure to characterize mechanical properties.
- ANSYS Mechanical was used perform static load simulations on the PKJ assembly, identifying stress distribution and interactions between components.

Prosthetic knee joint simulation involved the design successfully meeting the prescribed load conditions for static load tests. Simulation plots for total deformation, von-Mises stress, and factor of safety (FOS) were analyzed. Design alterations occurred based from simulation data until the PKJ assembly could withstand all load conditions.

3.4 Testing

Experimental lab testing was performed to validate and verify results for lattice simulation and PKJ assembly simulation (see Section 3.2 and Section 3.3 respectively).

A Shimadzu AG-IC universal test machine (UTM) was used to perform material tensile testing and apply static load testing, defined in Table 2-1, on 3D printed prototypes.

For load condition I and load condition II defined in Table 2-1, a test fixture was utilized to apply remote boundary conditions defined by ISO 10328:2016. A compressive plate was used for load condition III to directly apply the normal force to the PKJ.

Two prototype samples were provided for each experimental test as required by ISO 10328:2016 to satisfy compliance conditions.

3.5 Analysis

Data was collected to analyze the mechanical properties of the designed PKJ:

- Simulation data was collected in the form of total deformation, von-Mises, and FOS plots.
- Experimental test results were collected in tabular form for force and displacement and converted to stress and strain data respectively. Stress-Strain plots were generated for data visualization.

- A computer data acquisition system was used to operate the UTM and logged force and displacement for each test.

Cost and manufacturability analysis was performed on the designed PKJ to determine the feasibility of producing it or if an alternative process should be adopted

4. RESEARCH

4.1 Materials

4.1.1 Selection

All materials selected for the designed PKJ were sourced within South Africa to align with the research goal of aiding the prosthetic community in developing countries.

eSun eFlex TPU 3D printing filament (1.75mm diameter) was selected for the flexible lattice structures. 3D printed TPU lattice structures are elastic in behavior, demonstrating ability to cyclically absorb and return energy [64] (see Section 2.4.3).

eSun PLA+ was selected to produce parts requiring rigidity. eSun PLA+ is a modified PLA material and advertised by manufacturer eSun as having toughness two times more than PLA [43].

As mentioned in Section 2.4.4, modified PLA with increased toughness is expected to fail gradually by yielding rather than catastrophically. eSun PLA+ is selected with intention of preventing unexpected failure of the PKJ and which potentially could injure the prosthetic user.

4.1.2 Mechanical Properties

Experimental tensile testing of both eSun eFlex and eSun PLA+ filaments was guided by ISO 527-2-1BA "*Plastics – Determination of Tensile Properties*" [65]. However, the 3D printed test specimen dimensions defined by ISO 527-2-1BA required uniform scaling of 200% (see Figure 4-1). Scaling was necessary to align the predicted failure range of the test specimens with the working range of the available 20 kN load cell (1 kN to 19 kN).

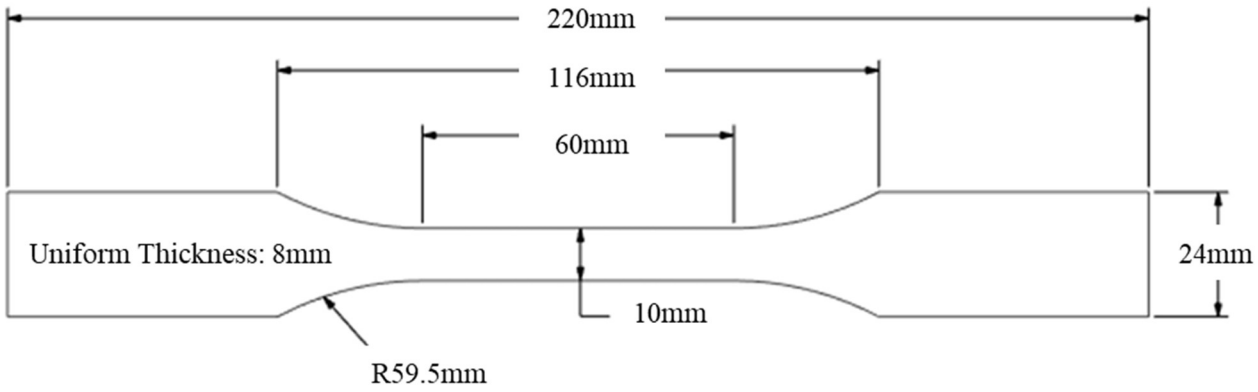

Figure 4-1. ISO 527-2-1BA Tensile Test Specimen Dimensions Scaled 200%.

Tensile test specimens were produced by a Creality Ender 3 Pro FFF 3D printer modified with a MicroSwiss Direct Drive extruder. Printer settings are listed in Table 4-1 below:

Table 4-1. 3D Printing Slicer Settings

Material	**eSun PLA+**	**eSun eFlex**
Nozzle Diameter, mm	.6	.6
Layer Height, mm	.2	.2
Wall Line Count	4	4
Printing Speed, mm/s	55	25
Print Infill, %	100	100
Nozzle Temperature, °C	220	230
Bed Temperature, °C	75	40
Brim	Outside	Outside
Support Placement	Touching Build Plate	Touching Build Plate
Support Overhang Angle, °	45	80

Three test specimens for each material were loaded to failure using an UTM with adjustable grip clamps shown in Figure 4-2 below:

Figure 4-2. Testing of eSun eFlex TPU tensile test specimen with a UTM.

Results

Table 4-2 lists the material properties obtained from the stress-strain plots which represent the specific properties of the respective 3D printing materials fabricated with settings defined in Table 4-1. The following material properties were utilized during CAD simulation of the lattice and PKJ assembly (see Section 4.3).

Table 4-2. Tensile Test Results: Material Properties of eSun Filaments

Material	Elongation at Break (%)	Yield Strength (Mpa)	Ultimate Tensile Strength (Mpa)	Density (g/cm^3)	Young Modulus (MPa)
eSun Pla+	8%	40	62	1.24	1529
eSun eFlex (Shore Hardness 95A)	771%	5	31	1.12	84

The resulting stress-strain plot for eSun PLA+ and eSun eFlex is shown in Figure 4-3 and Figure 4-4 respectively.

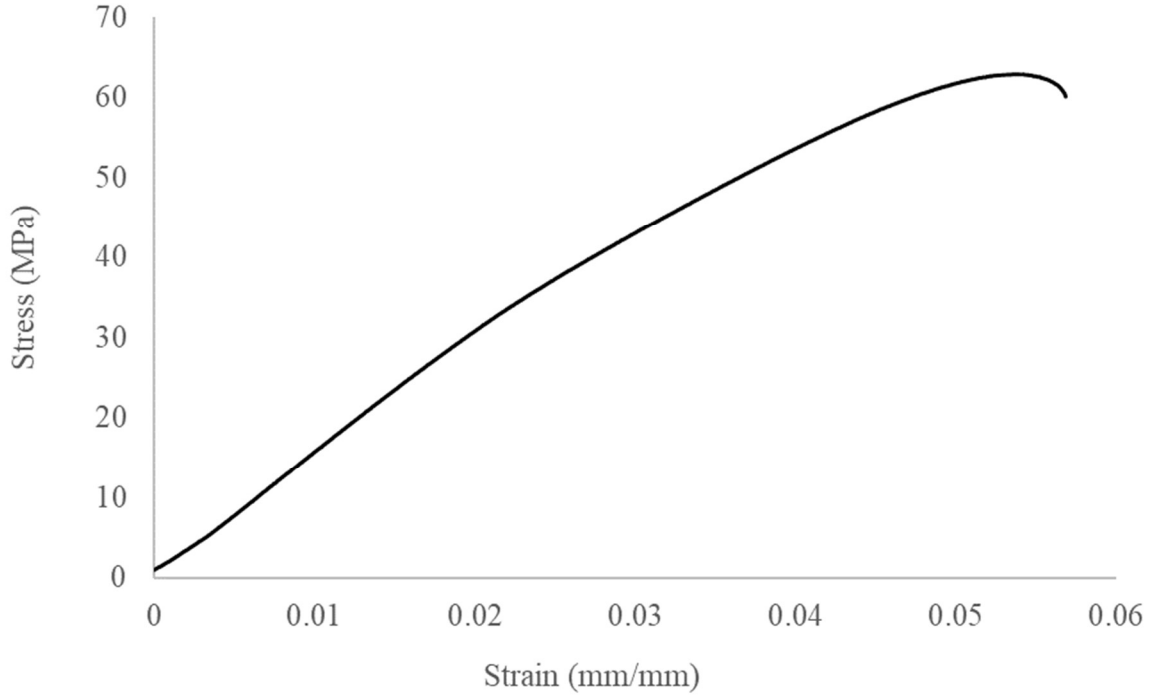

Figure 4-3. Stress vs Strain plot for eSun PLA+ tensile test specimen.

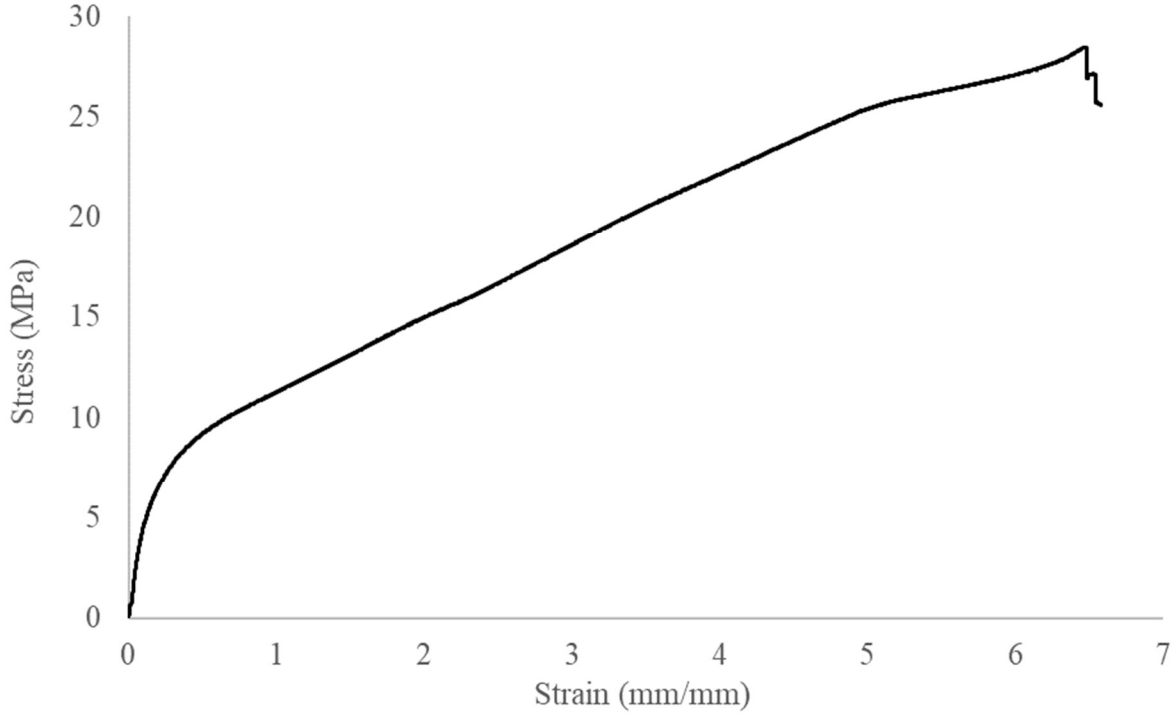

Figure 4-4. Stress vs Strain plot for eSun eFlex tensile test specimen.

Both plots demonstrate ductile materials with yielding before failure, however, eSun PLA+ was observed as a sudden, unexpected failure during testing and minimal necking with calculated 108%

elongation at break. eSun technical data sheet lists eSun PLA+ failing at 29% elongation (see Figure 4-5 however, tensile test data from Table 4-2 aligns with eSun PLA material which yields at 8%.

eSUN 3D PRINTING FILAMENT (Filament specification: 1.75mm / 2.85mm)

FILAMENT	Print Temp(℃)	Bed Temp(℃)	Density (g/cm³)	Distortion Temp (℃,0.45MPa)	Melt Flow Index (g/10min)	Tensile Strength (MPa)	Elongation at Break (%)	Bending Strength (MPa)	Flexural Modulus (MPa)	IZOD Impact Strength (kJ/m²)
PLA	190-210	No Heat/(60-80)	1.24	56	5(190℃/2.16kg)	65	8	97	3600	4
PLA+	205-225	No Heat/(60-80)	1.24	52	2(190℃/2.16kg)	60	29	87	3642	7

Figure 4-5. eSun Technical Data Sheet. Comparison of eSun PLA versus PLA+ mechanical properties [43].

Figure 4-6 displays the failure mechanic of the eSun PLA+ test sample. As noted previously in Section 2.4.4, not all modified PLA filaments perform as expected and it is best practice to self-characterize 3D printing filaments. eSun PLA+ remained selected for design of the PKJ as its ultimate tensile strength of 62 MPa is comparable to non-modified PLA (see Figure 2-12) and no other modified PLA filaments were available for purchase in South Africa.

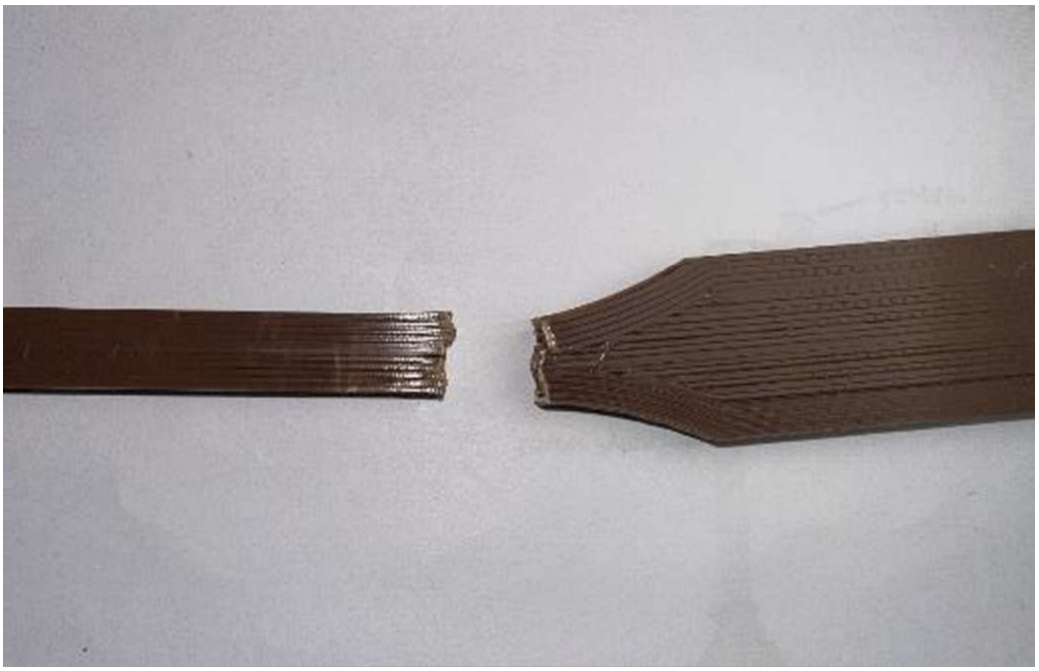

Figure 4-6. Failure mechanic of eSun PLA+ tensile specimen.

4.2 Design of Prosthetic Knee Joint

4.2.1 Prosthetic Knee Joint Assembly

The designed PKJ assembly is a passive single-axis knee designed for low-cost FFF 3D printing shown in Figure 4-7. The PKJ assembly is comprised of a smooth, curved body that tapers from a bulbed geometry creating resemblance to the shape of a human knee. Components such as fasteners are embedded to avoid protrusions allowing for ease when putting on pants and concealment of the PKJ when under clothes.

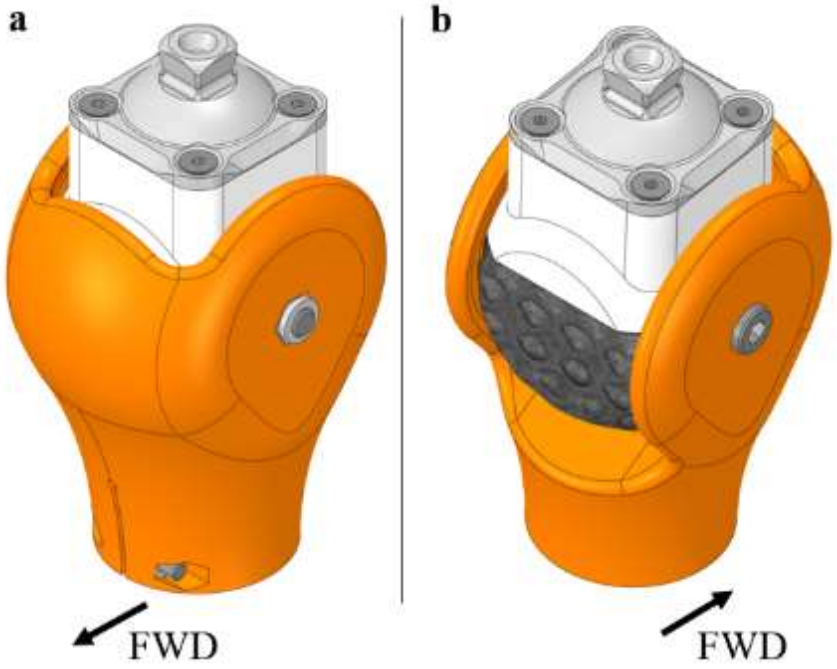

*Figure 4-7. PKJ assembly **(a)** front-isometric view. **(b)** back-isometric view.*

The designed PKJ assembly has a bounding box of 72mm x 90mm x 131mm and weighs 600 g (not including the pyramid adapter and four M5x30 screws identified in Figure 4-10). For a detailed weight breakdown of all components see Section 4.6.

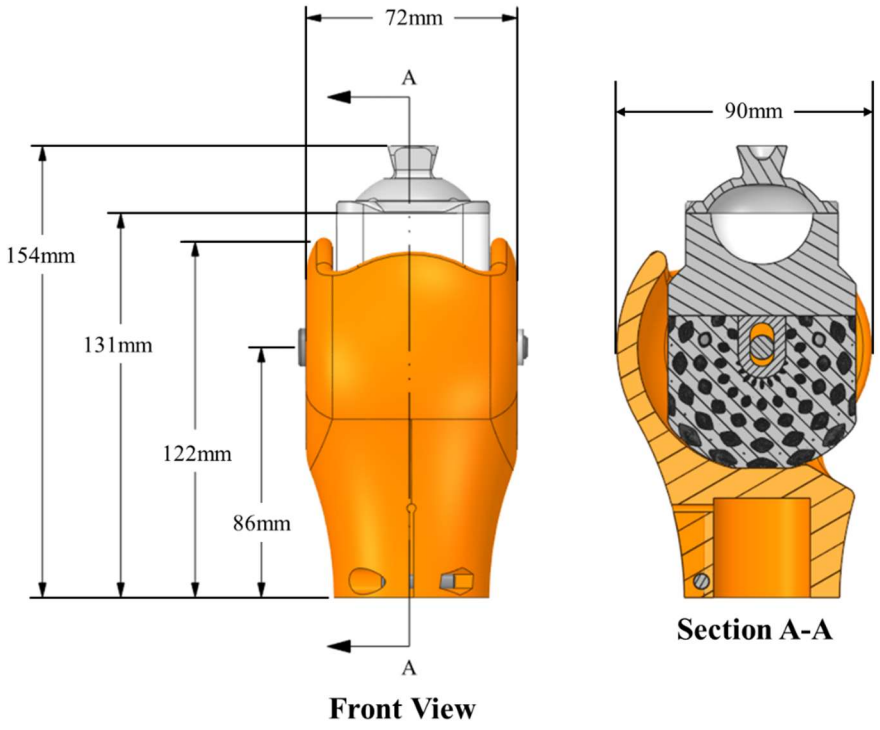

Figure 4-8. Bounding dimensions of PKJ Assembly excluding standard pyramid adapter.

The PKJ assembly contains 3D printed parts named the shell, and the lattice assembly which is comprised of the following subcomponents: the lattice region and the pyramid interface (see Figure 4-9). The shell and pyramid interface components are manufactured with eSun PLA+ filament allowing for a rigid structure and rigid interfaces for fasteners. The lattice region is manufactured from eSun eFlex TPU filament allowing for a deformable body. See Section 4.1 for detailed discussion of material selection and additive manufacturing methods.

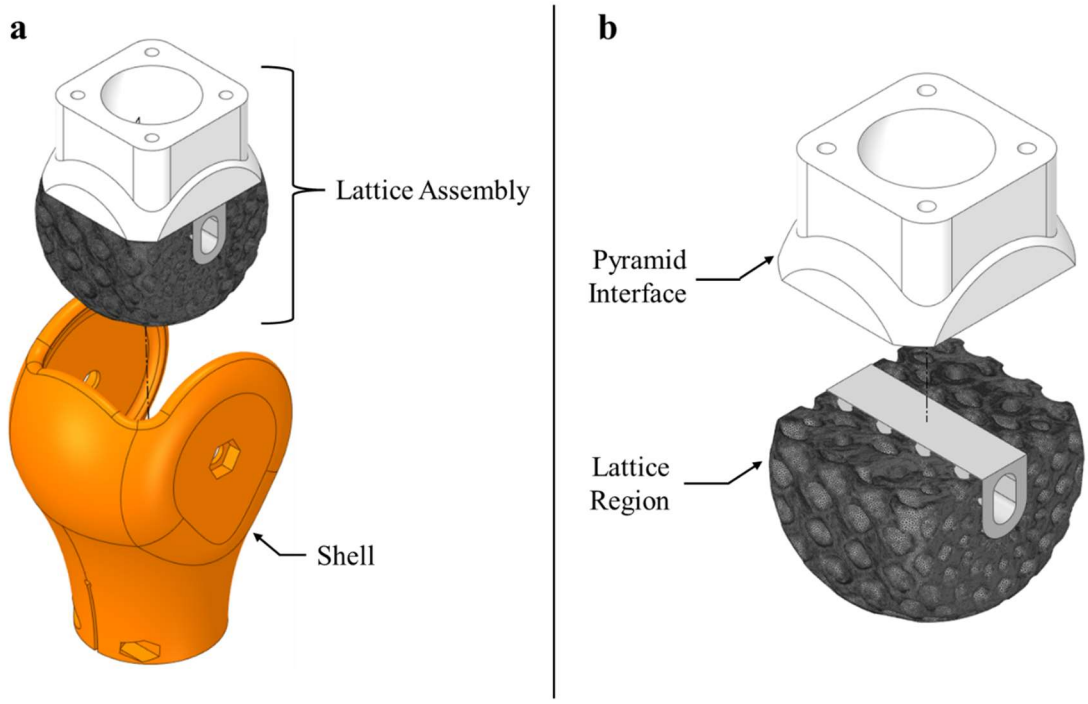

Figure 4-9. ***(a)*** *Exploded view of 3D printed components* ***(b)*** *Exploded view of lattice assembly.*

The lattice assembly is designed with elastically deformable lattice cells of varying sizes to provide cushion to the user. The resulting lattice structure can compress under the user's weight while being able to return to its original shape when load is removed. The individual lattice cells in combination to flexible 3D printed material enables the lattice region to deform regionally throughout the part and provide stability as the user's stance shifts. Section 4.2.2 will discuss the lattice region component in detail.

Figure 4-10 identifies the necessary procured fasteners for the PKJ assembly. A M8x70 hexagonal socket bolt secured by a M8 nylon lock nut joins the lattice assembly to the shell. The M8 bolt serves as the PKJ's single axis of rotation requiring a nylon insert lock nut to prevent the assembly from loosening during rotation. Four M5x30 hexagonal socket bolts with M5 washers are used to secure the lattice region to the pyramid interface. The bolts thread directly into the pyramid interface which is designed with undersized holes to allow engagement of threads. Additionally, an M5x20 Hex Socket Bolt with M5 nut is required to for the tube clamp identified in following Figure 4-11.

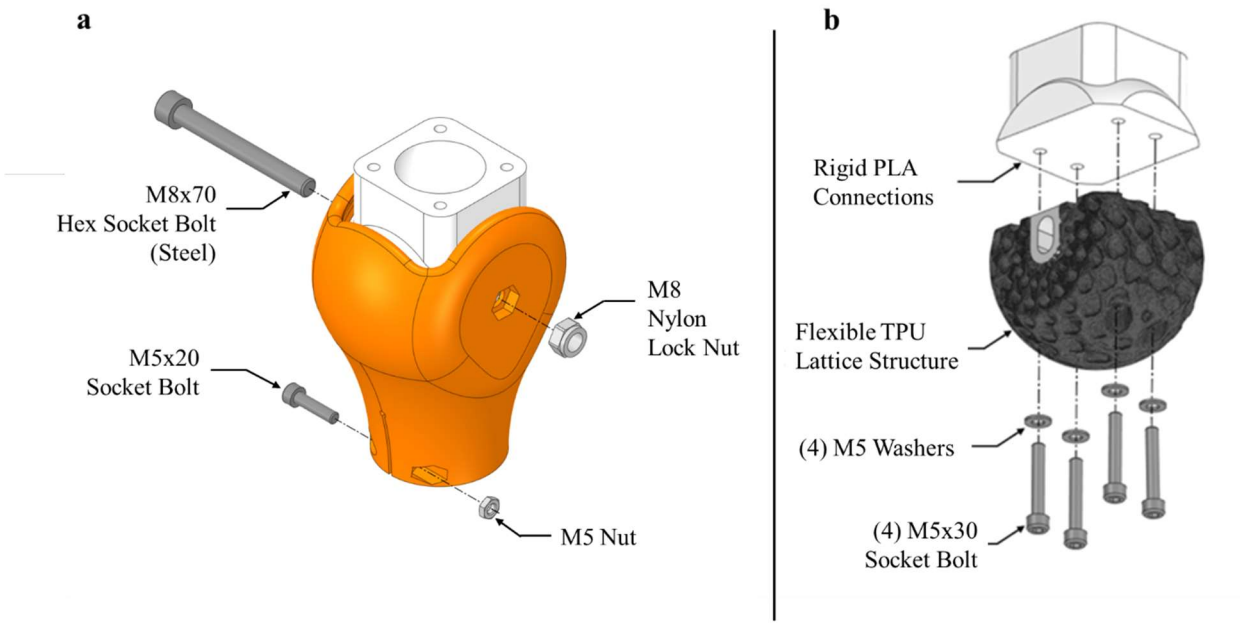

Figure 4-10. Exploded view of hardware components (a) PKJ assembly (b) Lattice assembly.

Both the shell and pyramid interface are designed with standard prosthetic interfaces allowing for "plug and play" functionality with existing commercial adapters. Figure 4-11 identifies a standard 4-hole pattern designed into thy pyramid interface component. The holes designed into the pyramid interface are undersized at 0.47mm diameter allowing for M5 bolts to be threaded directly into the part. A standard 30mm tube clamp is designed into the shell and utilizes an M5 bolt and nut to generate clamping force on the pylon.

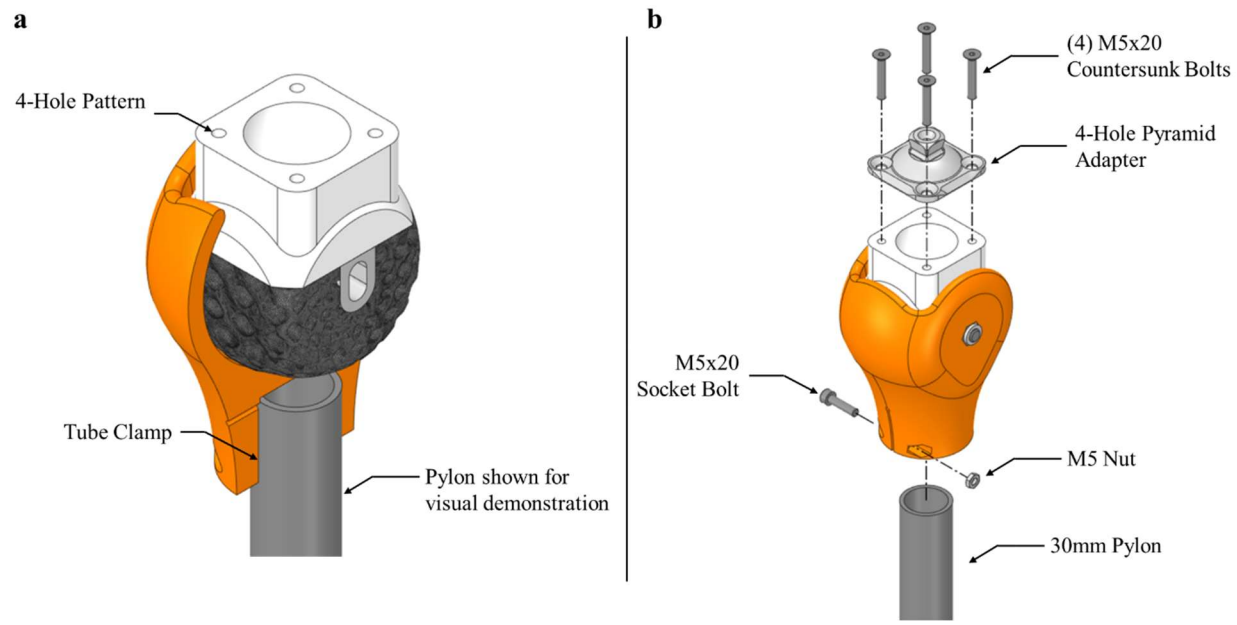

Figure 4-11. ***(a)*** *Identification of commercial interfaces.* ***(b)*** *Exploded view of commercial components.*

For visual demonstration Figure 4-11 includes a standard 4-hole pyramid adapter and a 30mm pylon. It must be noted these are commercial prosthetic components shown and are not part of the designed PKJ.

Range of Motion

The PKJ's single axis is defined by the M8 bolt allowing for rotation between the shell and inner lattice assembly. The PKJ is designed to swing freely with a range of motion of 10-degree extension to 120-degree flexion shown in Figure 4-12. The design represents the required human knee range of motion (ROM) for normal activities defined in Section 2.4.9.

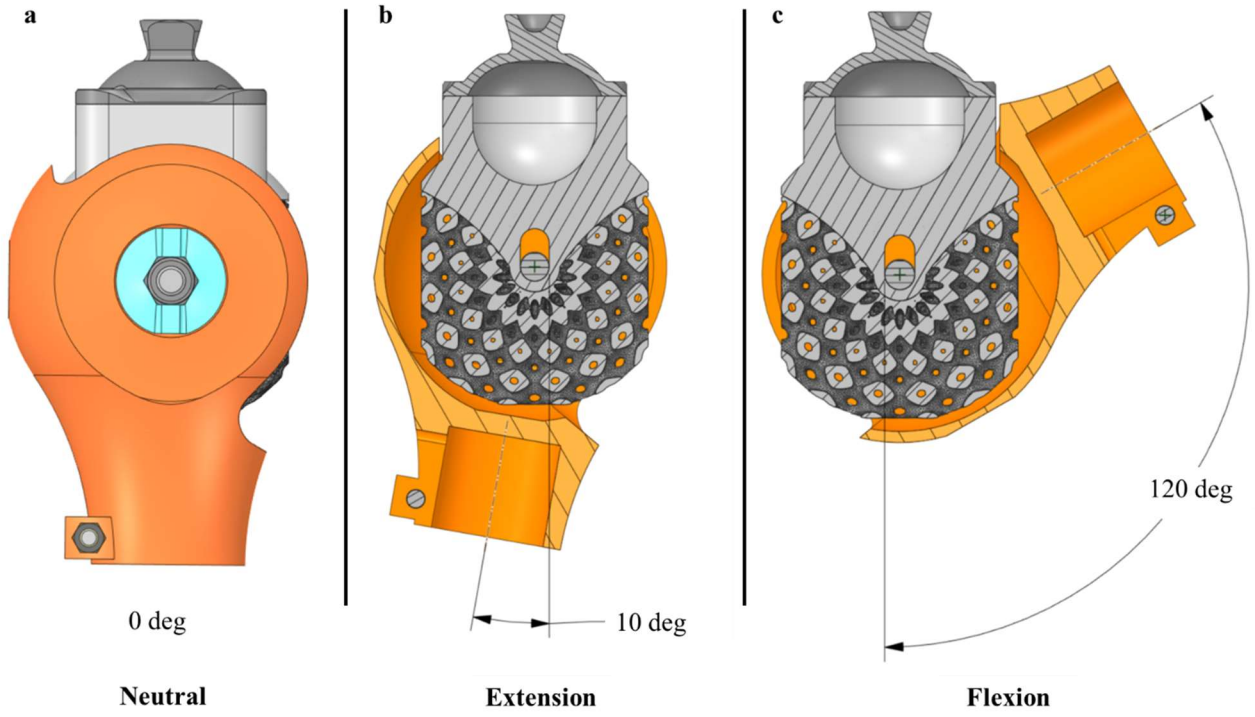

Figure 4-12. Range of motion. (a) PKJ at resting neutral position of 0 degrees. (b) section view of PKJ in extension of 10 degrees. (c) section view of PKJ in flexion of 120 degrees.

Rate Control and Stance Control

Mechanical friction can be imparted through tightening of M8 bolt adjusting the gap between the shell side wall and the lattice assembly. The friction can be adjusted until the rate at which the PKJ swings matches the user's natural gait or until the PKJ is fully constrained and unable to rotate. Figure 4-13 provides a cross-section view detailing the gap between the lattice assembly and the shell.

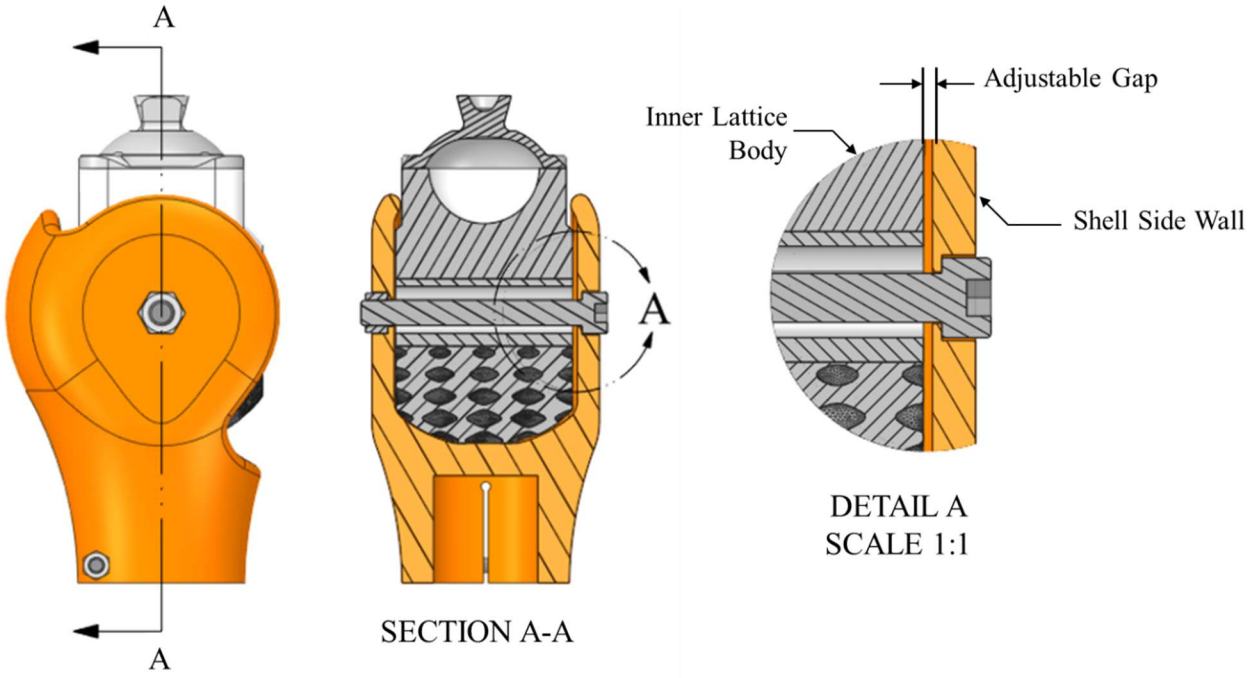

Figure 4-13. Detail view identifying adjustable gap between shell and lattice body.

4.2.2 Lattice Design

The following section will discuss the design of the lattice region identified in Figure 4-14 which is a subcomponent of the inner lattice assembly.

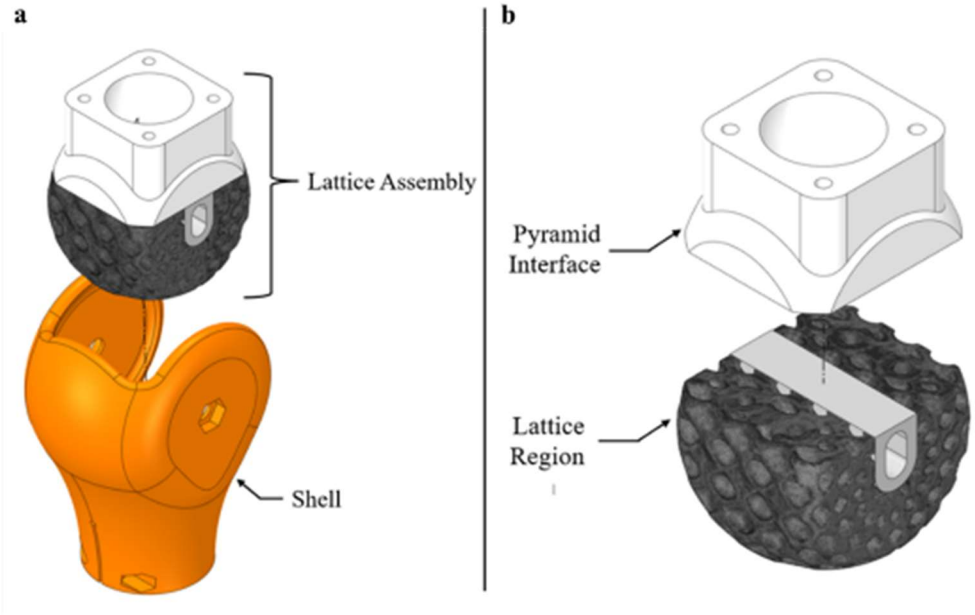

Figure 4-14. (a) Identification of Inner lattice assembly. (b) Identification of lattice region.

4.2.2.1 Lattice Type Selection

Schwarz lattice cells were selected for the design of the lattice region's structure. Within the lattice structure, each individual lattice cell is referred to as a unit cell and together the unit cells construct a lattice structure (see Section 2.4.1 for more details of lattice background). The deformation of the lattice structure is dependent on the location of the applied load allowing for each unit cell to deform individually based on shifting postures of the user.

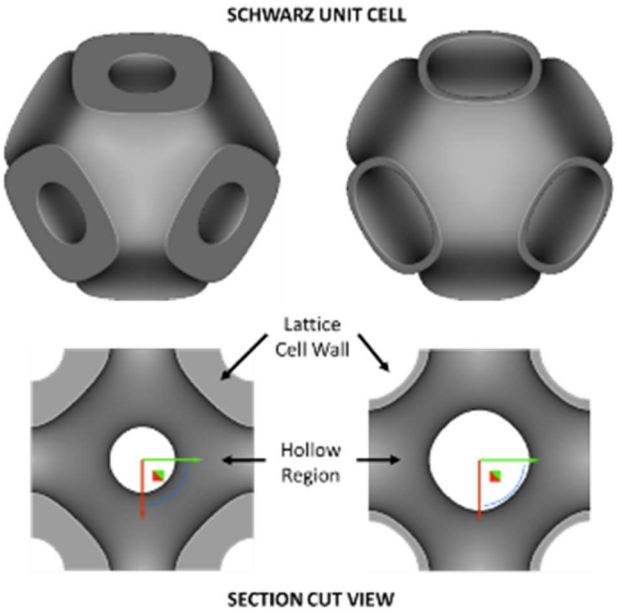

Figure 4-15. Schwarz unit cell section cut view: wall thickness versus hollow region.

Furthermore, the Schwarz unit cells are arranged as a cylindrical structure (see Figure 4-16) where cells increase in size as the distance from the axis increases. When load is applied along the perimeter of the structure, the exterior cells experience increased deformation and responsiveness.

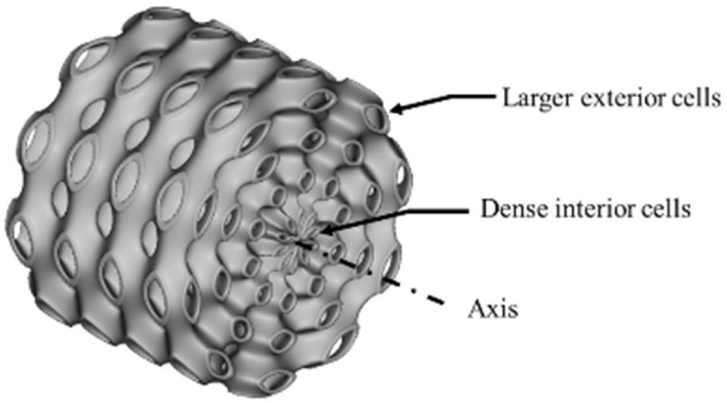

Figure 4-16. Illustration of cylindrical TPMS structure's change in cell size.

As stated in Section 2.4.2, the dome structure of schwarz cells allow for economical distribution of compressive stresses and enhanced mechanical properties compared to traditional beam structures. Geometrically the Schwarz lattice structures consist of a sloping continuous interior surfaces eliminating severe overhangs and the need for support structures during 3D printing resulting in faster 3D printing production and less wasted material.

4.2.2.2 Lattice Modelling

Lattice modelling utilized two different softwares discussed below:

Fusion 360 Software

The lattice region was first modeld with Fusion 360 software to define the geometry and bounding volume. The lattice region was modeled with selectable, separate CAD bodies identified as solid regions and lattice regions (colored red and blue respectively in Figure 4-17). Solid regions were distinguished as features that must retain their current geometry. The solid regions coorelate to locations where bolts must pass through as previously defined in Figure 4-10. The solid regions were not be altered and were unioned to the lattice region after lattices are modeled. The lattice region was re-modeled with lattices in nTopology software and defines the bounding volume of the lattice structure.

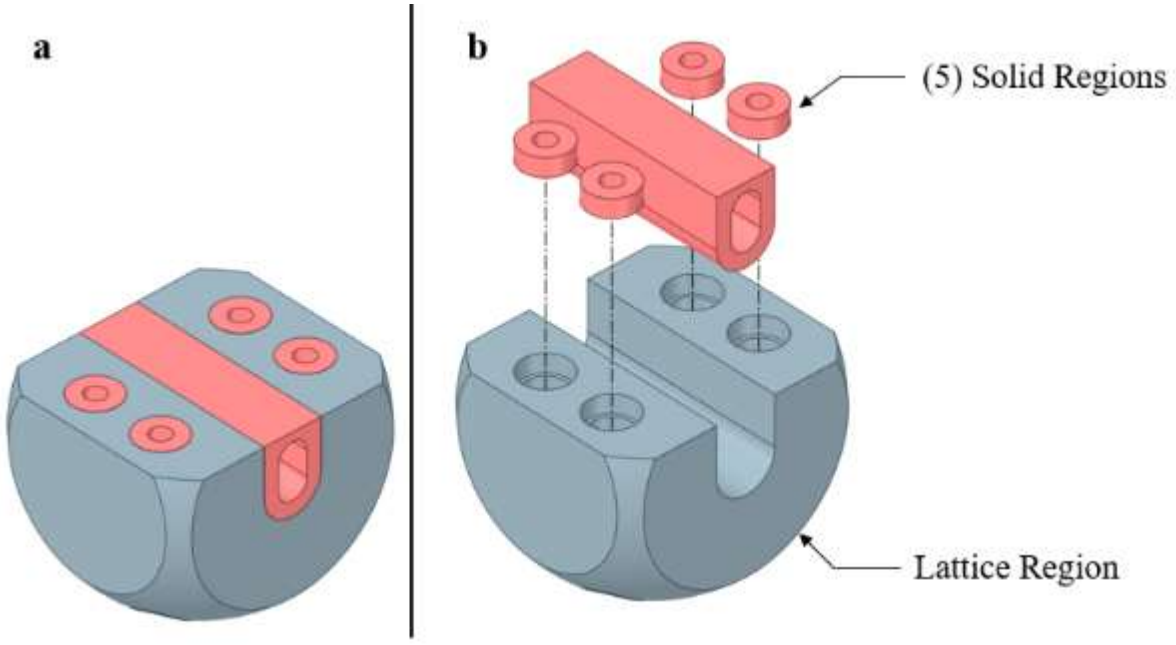

Figure 4-17. Exploded view of solid regions and lattice region.

nTopology Software

nTopology software was used to convert the lattice region to a Schwarz lattice structure through the following outlined steps. Figure 4-18 provides screen captures from nTopology illstrating Steps 1 through 4.

Step 1: Import CAD body containing both the lattice region and solid regions

Step 2: Select the lattice region for modelling

Step 3: Define lattice parameters that generates a structure which conforms to the lattice region

Step 4: Union solid regions with new lattice structure to create a monolithic part

Step 5: Characterize the lattice structure through nToplogy simulation

Step 6: Repeat Step 4 and Step 5 until desired mechanical properties are met

Step 7: Export the part

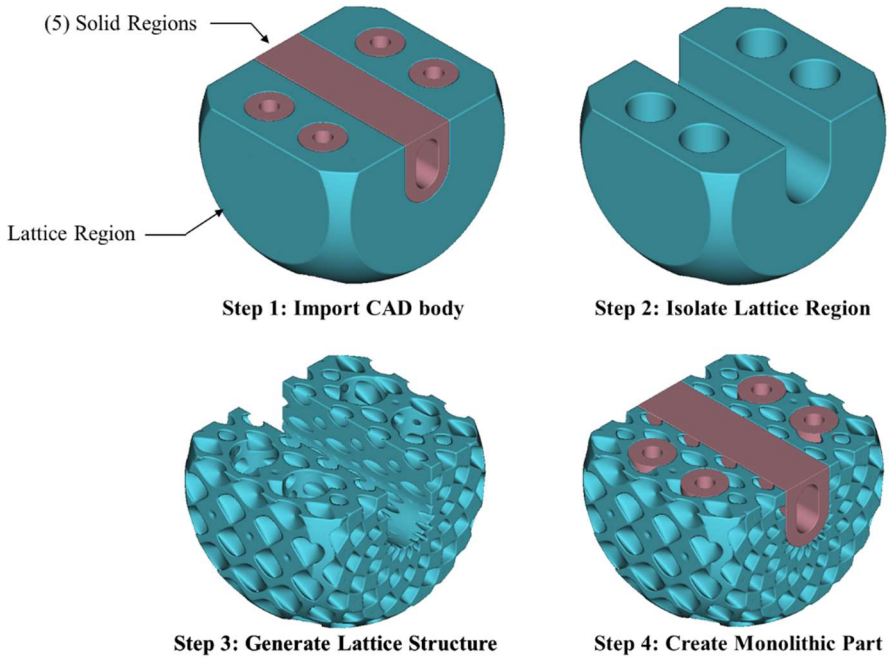

Figure 4-18. Lattice modelling steps within nTopology software.

Lattice parameter definition in Step 3 required a trial-and-error process. Lattice parameters were readjusted until a confoming lattice was generated with no thin or unconnected overhangs on the exterior of the structure. Figure 4-19 below is provided to compare the Schwarz structure to a traditional beam lattice structure whose geometry poorly conforms to rounded volumes. The result is unconnected exterior beam suspected to buckle under load:

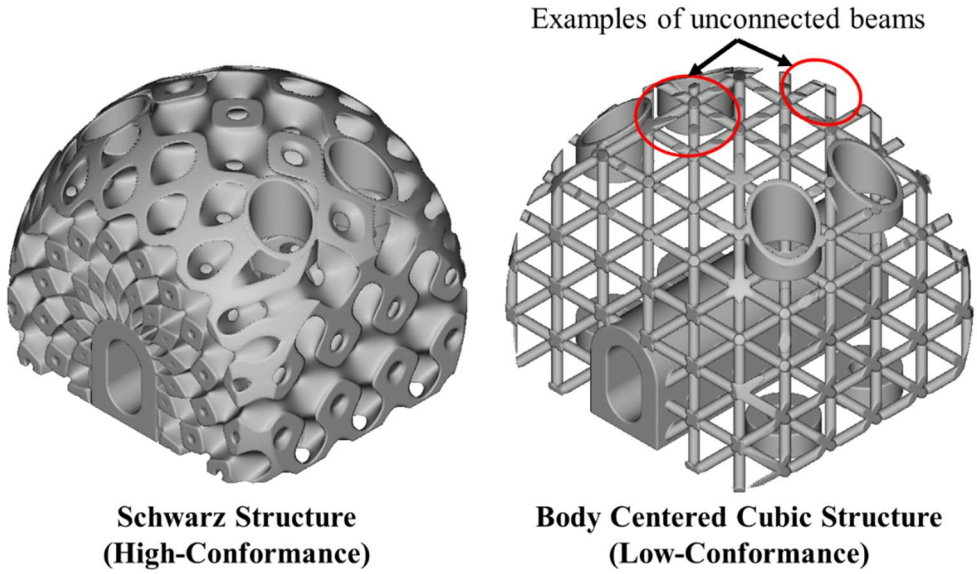

Figure 4-19. Example of high-conformance and low-conformance structures.

The following Figure 4-20 is provided for knowledge transfer to illustrate the relationship between each parameter and a cylindrical Schwarz structure:

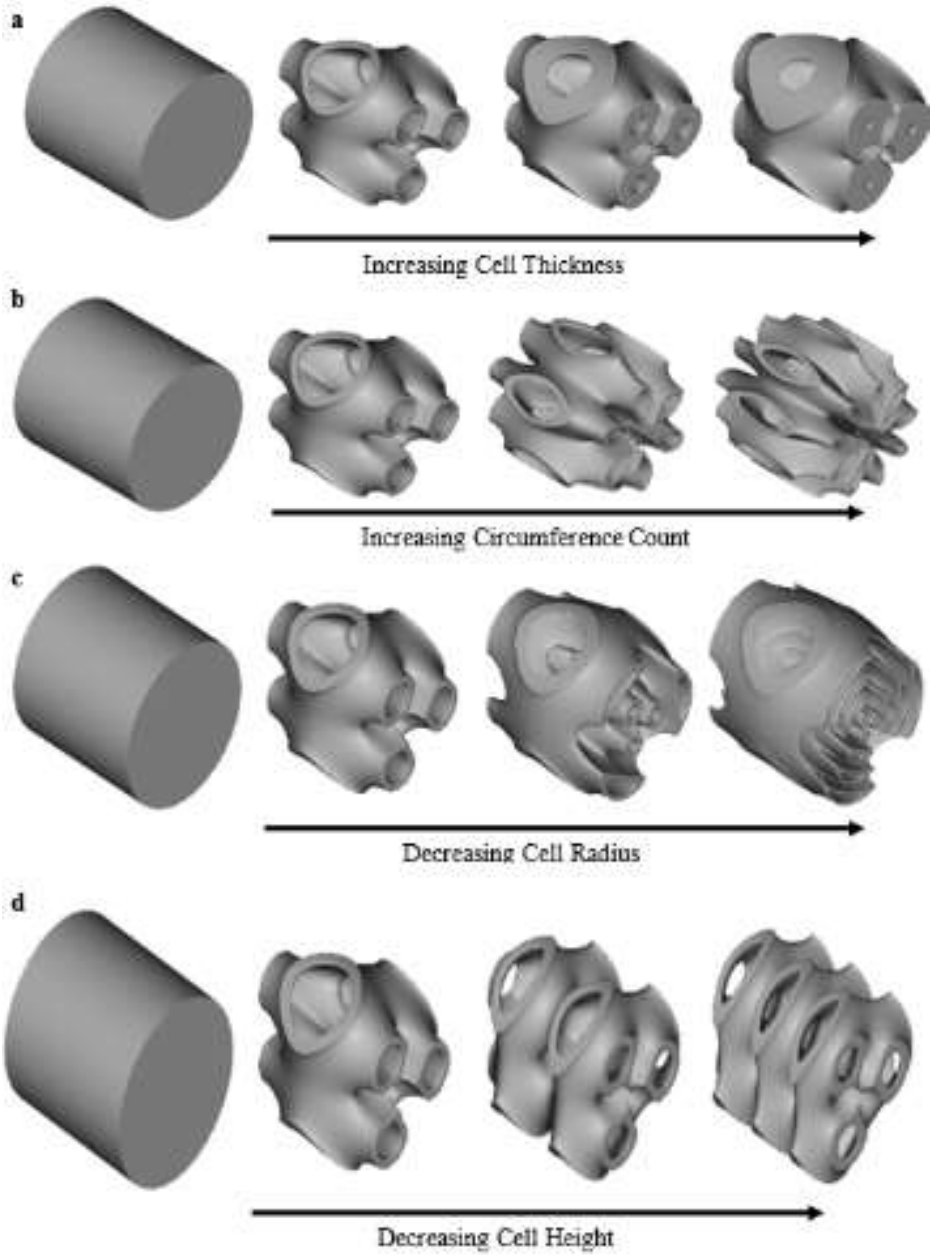

Figure 4-20. Cylindrical TPMS structure parameters. (a) Increasing cell thickness. (b) Increasing circumference count. (c) Decreasing cell radius. (d) Decreasing cell height.

The designed PKJ's lattice region is defined with parameters listed in Table 4-3. The parameters were selected based off of simulation results in Section 4.3.1 evaluating the structure's mechanical performance. The parameters listed in Table 4-3 result in a lattice region with the lowest stiffness, yet could meet load requirements from Section 2.4.10 without permanent deformation.

Table 4-3. Final Cylindrical TPMS Parameters for Lattice Body

Parameter	Input
Lattice Type:	Walled TPMS Cylindrical
Circumference Count	16
Radius Cell Size	8mm
Height Cell Size	14mm
Cell Wall Thickness	1.6mm
Fill Type:	Schwarz

4.2.2.3 nToplogy Export

After modelling, the lattice structures must be meshed in nToplogy to export the part. As stated by nTopology, the complex geometry of lattices requires a high number of faces to capture the shape [66]. The single 10x10x10 unit cell below requires 588 nodes and 452 faces:

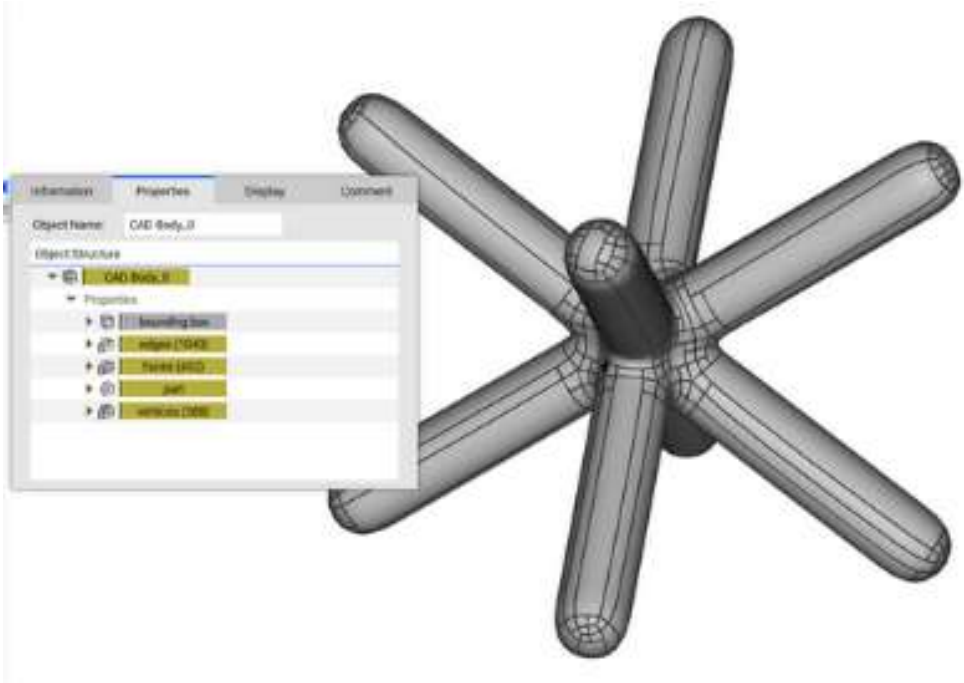

Figure 4-21. Example of high face requirement for a single unit cell [66].

The designed lattice region from Section 4.2.2 requires 1,318,342 faces / 658,421 vertexes to create a high-fidelity mesh (see Figure 4-22) and can be reduced to 157,984 faces / 78,602 vertexes if loss in fidelity is acceptable (see Figure 4-23).

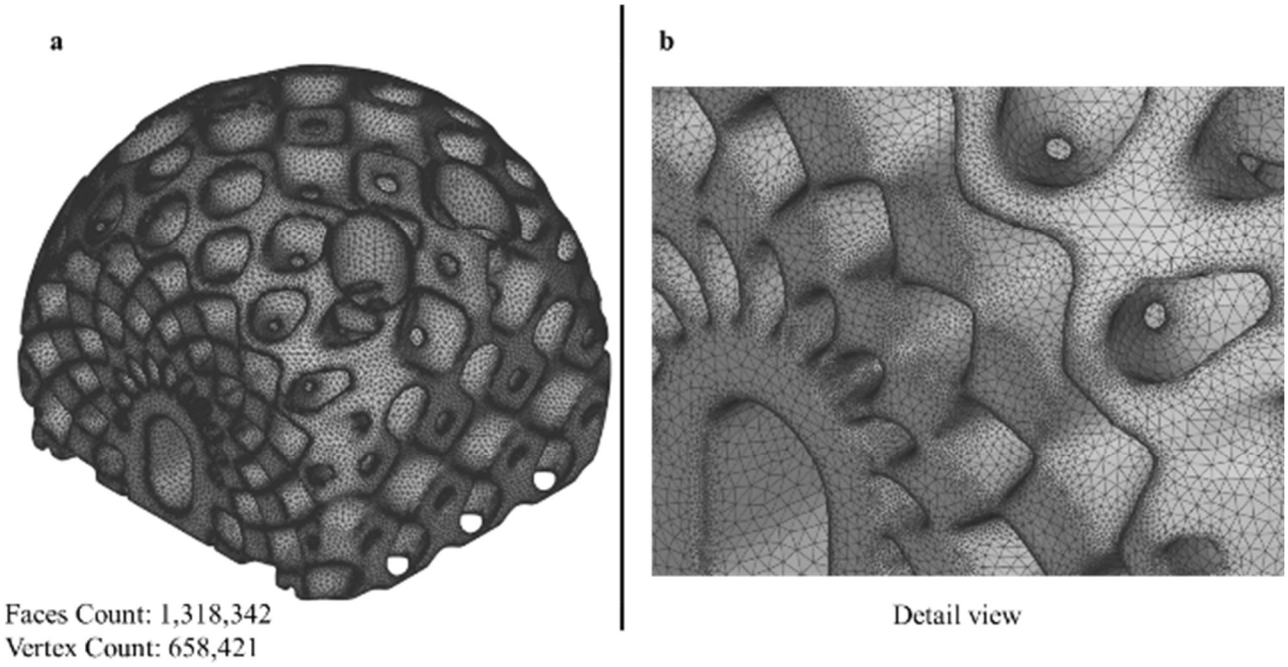

Figure 4-22. Lattice Region with high-fidelity mesh.

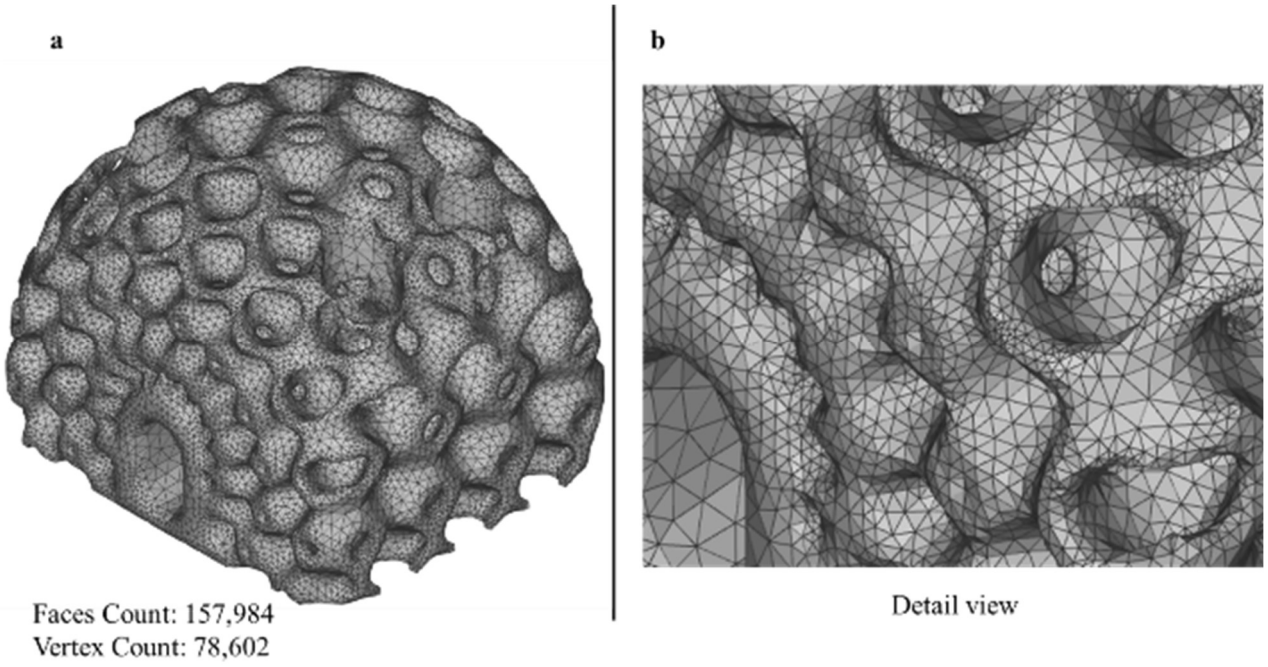

Figure 4-23. Lattice region with low-fidelity mesh.

nTopology can efficiently accommodate the millions of meshed elements allowing for the part to be exported as a high fidelity STL file for 3D printing. However, nTopology is unable to generate a CAD part required to export the part to external simulation software. While it is feasible to convert

a faceted STL file to a solid body within Ansys SpaceClaim at the cost of computational resources, structural simulation within Ansys Mechanical is limited to a maximum of 128K faces/vertexes and therefore cannot generate the required mesh [67].

Therefore, all lattice region simulations for Section 4.3.1 will be performed within nTopology software and will not be simulate as part of the complete PKJ assembly. Section 4.3.1 simulations will be performed with the high-fidelity mesh shown previously in Figure 4-22.

4.3 Simulation

4.3.1 Lattice Simulation

The following simulations were performed in conjunction to Section 4.2.2 to characterize how the lattice region will respond to different load cases in pair with varying parameters.

As stated in Section 4.2.2, nTopology lattice structures cannot be exported to external simulation software. The following sub-sections characterize the lattice region's stiffness and evaluate the lattice region's strength. The lattice region was simulated against ISO 10328:2016 load condition I which is the highest prescribed ultimate test force. It must be noted that nToplogy cannot apply the remote boundary conditions defined in Section 2.4.10.

4.3.1.1 Lattice Region Density (LRD)

The lattice region component with modeled lattice structure is characterized by the volume of modeled lattice versus the volume of the original solid lattice region. nTopology software was utilized to calculate the lattice volumes used for Equation 1 below. This characterization will be referred to as Lattice Region Density (LRD):

$$Lattice\ Region\ Density\ = (Volume_{Lattice}/Volume_{Solid\ Body}) * 100 \qquad (1)$$

Various lattice modelling parameters impact the lattice volume. As the volume of lattice increases, more material from the original lattice region is retained increasing the LRD. The LRD is positively correlated to parameters unit cell type, number of cells and cell thickness defined in previous Figure 4-20. Figure 4-24 displays cross-section views of increasing LRD as the wall thickness changes:

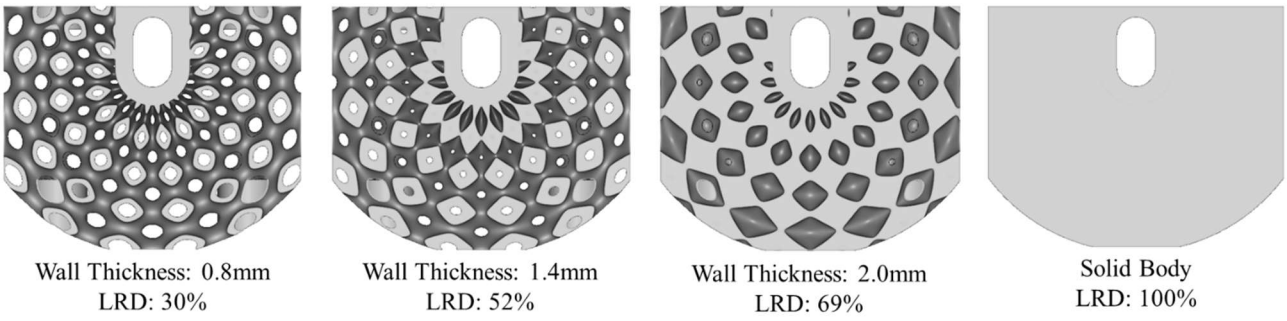

Figure 4-24. Visual comparison of increasing LRD values.

4.3.1.2 Simulation Definition

The lattice region was simulated in nToplogy with constant parameters defined in previous Table 4-3 and varying wall thicknesses relating to LRD values defined in Table 4-4 below. The minimum LRD value of 30% was selected as it relates to a lattice wall thickness value of .8mm. This research project utilizes a .6mm nozzle for additive manufacturing and LRD of 30% ensures successful fabrication of the structure's walls as the 3D printer will be required to make at least two passes to build the thickness.

Table 4-4. Definition of LRD Values for Lattice Simulation

LRD	**30%**	**37%**	**45%**	**52%**	**59%**	**64%**	**69%**
Corresponding Wall Thickness	.8mm	1.0mm	1.2mm	1.4mm	1.6mm	1.8mm	2.0mm

For all simulations, load was applied to the top of the lattice structure representing the compression plate used for experimental testing (see Figure 4-41). Figure 4-25 identifies locations of the boundary conditions and load direction. The lattice region was simulated with the high-fidelity mesh from previous Figure 4-22.

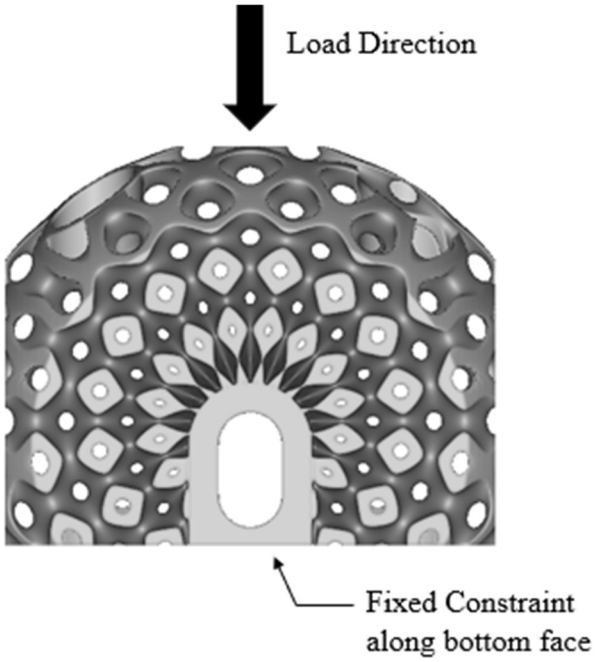

Figure 4-25. Boundary conditions for lattice characterization.

4.3.1.3 Lattice Characterization

Simulation was performed with nTopology software on the lattice region with modeled lattice structures to characterize the structures stiffness as a function of LRD.

The stiffness of each LRD is calculated as shown in Equation 2 and is plotted in Figure 4-26. As the structure's density increases, the stiffness increases exponentially as a result of more material and more rigid lattice cells:

$$Stiffness = Load/Displacement \quad (2)$$

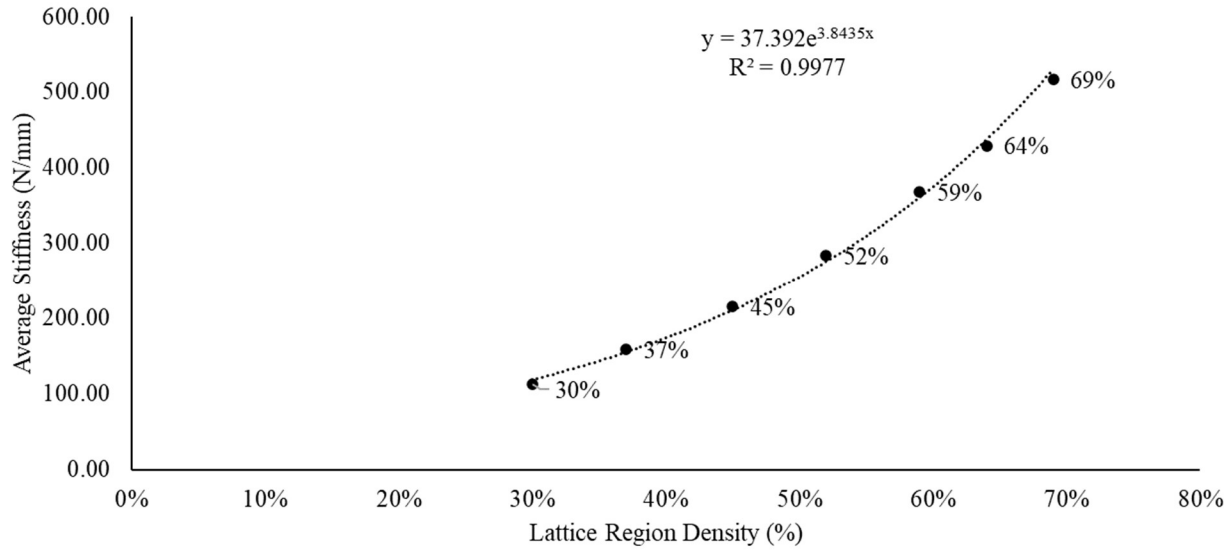

Figure 4-26. Stiffness-LRD plot from nTopology simulation.

Figure 4-27 displays force-displacement plot for the simulated LRD values with stiffness equating to the slope of each LRD line. Each LRD tested displays a linear relationship between load and displacement.

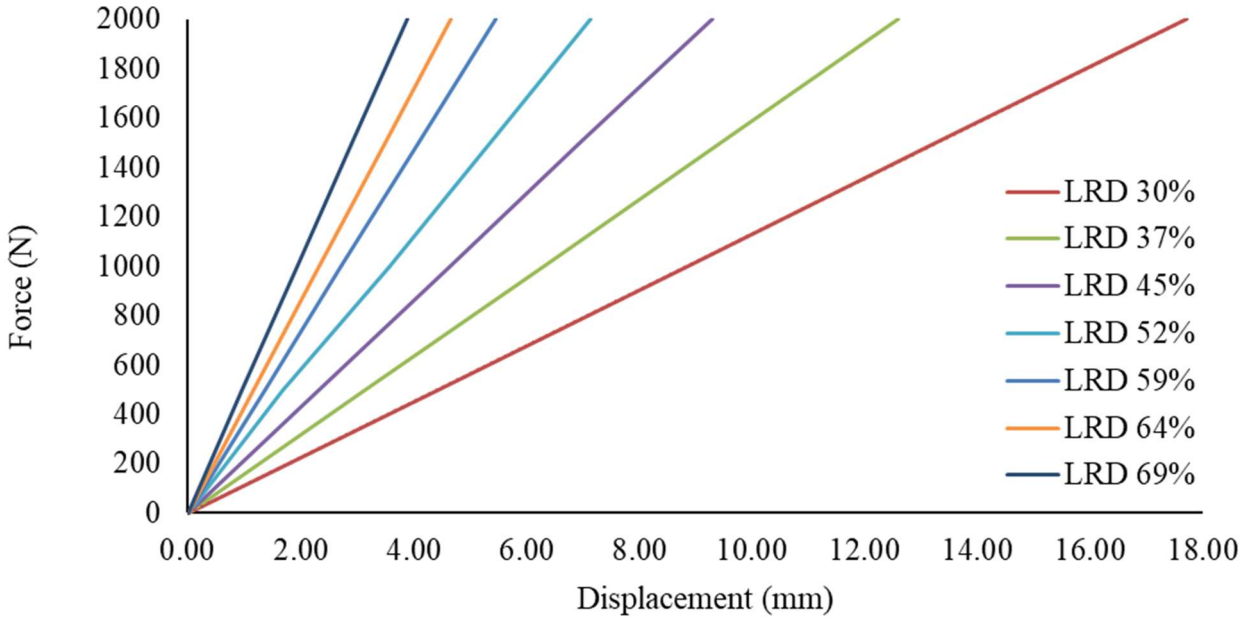

Figure 4-27. Force-Displacement plot from nTopology simulation for different LRD values.

4.3.1.4 Lattice Strength Evaluation

Figure 4-28 presents load condition III cross-section views of the simuluation results, which applies a load representative of normal use. Von Mises stress plots are set with maximum value of 6 MPa to

identify where stress is greater than the yield strength of 5 MPa for eSun eFlex material. For LRD values 45% and greater the structures are expected to compress and elastically return to original shape as all stresses are below 5 MPa. No permanent deformation is to be expected. Permanent deformation is expected along the exterior cells of LRD 30% and LRD 37% and are not deemed viable for the PKJ load requirements defined in Section 2.4.10.

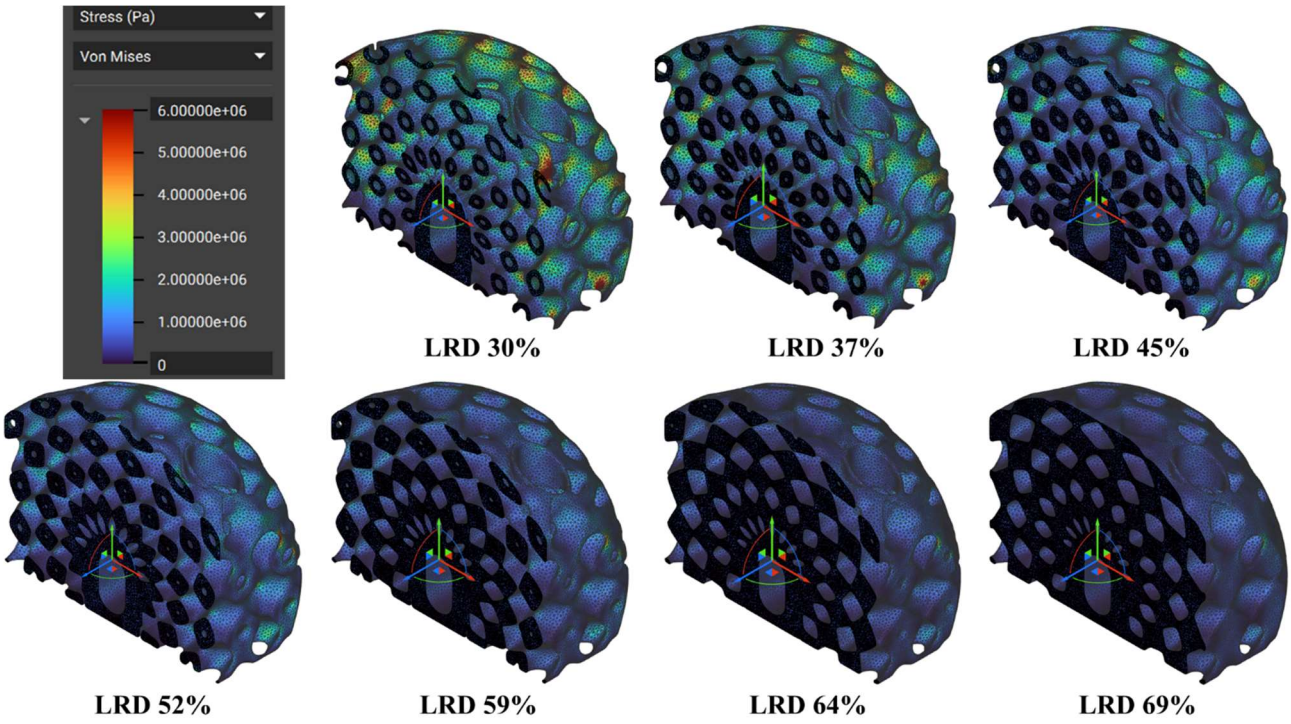

Figure 4-28. Cross-section views of lattice region simulated for load condition III.

Figure 4-29 presents cross-section simuluation results for load condition I, which applies an ultimate load defined by ISO 10328:2016 representing an extreme loading scenario. Von Mises stress plots are set with maximum value of 31 MPa to identify where stress is equivalent to ultimate tensile strength eSun eFlex material. For LRD values 45% to 52% the structure expected to withstand the load without failure, however, permanent deformation is expected to occur as stresses exceed the material yield strength. Examination of the cross-sectional area identifies that permanent deformation is to occur primarily for exterior cells where stress is highest. LRD values of 59% and greater are recommended for the PKJ design for a 100 kg user as no permanent deformation will occur and the structure is expected to elastically return to its original shape after ultimate load conditions.

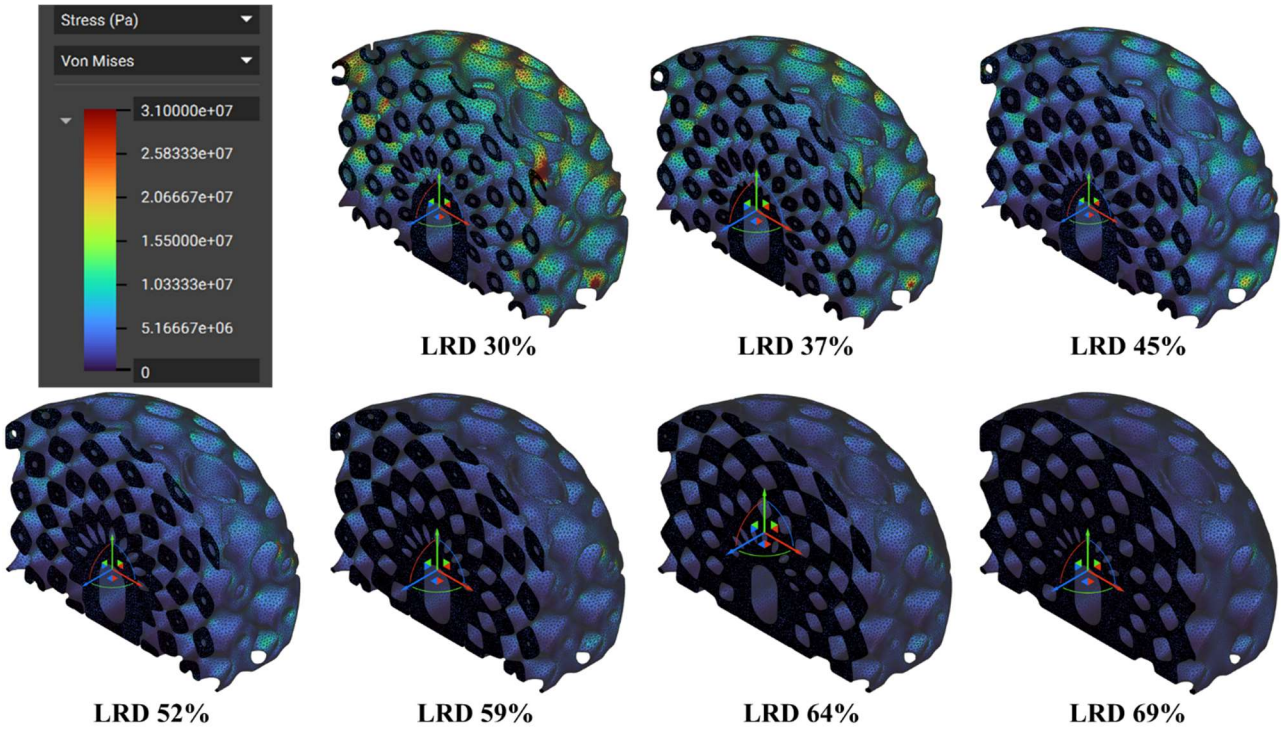

Figure 4-29. Cross-section views of lattice region simulated for load condition I.

For all LRD values it is observed that stresses are not uniform throughout the structure and that stresses are greatest at the exterior unit cells. Cross-section views of the structure (see Figure 4-30) display that the size of unit cells increases as the distance from the axis increases. Additionally as the distance from the axis increases the cells become less densely packed resulting in the cell geometry to flatten. Cells closely packed at the axis are shaped as an ovoid (egg-shaped object). Bioscience researchers examining strengths of eggs quantify that “the sharper the curve of an ovid (egg-shaped object), the stronger and more rigid it is at its tip) [68]. This phenomenon is utilized in structural arches which distribute load down the curved sides and reduce stress concentrations.

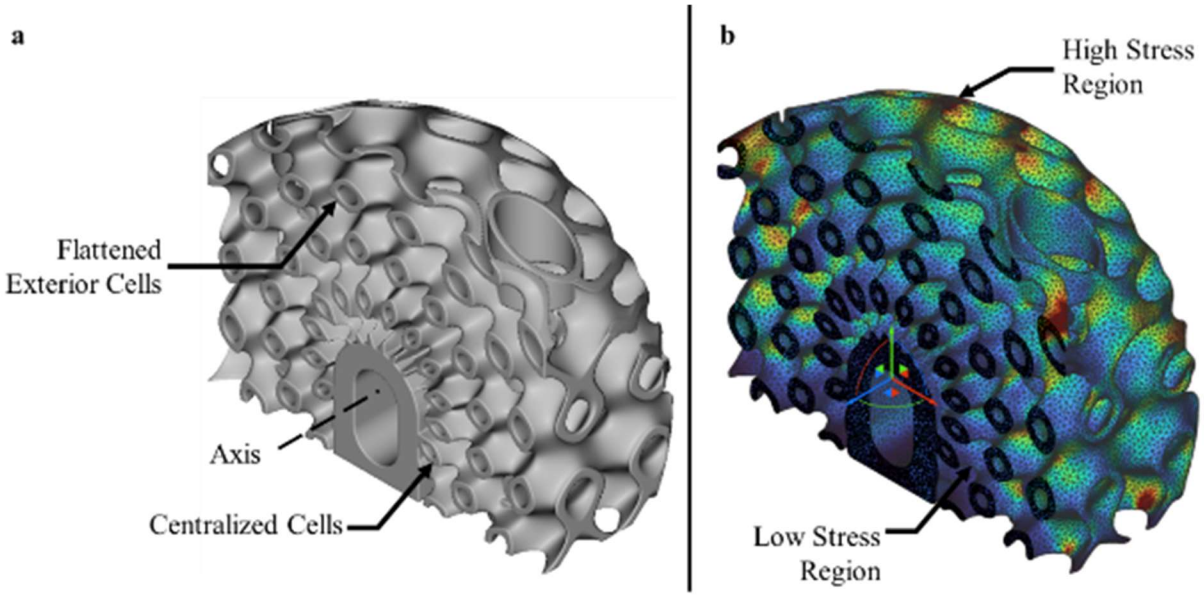

Figure 4-30. (a) Varied cell geometries. (b) Identification of changing stress values.

4.3.2 PKJ ASSEMBLY SIMULATION

Two rounds of simulations were performed. Round I served as an initial evaluation of the PKJ assembly to identify redesign areas of the shell based off resulting stresses. Round II simulated the redesigned shell to display compliance with load requirements.

4.3.2.1 Simulation Definition

A lightweight PKJ assembly omitting hardware components was used for simulation to reduce model complexity. As stated in Section 4.2.2, the lattice region with modeled lattice structure cannot be simulated in Ansys Mechanical and therefore a solid lattice region (LRD 100%) was used in place which is defined as flexible eSun eFlex material. While the the lattice region is not simulated with a modeld lattice strucutre, the simulation results provide insight on how interactions between components of various materials will distribute the applied stress. Figure 4-31 below identifies the components and defined materials for the PKJ assembly simulation. See Section 4.1 for detailed information of eSun filament material properties.

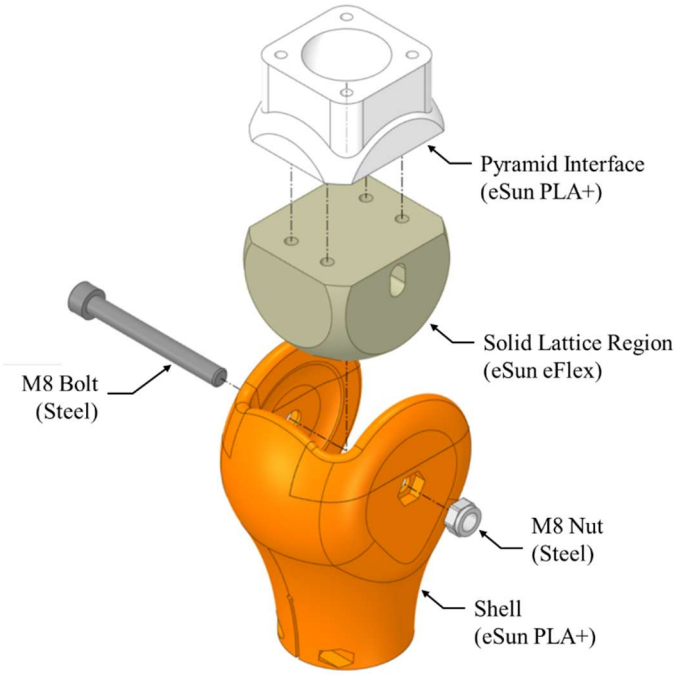

Figure 4-31. Lightweight PKJ Assembly for Ansys structural simulation.

Mesh

An iterative loop of running simulation, then refining mesh in areas of stress concentrations was performed resulting in the following multi-size mesh (see Figure 4-32). Simulation was constrained by an Ansys Mechanical Student License limiting mesh to 128,000 faces/vertexes and therefore a refined mesh could not be applied to all regions of the PKJ assembly without exceeding the numerical license limit. Techniques of splitting bodies, surface refinement, edge refinement, and virtual topology were utilized to minimize stress concentrations while staying within the license limits. The final mesh utilized 72,212 triangular elements and 125,504 nodes ranging in size from 1.85mm to 5.0mm.

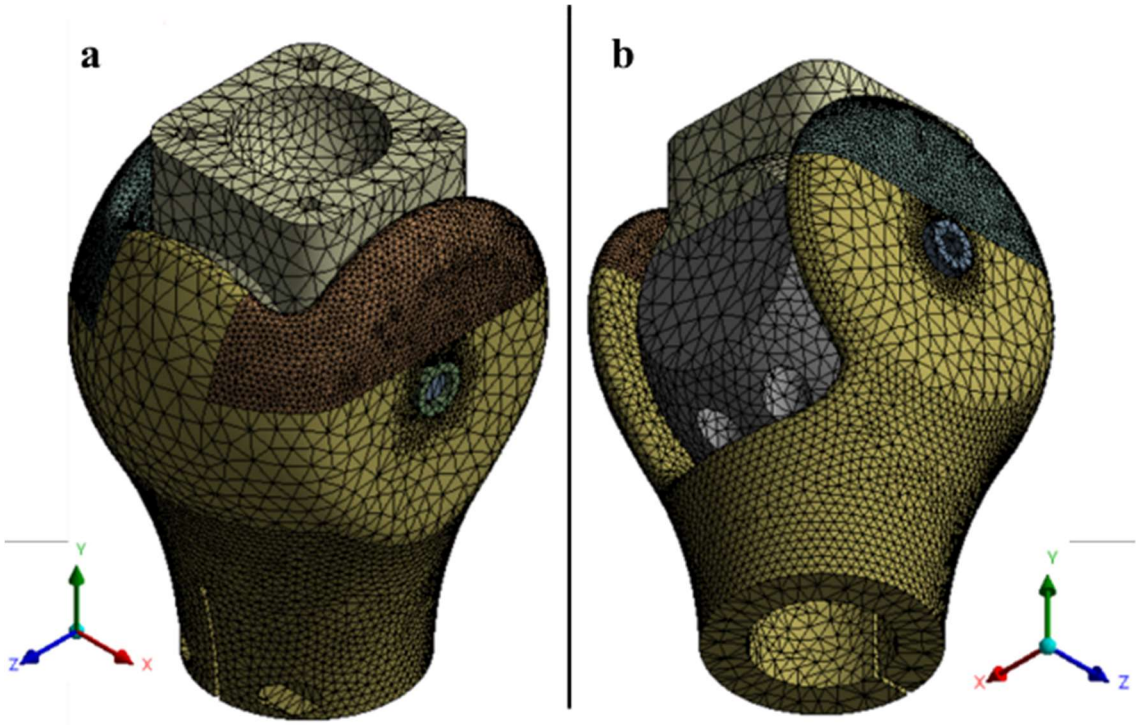

Figure 4-32. PKJ Assembly with mesh refinement.

Boundary Conditions

For all load conditions, the applied force was scoped to the top surface of the pyramid interface and the fixed constraint scoped to the tube clamp as shown in Figure 4-33. Bonded contacts were applied to the pyramid interface and the lattice region to represent bolt connections and all other component contacts were defined as without penetration. For load condition III, load was applied normal and directly to the load face shown in Figure 4-33.

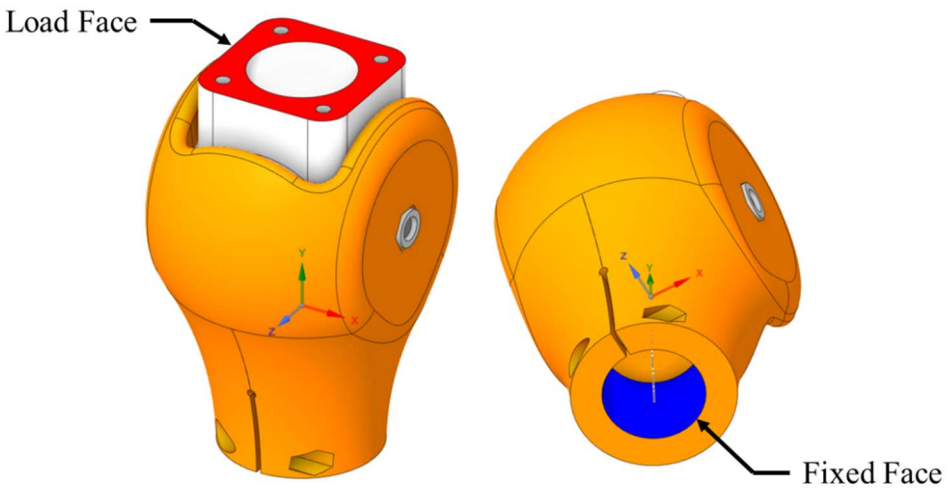

Figure 4-33. Identification of boundary condition faces.

For load condition I and load condition II, remote loads were applied to the force face and remote constraints were applied to the fixed face (see Figure 4-34).

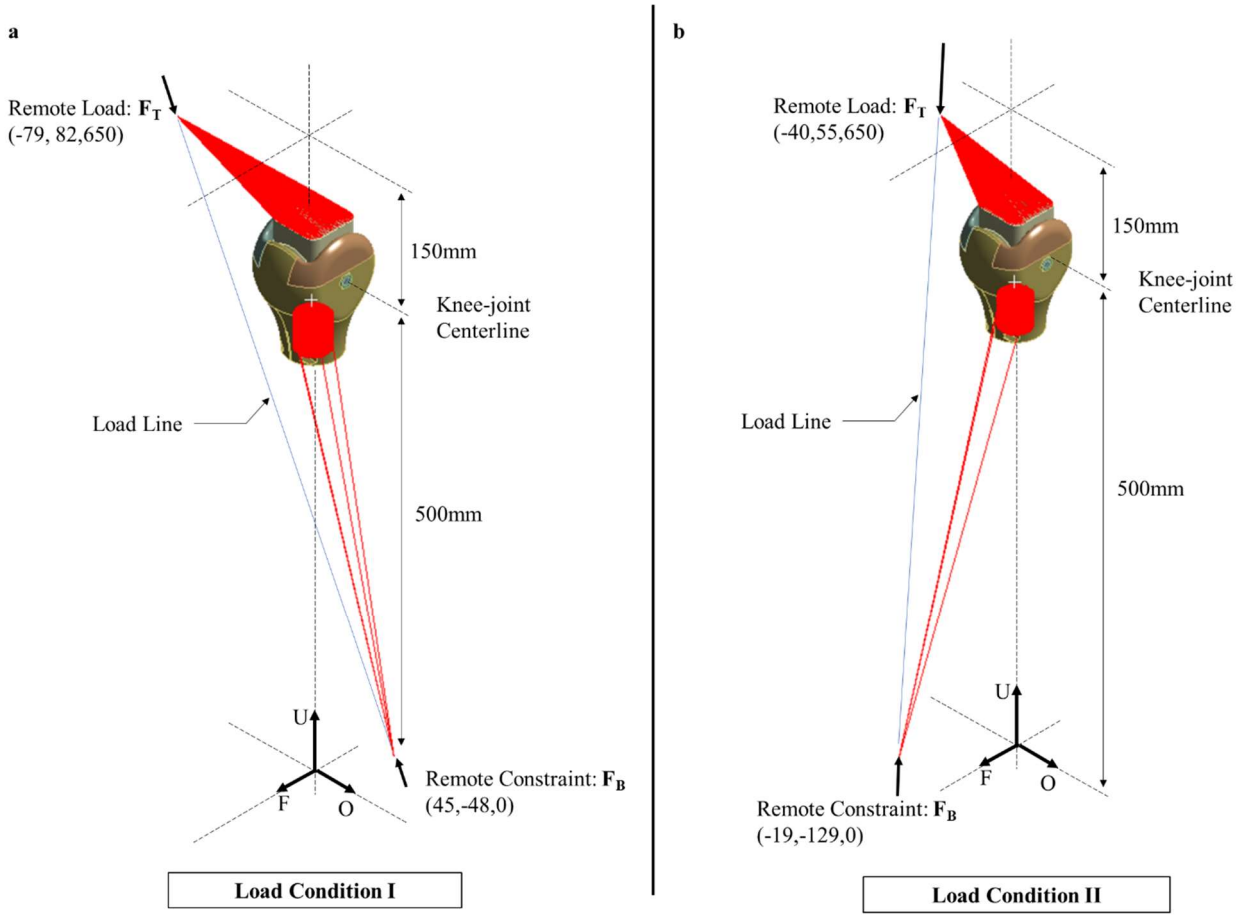

Figure 4-34. ISO 10328:2016 remote offsets (a) Load condition I. (b) Load condition II.

4.3.2.2 Simulation Results

Results – Round I

Simulation for load condition I was performed for Round I. Results indicated that max loads will be applied at the corners of the shell (see Figure 4-35). Results indicated expected part failure of original shell design as resulting stress of 120 MPa exceeded the ultimate tensile strength of 61 MPa for eSun PLA+.

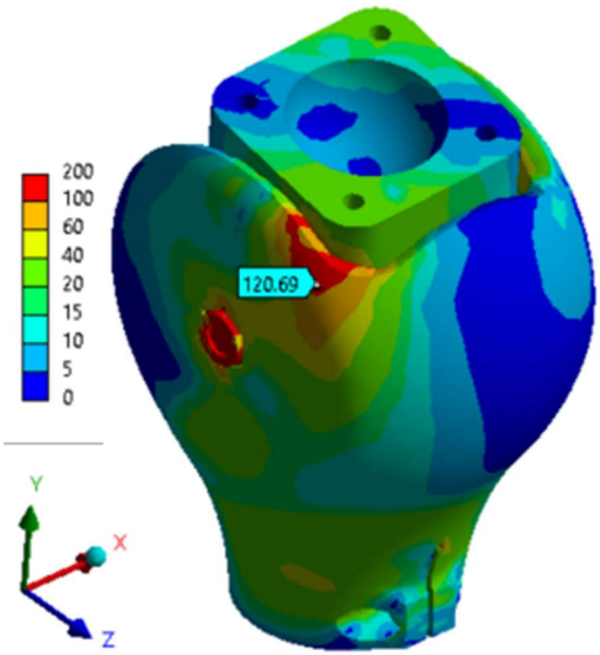

Figure 4-35. Expected location of failure for load condition I.

Round I simulation additionally served to identify the component interaction between pyramid interface and shell indicating that the shell will be loaded in the XZ directions as the pyramid adapter displaces in the -X and +Z directions. Part orientation during 3D printing is discussed in Section 4.4**Error! Reference source not found.** to optimize the 3D printed shell based off the lateral loads.

The shell was redesigned with thicker walls to accommodate the high stresses. Cross-section views are provided in Figure 4-36 showing the shell before and after redesign.

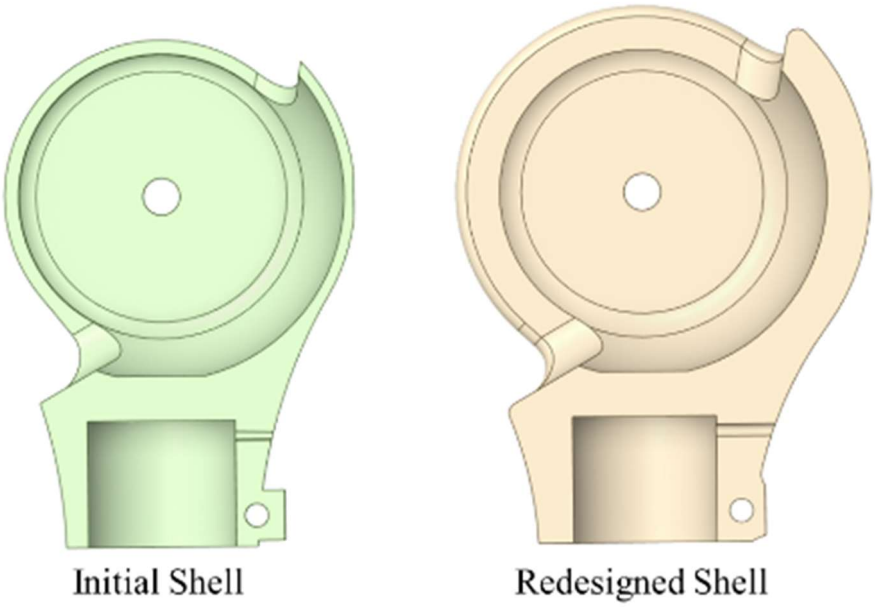

Figure 4-36. Redesigned shell based off round I simulation results.

Results – Round II

Round II simulated the redesigned, final shell for load conditions I, II, and III.

For all load conditions, load condition resulted the maximum stress of 30 MPa in the 3D printed shell (see Figure 4-37). As the stresses within the shell are below the ultimate tensile strength for eSun eFlex (61 MPa), the PKJ assembly is expected to withstand all load conditions. For load condition I the FOS is greater than 1.5 indicating that the part is expected to withstand extreme load case without deformation or failure (see Figure 4-38).

Note:

- Stress plot legends are scaled to a maximum value of 65 MPa to identify failure within the 3D printed parts. If failure was to occur, the 3D printed components will fail before the steel parts and therefore this analysis omits the stresses within the bolt and nut.
- High stresses within the solid lattice region are driven by poor mesh quality as the solid lattice structure serves as a place holder for the lattice region designed in Section 4.2.2.

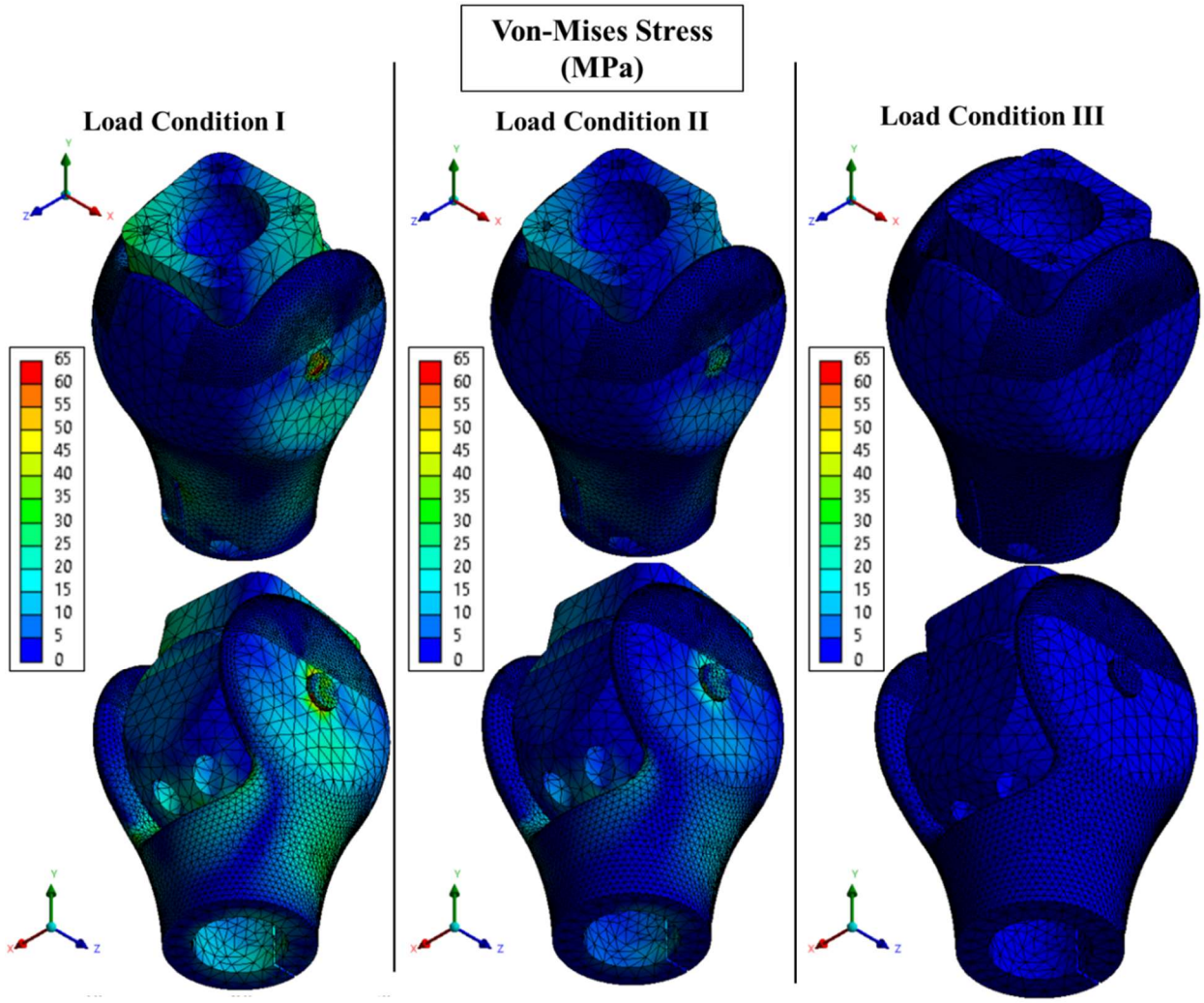

Figure 4-37. Simulation von-Mises stress plot.

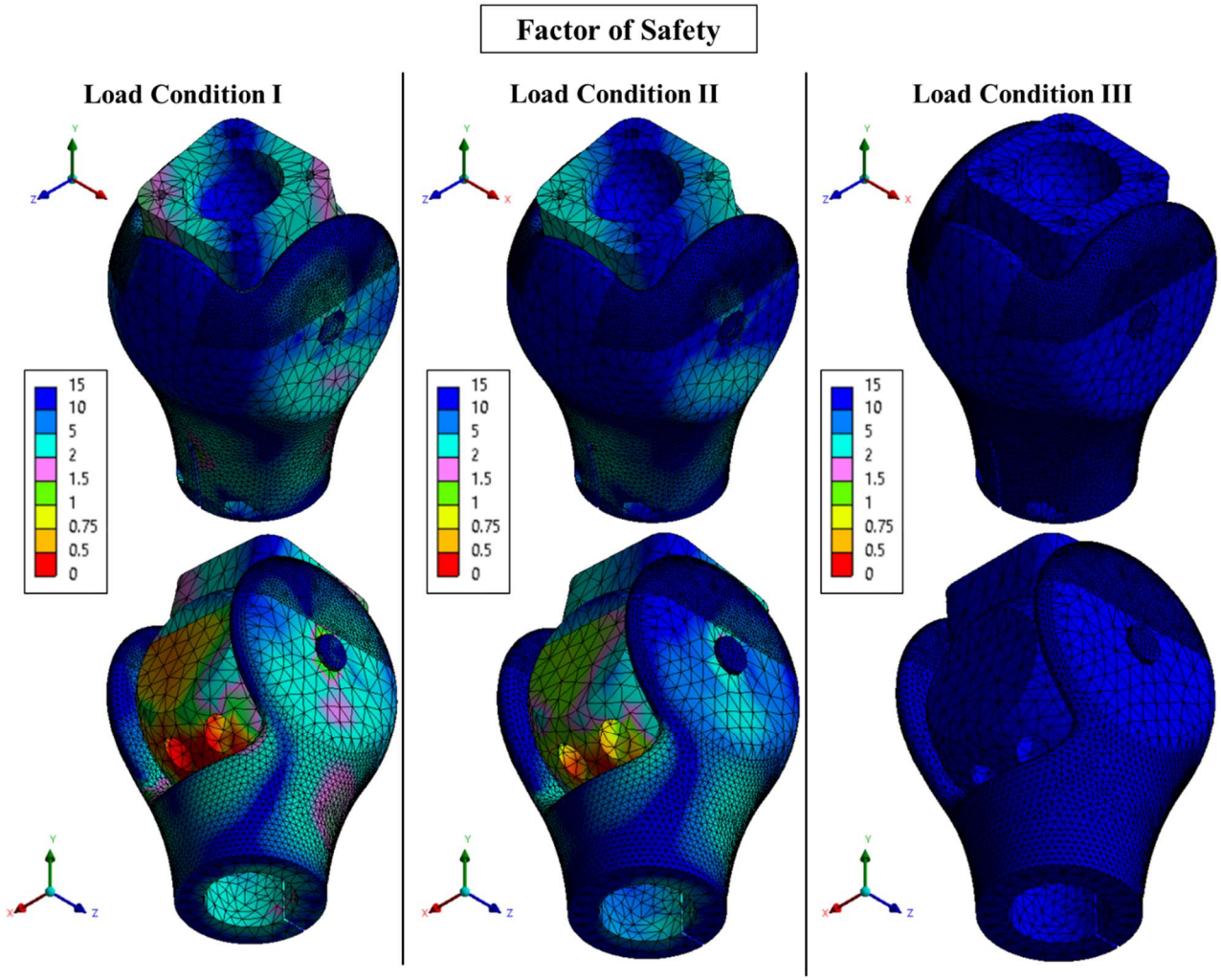

Figure 4-38. Simulation Factor of Safety plot.

4.4 Additive Manufacturing

All 3D printed parts were manufactured with identical settings, respective to material, listed in Table 4-1. Two different shell orientations were tested during experimental validation discussed in Section 4.5. Figure 4-39 displays the preliminary orientation tested utilized to validate Round I simulation data (see Section 4.3.2).

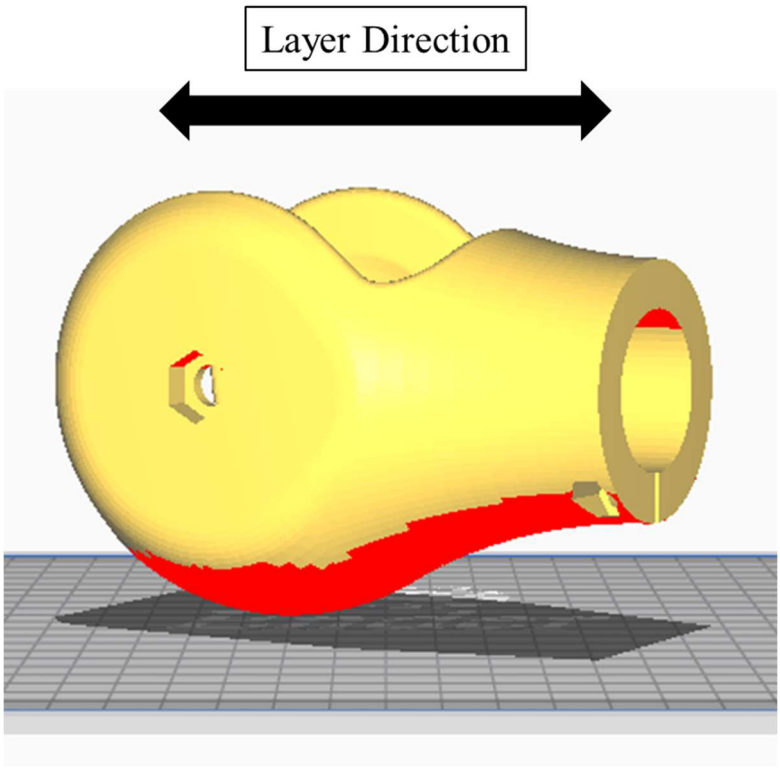

Figure 4-39. Preliminary shell orientation to validate Round I simulation data.

Figure 4-40 displays the final orientation of all 3D printed parts used to validate Round II simulation data (see Section 4.3.2). The final orientations place the part layers in tension for load condition I and load condition II. The pyramid adapter and lattice region are oriented so that the layers are parallel to the bolt connections.

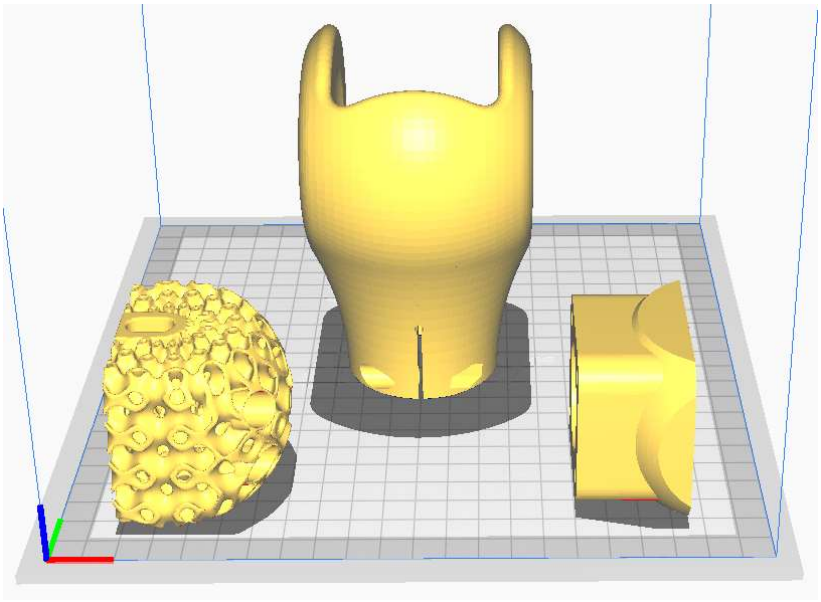

Figure 4-40. Orientation of PKJ components shown within Cura slicer software.

4.5 Experimental Validation

Experimental testing occurred to validate lattice characterization and PKJ assembly simulation results respectively from Section 4.3.1 and Section 4.3.2. A UTM with a 20 kN load cell was utilized for compression tests. Experimental validation did not test every load condition or every characterized lattice. This was due to resulting lack of resources, specifically 3D printing filament, from this project being self-funded. For each experiment, two samples were produced for testing.

4.5.1 Lattice Region

Test Definition

3D printed lattice regions of LRD 30%, LRD 52%, and LRD 69% were experimentally subjected to 2000 N of compressive load to quantify the relationship between LRD and stiffness characterized in Section 4.3.1. The LRD ranges tested represent the minimum, middle, and maximum LRD values characterized from Table 4-4.

Two 3D printed lattice regions were fabricated for each LRD tested. Samples were placed flat against the test machine work surface with load applied as shown in Figure 4-41.

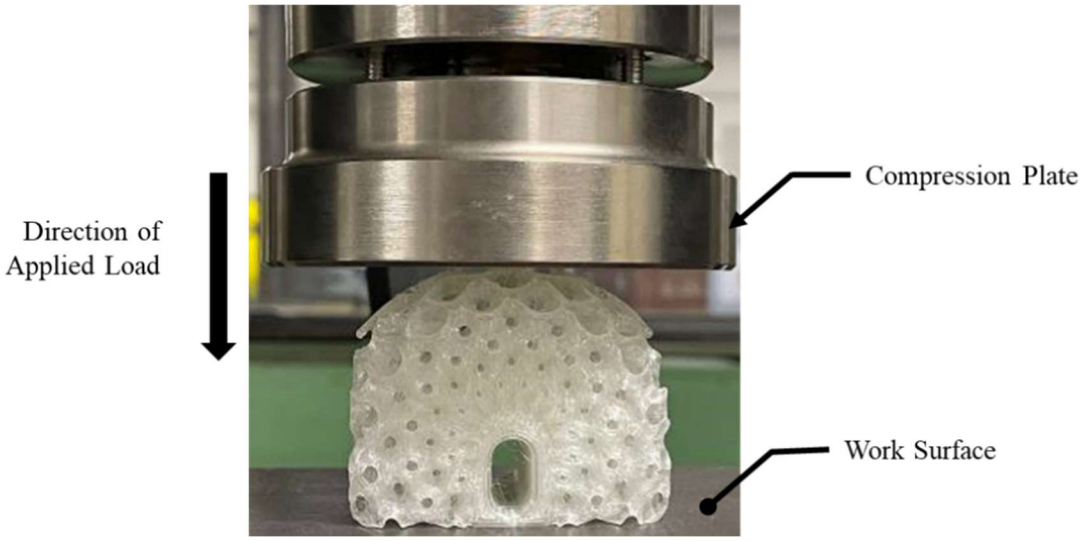

Figure 4-41. Experimental boundary conditions for lattice characterization.

Results

Experimental data displayed positive correlation between stiffness and LRD. Figure 4-42 below validates simulation data in Figure 4-26 displaying that as LRD increases the structure's stiffness decreases. The stiffness in Figure 4-42 is the slope of each line. For a force of 1000 N, the structures with LRD 30% displaced 2.7mm while structures with LRD 69% displaced 6.3mm.

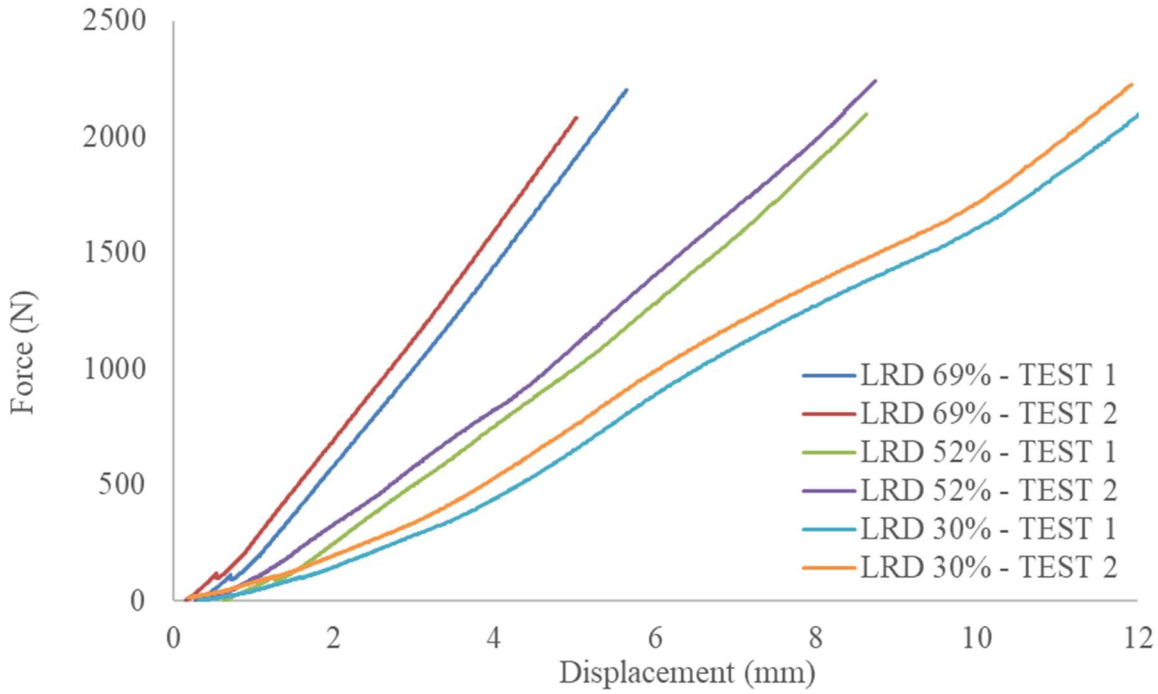

Figure 4-42. Experimental lattice characterization force-displacement plots.

Trendlines (not shown) from Figure 4-42 were used to extract the slope of each line and obtain the stiffness for each test. The stiffnesses are compared against simulation values in Table 4-5.

Table 4-5. Comparison of Experimental and Simulation Lattice Structure Stiffness

LRD	**Stiffness (N/mm)**		
	Test 1	Test 2	Simulation
30%	173	182	113
52%	260	261	284
69%	422	437	517

Figure 4-43 through Figure 4-45 respectively display calculated trendlines from Figure 4-42 for LRD 30%, LRD 52%, and LRD 69%. Experimental trendlines for each LRD value are compared against the predicted simulation data from Figure 4-27. For all LRD values, both experimental test results and simulation predictions display that the lattice structure responds linearly to applied force. Figure 4-43 through Figure 4-45 validates the linear stiffness equation used for lattice characterization in Section 4.3.1.3 (see Equation 2).

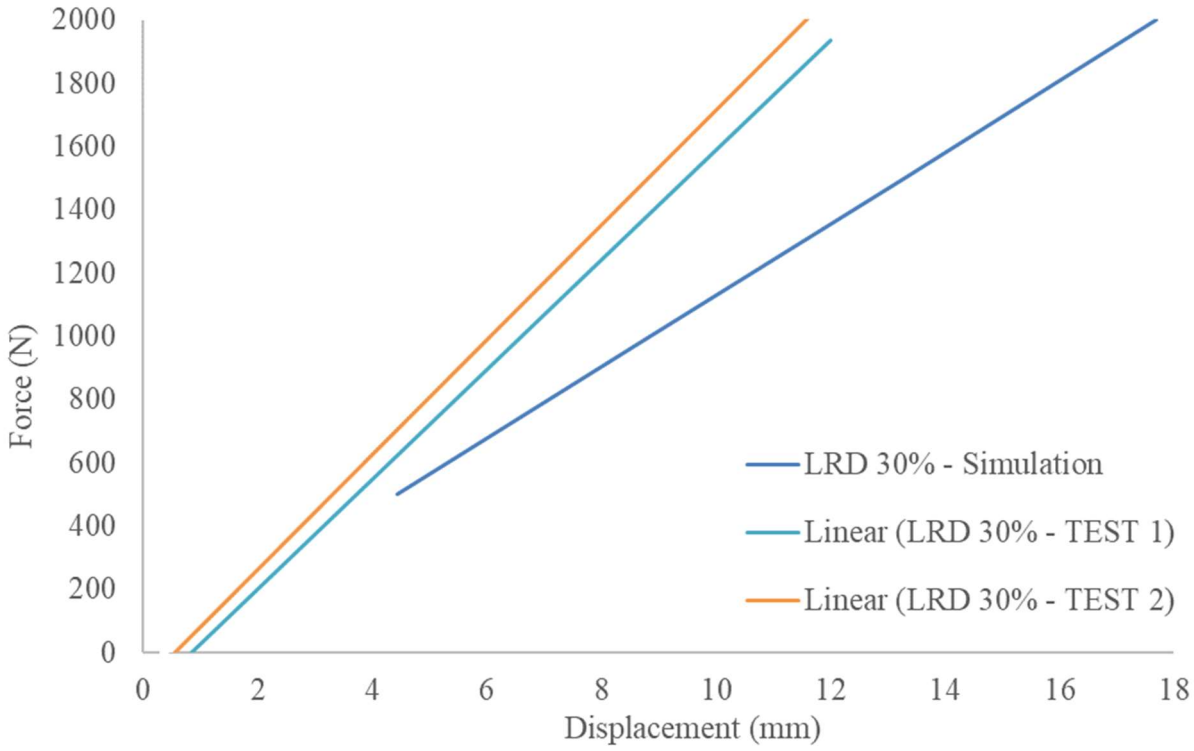

Figure 4-43. LRD 30% force-displacement plots obtained by simulation and experimental results.

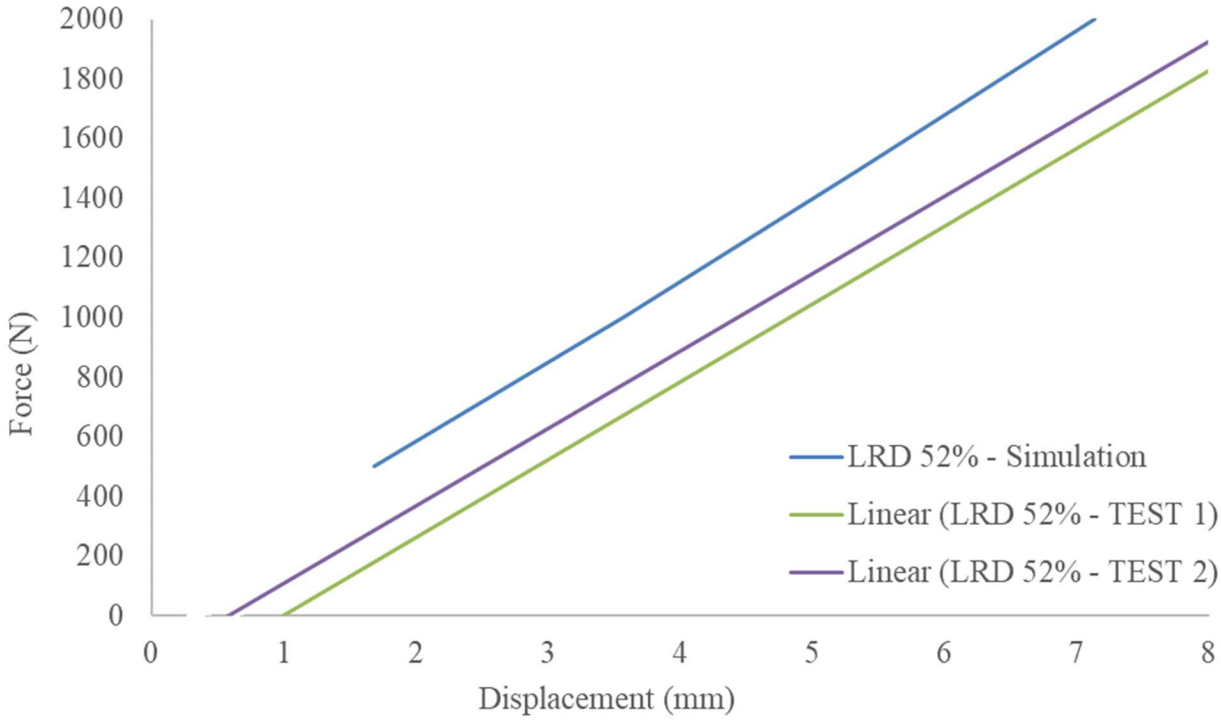

Figure 4-44. LRD 52% force-displacement plots obtained by simulation and experimental results.

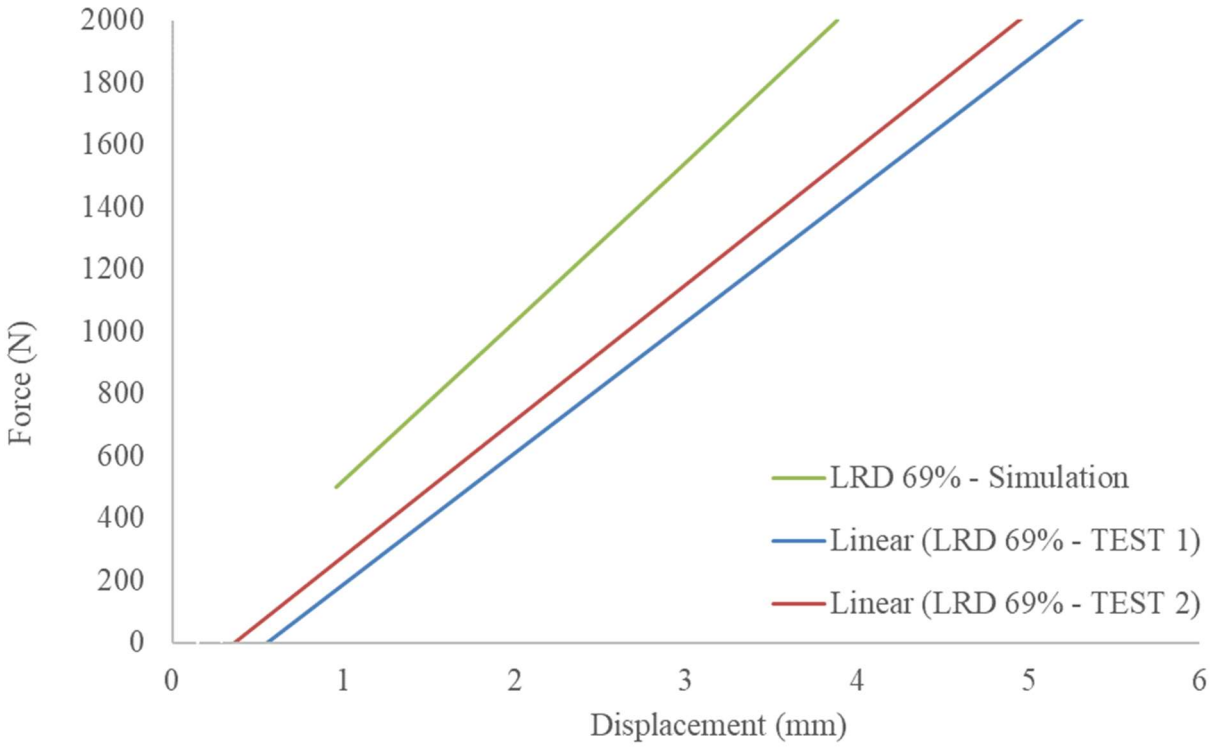

Figure 4-45. LRD 69% force-displacement plots obtained by simulation and experimental results.

Figure 4-46 displays that for both experimental and simulated stiffness values, an exponential relationship can be fit to model the increasing stiffness in relation to increasing LRD. It is

recommended that further research evaluates additional LRD values to evaluate the simulation's exponential trendline.

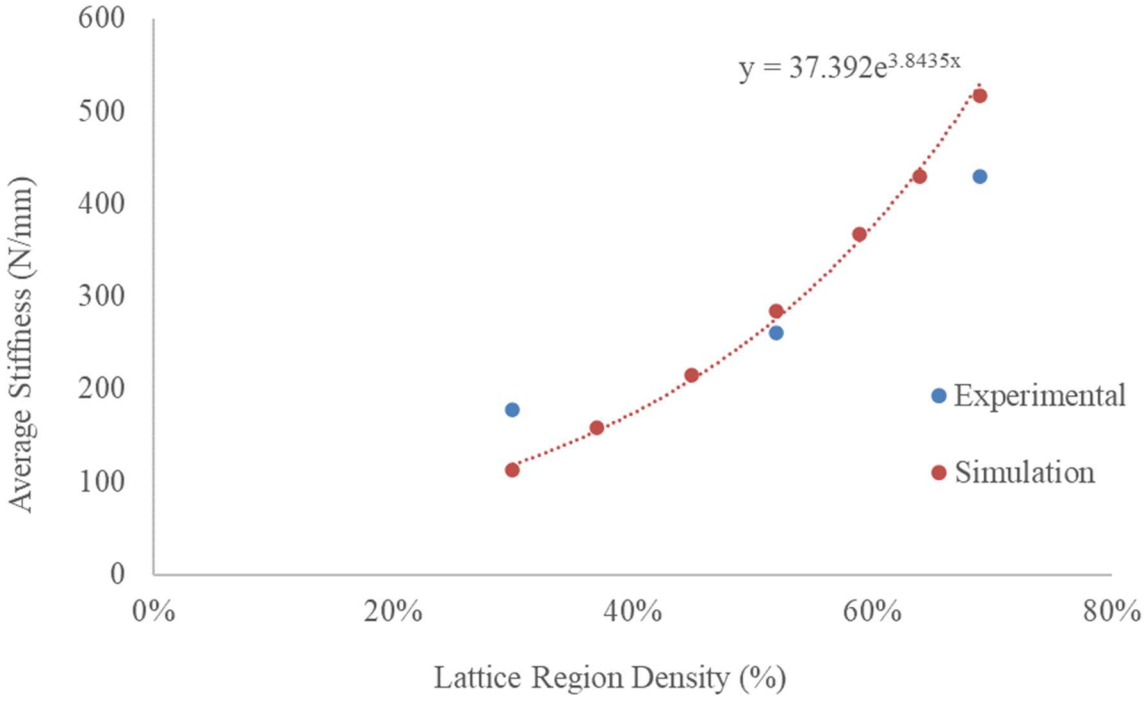

Figure 4-46. Average Stiffness – LRD plot for simulated and experimental data.

4.5.2 PKJ Assembly – Load Condition I

Test Definition

The PKJ assembly was experimentally tested for load condition I. A compressive load of 980 N was applied to the top surface of the pyramid interface with the bottom surface of the shell constrained vertically by the UTM worksurface to prevent the creation of bending forces (see Figure 4-47). No translation along the worksurface was observed during testing.

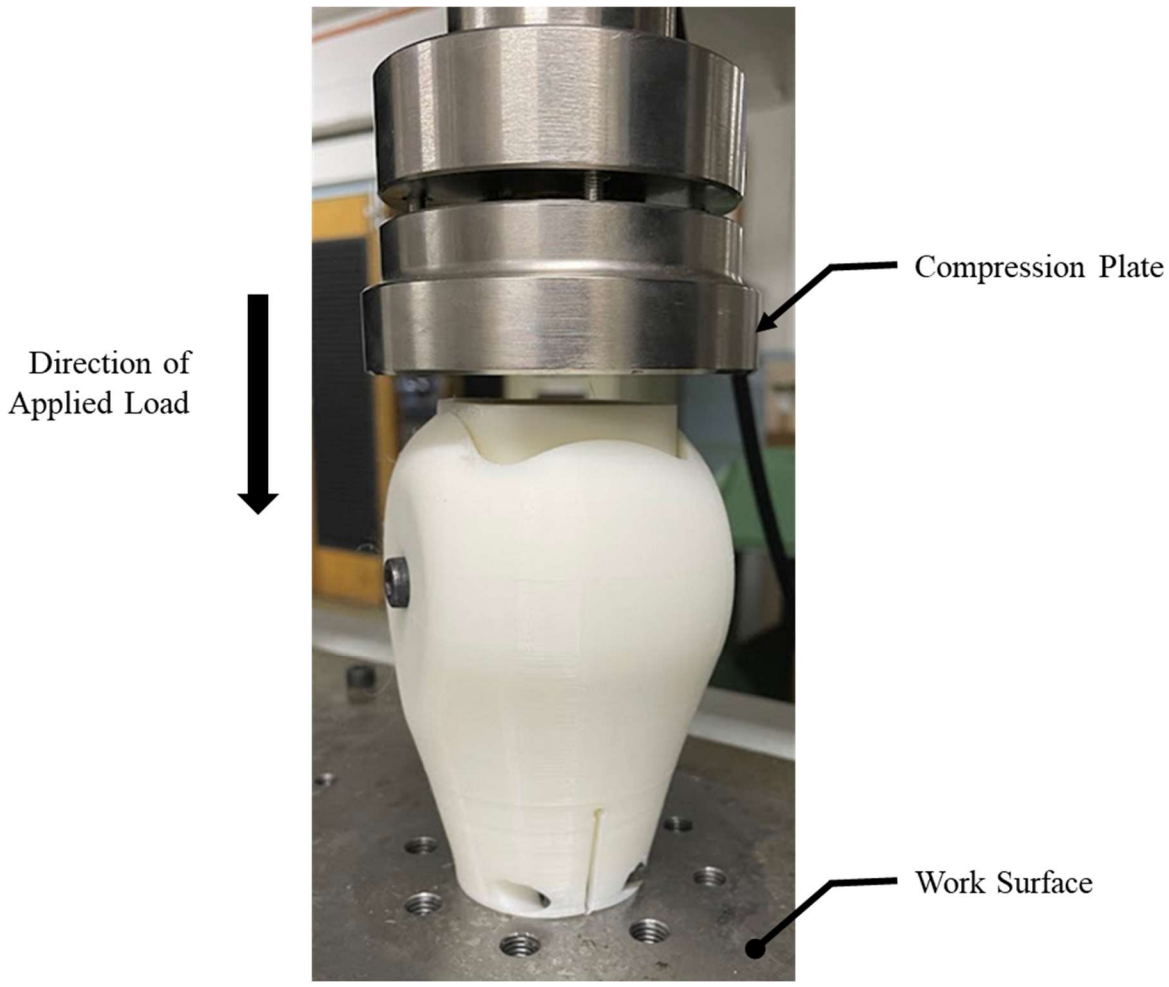

Figure 4-47. Experimental boundary conditions for load condition III.

Results

The PKJ assembly withstood load condition I. The obtained stress-strain plot shown in Figure 4-48 displays a constant slope of stress vs strain indicating no yielding of material and no part failure. No audible sounds of layer delamination were observed during testing and visual inspection indicates no forms of failure. The results identify that while the 3D printed part layers are oriented specifically for load condition I (see Figure 4-49), the layers will withstand the compressive loads from a user standing at rest.

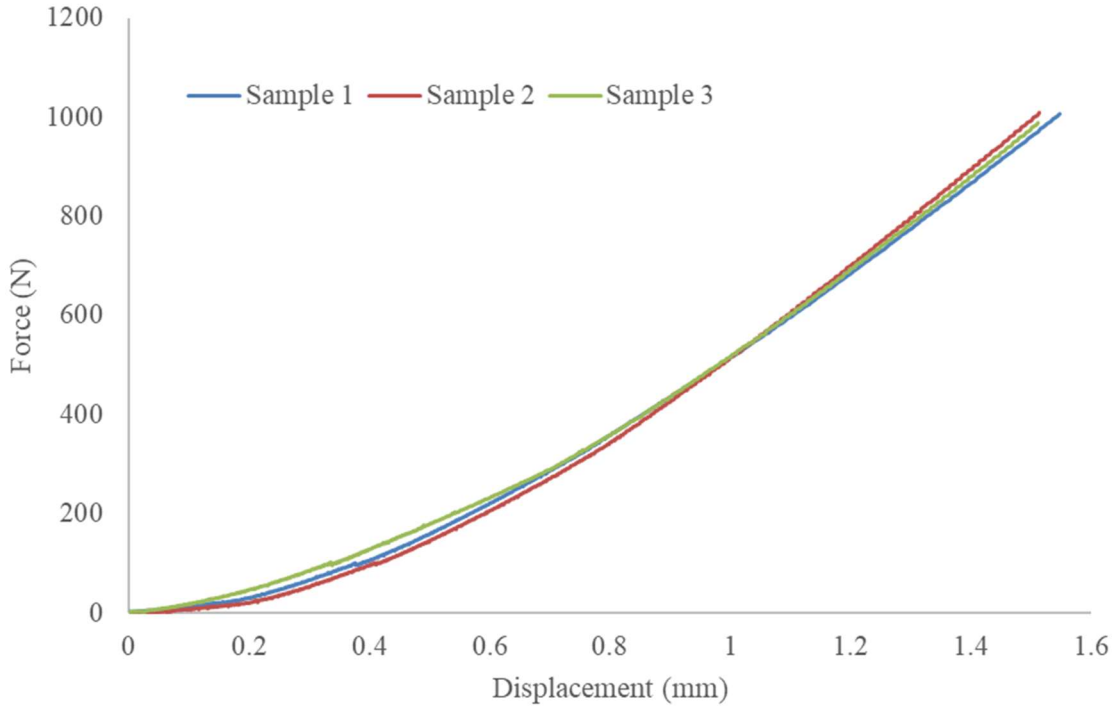

Figure 4-48. Force-Displacement plot for load condition I obtained by experimental testing.

Figure 4-49. PKJ assembly after load condition I.

4.5.3 PKJ Assembly – Load Condition III

Test Definition

Two rounds of experimental testing were performed on the PKJ assembly for load condition I. Round I was performed to validate test results from Section 4.3.2 and ensured accurate redesign of the shell to meet strength requirements. Round II simulated the final, redesigned shell to display compliance with load requirements defined in Section 2.4.10.

A test fixture was fabricated to create remote boundary conditions for load condition I and defined in by ISO 10328:2016 in Section 2.4.10 (see Figure 4-50). Figure 4-51 displays the experimental test set up for load condition I.

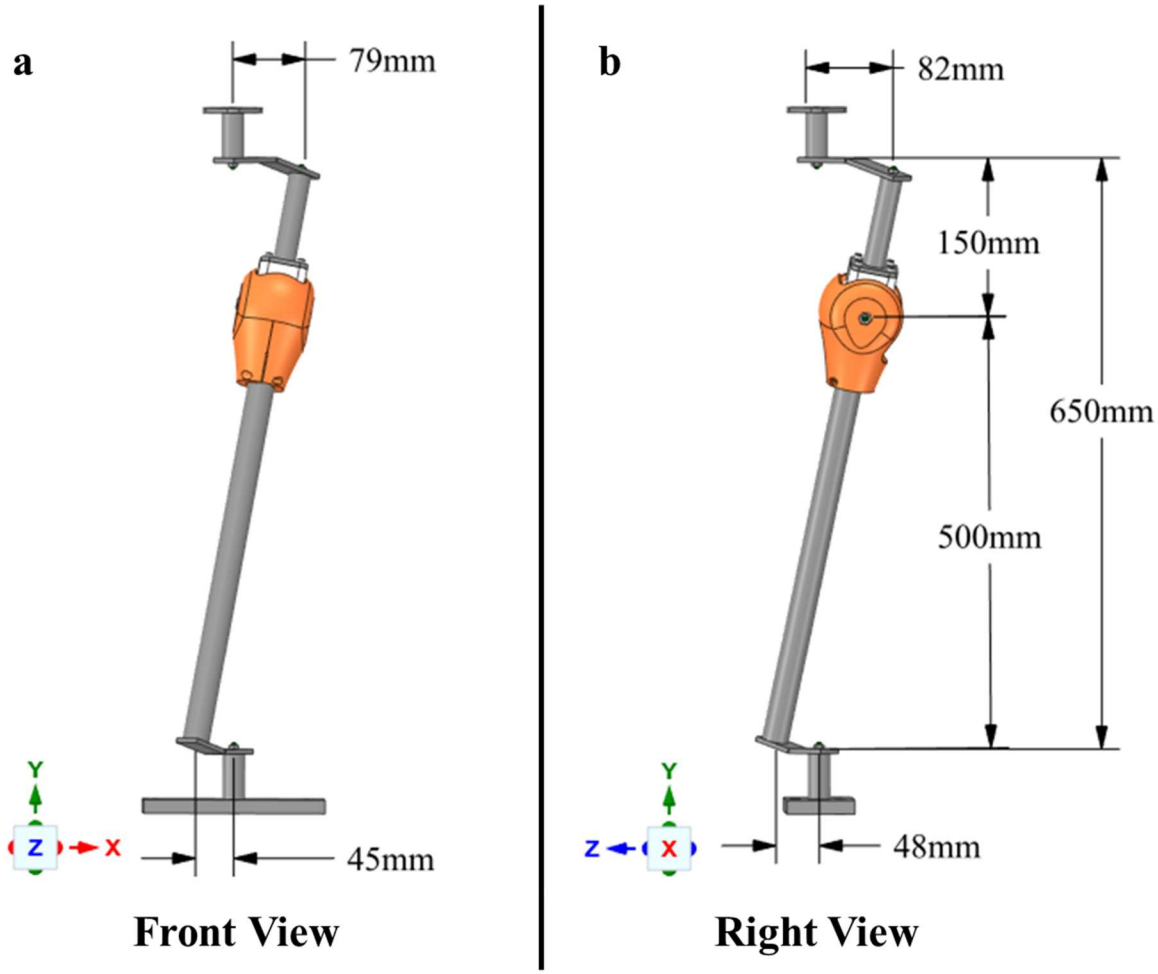

Figure 4-50. CAD model of offset test fixture. (a) Front view. (b) Right view.

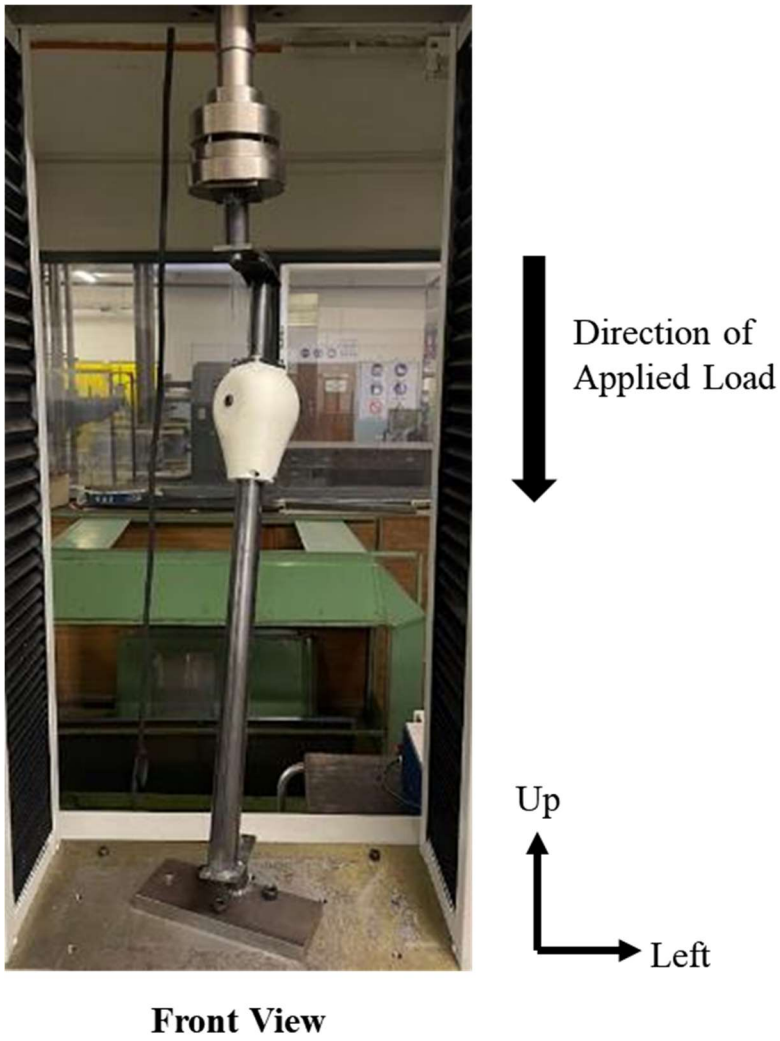

Figure 4-51. Experimental test fixture for load condition III.

Results – Round I

The initial shell design failed at approximately 700 N. Experimental results aligned with simulation data from Section 4.3.2 with failure occurring at the forward right corner. Crack propagation along the layers validated the resulting force direction from the pyramid adapter to the shell (-X +Z direction). Figure 4-52 below compares simulation results next to experimental results. Redesign of the shell is discussed in Section 4.3.2 and reorientation of the shell during 3D printing is discussed in Section 4.4.

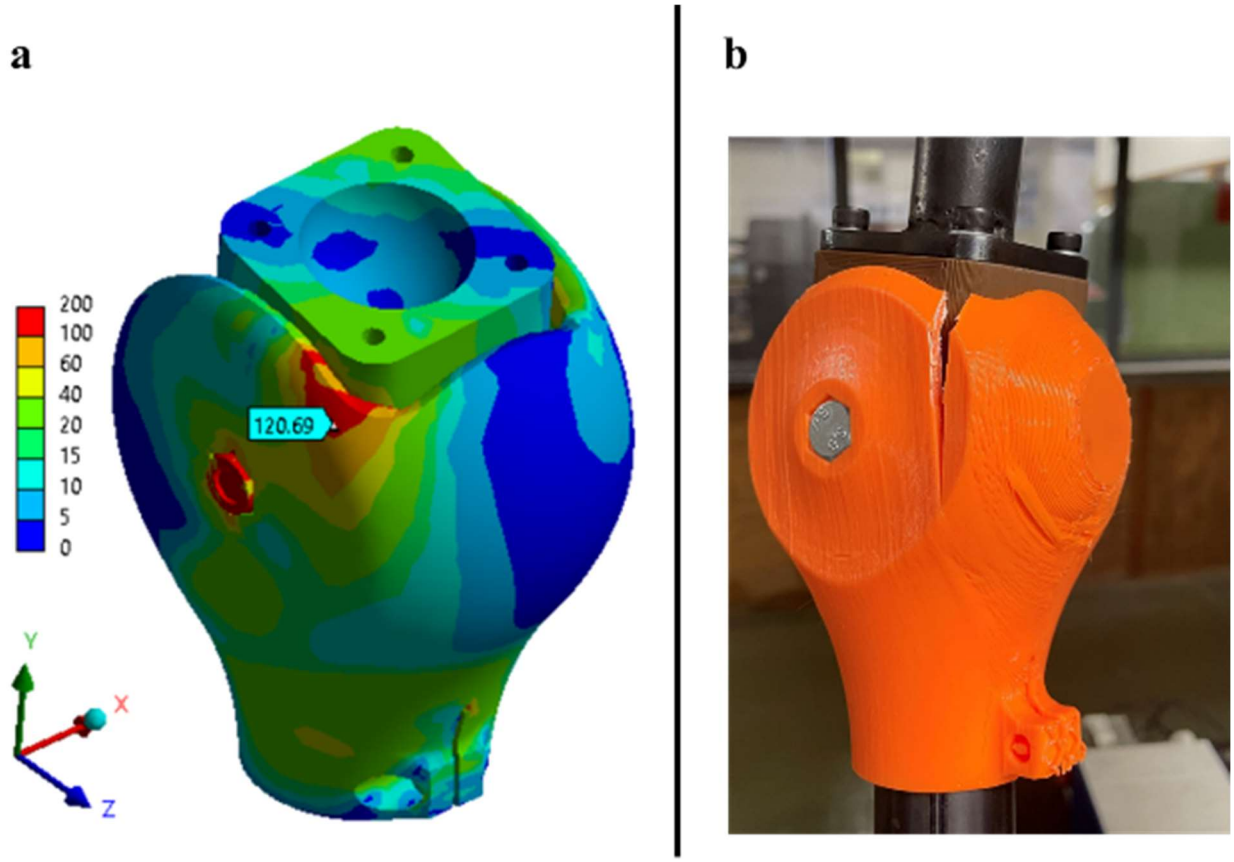

Figure 4-52 (a) Round I simulation results from Section 4.3.2 (b) Round I experimental results.

Results – Round II

During Round II of testing the redesigned PKJ assembly failed at approximately 760 N (see Figure 4-53) due to bolt shear tear-out as shown in Figure 4-54. As the remote offsets loaded the bolts in tension, the combination of threading the bolts directly into the ductile PLA material and the small bolt threads resulted in structural failure. Experimental testing was stopped early before the minimum load requirement of 3360 N was met for load condition I.

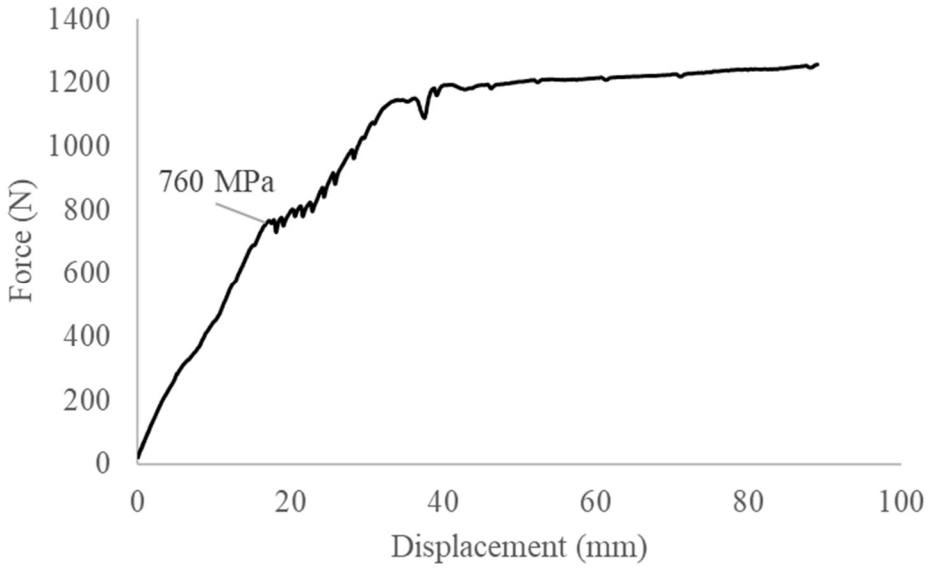

Figure 4-53. Force-displacement plot indicating bolt shear tear-out at 760N.

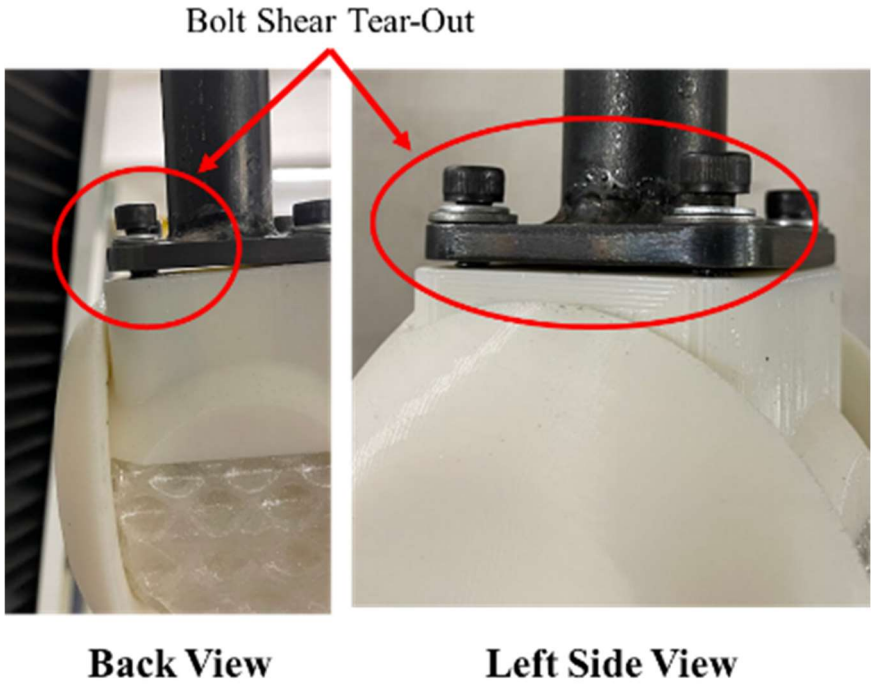

Figure 4-54. Bolt shear tear-out observed for left side of pyramid interface.

Further work is recommended to research methods of eliminating bolt shear tear-out. Specifically, it is recommended to investigate the tear-out strength of embedded nuts, helicoils, and threaded inserts. The ReMotion knee shown in Figure 2-15 circumvents bolts by integrating the metal pyramid adapter directly into the plastic, however, this would increase the complexity, manufacturing, and cost of the PKJ designed in this research project.

4.6 Cost Analysis

The designed PKJ costs R372 per unit (equivalent to $25). Figure 4-55 provides weight and print time details for each part used for the cost analysis.

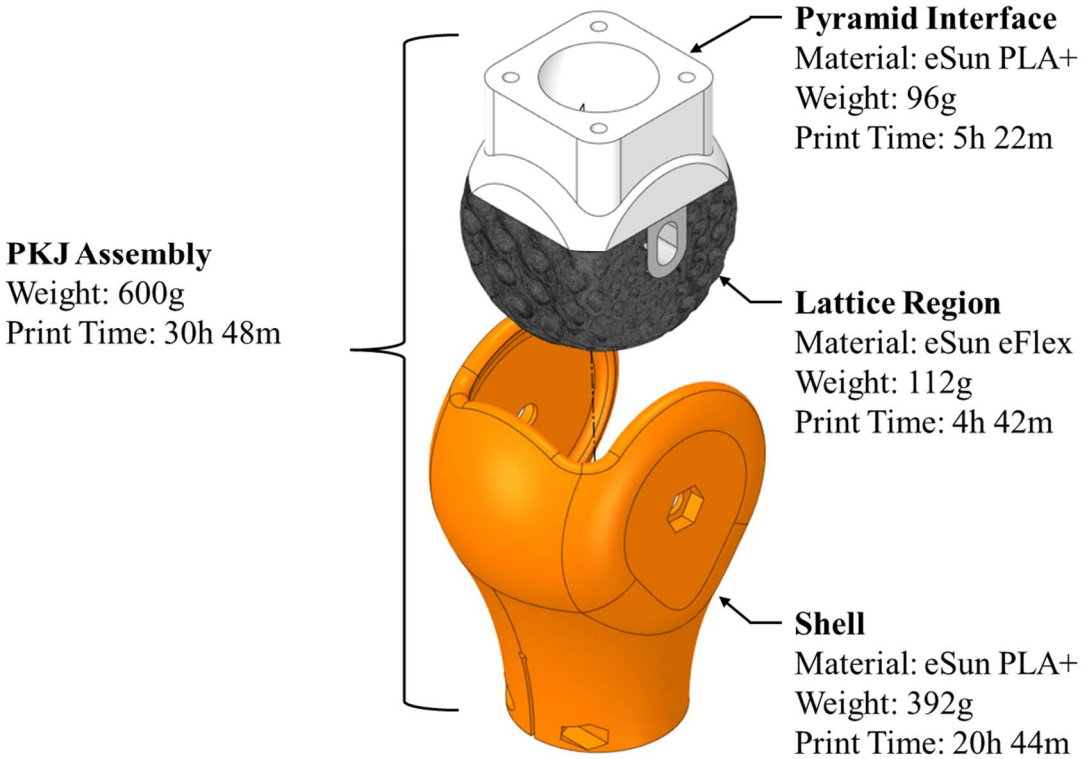

Figure 4-55. Weights and print times of 3D printed components.

The part unit cost includes of the 3D printed PKJ is the sum of material cost, labor cost, and operation cost [69]:

$$Part\ Unit\ Cost = Material\ Cost + Labor\ Cost + Operation\ Cost \quad (3)$$

Table 4-6. Part Unit Cost Analysis

Material	R271.92
Labor	R32.40
Operation	R43.12
Part Cost	**R347.44**

The material cost is the product of the weight of the part times the cost of filament per gram:

$$Material\ Cost = Unit\ Price\ (R/g) * \text{Part Weight (g)} \quad (4)$$

Table 4-7. Material Cost Analysis

Part	Material	Unit Price (R/g)	Weight (g)	Material Cost (R)
Shell	eSun PLA+	0.47	392.00	184.24
Pyramid Interface	eSun PLA+	0.47	96.00	45.12
Lattice Region	eSun eFlex	0.38	112.00	42.56
			Total	**271.92**

The labor cost is the product of hourly wage and time spent setting up and post processing the print. Set up time includes loading the part into 3D printing software, slicing the part, and sending the file to the 3D printer. Post processing includes removal of support material from the completed part. Support material was not present for the designed PKJ. Labor wages for commercial additive manufacturing companies are not disclosed within South Africa and therefore the hourly wage was calculated from United States federal minimum wage of $7.25 [70] equivalent to R108. The minimum wage in South Africa is actually R20 (equivalent to $1.34) [71] resulting in the United States minimum wage representing a max labor cost estimate.

$$Labor\ Cost = Hourly\ Wage * (Set\ Up\ Time + Post\ Processing\ Time) \quad (5)$$

Table 4-8. Labor Cost Analysis

Part	Hourly Wage (R/h)	Slicer Set up Time (m)	Post Processing Time (m)	Labor Cost (R)
Shell	108.00	5.00	1.00	10.80
Pyramid Interface	108.00	5.00	1.00	10.80
Lattice Region	108.00	5.00	1.00	10.80
			Total	**32.40**

The operation cost is calculated as the product of the local cost of one kWh of electricity [72] times the time required for the printer to run to produce the part:

$$Operation\ Cost = Electricity\ Cost * (Print\ Time) \quad (6)$$

Table 4-9. Operation Cost Analysis

Part	Electricity Cost (R / kWh)	Print Time (h)	Operation Cost (R)
Shell	1.40	20.73	29.02
Pyramid Interface	1.40	5.37	7.52
Lattice Region	1.40	4.70	6.58
		Total	**43.12**

The total cost of producing the 3D printed PKJ in developing countries is the one-time purchase cost of a 3D printer plus the cost for the number of units produced.

$$Total\ Cost = Printer\ Price + (Part\ Unit\ Cost * Number\ of\ Units) \quad (7)$$

This research project was performed with an Ender 3 printer with an upgraded direct drive extruder requiring a total cost of R4176 (equivalent to $280). As stated previously in Section 1.4, 3D printing requires a one-time purchase cost for the printer and all further costs are driven by the part's geometry impacting labor, material, and print time. Material is not wasted as 3D printing is an additive process and the printer does not require the operator's presence once started. The designed PKJ's unit cost does not change based on the number of units produced for 3D printing as modifications do not require specialized tooling or fixtures required for injection molding (for detailed comparison between 3D printing and injection molding costs, see Section 1.4 and Figure 1-7). The fixed unit cost provides motivation to produce small batches of customized devices defined by each user. A comparison between injection molding and 3D printing production times for each unit is insignificant and is omitted from analysis as the draw of 3D printed prosthetics is to create low-volume, bespoke devices. The demand for each device is assumed to not meet levels of mass production.

5. CONCLUSION

This research project investigated the redesign of a single-axis PKJ specifically for FFF desktop 3D printing. Furthermore, the feasibility of implementing a compressible FFF lattice structure into the PKJ was studied. Literature review of available prosthetics resulted significant low-cost advances for hands, arms, and feet through the aid of 3D printing. However, minimal research has been conducted to bring forth a 3D printed PKJ which would allow for decentralized, low-overhead, and low-cost manufacturing in developing countries.

The PKJ was designed specifically for expected loads from a 100 kg user highlighting 3D printing's ability to create bespoke products. Modelling was completed through CAD software allowing for motion analysis between components as they rotated around a single axis. The PKJ contains a range of motion from 10 degrees extension to 120 degrees flexion like the human knee and consists of a standard 4-hole pattern and 30mm tube clamp to interface with commercial prosthetic components. The design has a bounding box of 72mm x 90mm x 13mm and weighs 600 g.

A deformable lattice structure, successfully printed by FFF 3D printing, was identified, and modeled through nTopology software. The structure allows for user defined parameter selection which alters the stiffness of the structure. A predictive model of the structure's stiffness was characterized for various lattice structure densities through simulation and experimentally validated through testing.

Static strength simulations were performed on the PKJ structure against ultimate load requirements set by ISO 10328:2016 Preliminary simulation results were validated by experimental testing with demonstrating points of high stress and failure identified in simulation as points of part failure during testing. Simulation on the final PKJ design indicated no part failure as the ultimate load case resulted a FOS of at least 1.5.

Experimental testing resulted in the PKJ withstanding compressive loads representing the weight of the user standing at rest, however, the PKJ failed to meet ultimate strength requirements defined by ISO 10328:2016. Due to offset remote loading, failure by bolt shear tear-out occurred at PLA connections. This failure was not identified in simulation as analysis of bolted connections were omitted and remote forces were scoped to surfaces only. Experimental testing indicates that the entire PKJ assembly cannot be 3D printed and requires a more structural interface for bolted connections.

The concept of a 3D printed PKJ remains effective as it financially allows for bespoke customization defined by the end user's weight and performance requirements. The designed PKJ costs a total of R372 per unit (equivalent to $25) and the price is not dependent on the number of units produced.

Further Research Recommendations

The following recommendations are provided to continuate the goal of creating low-cost 3D printed PKJs for developing countries are as follow:

1. Investigation of embedded threaded inserts and embedded nuts which have demonstrated means to provide structural interface between 3D printed parts and bolts. However, research has identified marginal improvement of shear-out strength [73].
2. Gait analysis should occur to ensure proper placement of the single axis of rotation. Studies should utilize both simulation and involve case studies with amputees.
3. Case studies involving amputees should be performed to identify the perceived level of comfort created by deformable lattice structures of varying densities.
4. Light weighting of the shell should be performed. Studies have indicated that solid 3D printed parts (infill 100%) is not optimal as the structure's strength is developed in its walls [74]. Significant cuts can be made to the shell's weight, printing time, and printing material through infill studies.

6. ETHICAL ISSUES/CLEARANCE

This research project has been ratified by WITS University Main Ethics Committee (non-medical). The clearance number is MIAEC 024/21W.

7. REFERENCES

1. Organization WH. Guidelines for training personnel in developing countries for prosthetics and orthotics services [Internet]. World Health Organization; 2005 [cited 2021 Mar 17]. Available from: https://apps.who.int/iris/handle/10665/43127
2. Issue [Internet]. [cited 2021 Mar 17]. Available from: http://universalprosthetics.com/issue.html
3. | Human Development Reports [Internet]. [cited 2021 Mar 17]. Available from: http://hdr.undp.org/en/2020-report
4. Osseointegration for Amputees: Current Implants, Techniques,... : JBJS Reviews [Internet]. [cited 2021 Mar 17]. Available from: https://journals.lww.com/jbjsreviews/Fulltext/2020/03000/Osseointegration_for_Amputees__Current_Implants,.9.aspx
5. The rehabilitation of the amputee in the developing world: a review of the literature | O&P Virtual Library [Internet]. [cited 2021 Mar 17]. Available from: http://www.oandplibrary.org/poi/1996_01_045.asp
6. Hui A. Quick Guide to Prosthetic Limbs in Canada - Cost, Types, and Funding [Internet]. [cited 2021 Mar 17]. Available from: https://www.olympiabenefits.com/blog/quick-guide-to-prosthetic-limbs-in-canada-cost-types-and-funding
7. Rohwerder B. Disability Stigma in Developing Countries. 2018 May 9 [cited 2021 Mar 17]; Available from: https://opendocs.ids.ac.uk/opendocs/handle/20.500.12413/13795
8. Stigma as barrier to the implementation of the Convention on the Rights of Persons with Disabilities in Africa [2016] ADRY 2 [Internet]. [cited 2021 Mar 17]. Available from: http://www.saflii.org/za/journals/ADRY/2016/2.html
9. Njelesani J, Hashemi G, Cameron C, Cameron D, Richard D, Parnes P. From the day they are born: a qualitative study exploring violence against children with disabilities in West Africa. BMC Public Health. 2018 Dec;18(1):153.
10. Monocentric (single axis) knees [Internet]. [cited 2021 Mar 24]. Available from: https://www.nzals.co.nz/products/categories/knee-joints/monocentric-single-axis-knees
11. Donaldson K. The $80 prosthetic knee that's changing lives [Internet]. [cited 2021 Mar 17]. Available from: https://www.ted.com/talks/krista_donaldson_the_80_prosthetic_knee_that_s_changing_lives
12. Williams W. Bionic Leg Price List [Internet]. 2020 [cited 2021 Mar 25]. Available from: https://bionicsforeveryone.com/bionic-leg-price-list/
13. Scott Yu-Jan. Krista Donaldson: The $80 prosthetic knee that's changing lives [Internet]. 2013 [cited 2021 Mar 24]. Available from: https://www.youtube.com/watch?v=LIy2oVJtJsA&t=205s
14. Clinical field testing of trans-femoral prosthetic technologies: Resin-wood and ICRC-polypropylene - J. S. Jensen, W. Raab, 2004 [Internet]. [cited 2021 Mar 21]. Available from: https://journals.sagepub.com/doi/10.1080/03093640408726699?url_ver=Z39.88-2003&rfr_id=ori:rid:crossref.org&rfr_dat=cr_pub%20%200pubmed
15. What is Additive Manufacturing? | GE Additive [Internet]. [cited 2021 Mar 17]. Available from: https://www.ge.com/additive/additive-manufacturing
16. Top 3D printing technologies 2021 [Internet]. Statista. [cited 2022 Jan 18]. Available from: https://www.statista.com/statistics/560304/worldwide-survey-3d-printing-top-technologies/
17. Burkhardt F, Schirmeister CG, Wesemann C, Nutini M, Pieralli S, Licht EH, et al. Pandemic-Driven Development of a Medical-Grade, Economic and Decentralized Applicable Polyolefin Filament for Additive Fused Filament Fabrication. Molecules. 2020 Jan;25(24):5929.
18. 11 Things to Consider When Choosing Your First or Next Desktop 3D Printer [Internet]. [cited 2021 Mar 25]. Available from: http://my3dconcepts.com/explore/main-components-of-desktop-3d-printers/

19. 3-D Printer Brings Dexterity To Children With No Fingers : Shots - Health News : NPR [Internet]. [cited 2021 Mar 17]. Available from: https://www.npr.org/sections/health-shots/2013/06/18/191279201/3-d-printer-brings-dexterity-to-children-with-no-fingers
20. Industries M. MakerBot and Robohand [Internet]. GlobeNewswire News Room. 2013 [cited 2021 Mar 17]. Available from: http://www.globenewswire.com/news-release/2013/05/08/545632/10031955/en/MakerBot-and-Robohand.html
21. Manero A, Smith P, Sparkman J, Dombrowski M, Courbin D, Kester A, et al. Implementation of 3D Printing Technology in the Field of Prosthetics: Past, Present, and Future. Int J Environ Res Public Health [Internet]. 2019 May [cited 2021 Mar 17];16(9). Available from: https://www.ncbi.nlm.nih.gov/pmc/articles/PMC6540178/
22. The Raptor Reloaded [Internet]. Enabling The Future. 2015 [cited 2021 Mar 21]. Available from: http://enablingthefuture.org/upper-limb-prosthetics/raptor-reloaded/
23. Developing 3D printed Prosthetics for Animals with nTop Platform | nTopology [Internet]. [cited 2021 Mar 17]. Available from: https://ntopology.com/blog/2020/11/12/3d-printed-prosthetics-for-animals/
24. Carbon 3D Print Lattice Innovation — The adidas Story [Internet]. Carbon. 2018 [cited 2021 Mar 17]. Available from: https://www.carbon3d.com/resources/whitepaper/the-adidas-story/
25. Franchetti M, Kress C. An economic analysis comparing the cost feasibility of replacing injection molding processes with emerging additive manufacturing techniques. Int J Adv Manuf Technol. 2017 Feb 1;88(9):2573–9.
26. Robohand Featured On NPR [Internet]. MakerBot. 2013 [cited 2021 Mar 21]. Available from: https://www.makerbot.com/stories/medical/robohand-featured-on-npr/
27. Savonen BL. A METHODOLOGY FOR TRIAGING PRODUCT NEEDS FOR LOCALIZED MANUFACTURING WITH 3D PRINTING IN LOW-RESOURCE ENVIRONMENTS. 2019 Apr 16 [cited 2021 Mar 19]; Available from: https://etda.libraries.psu.edu/catalog/17016bls78
28. Griffiths SD Daniel O'Connor, Laura. The latest 3D printing efforts against Covid-19 [Internet]. TCT Magazine. 2020 [cited 2021 Mar 19]. Available from: https://www.tctmagazine.com/api/content/ce4b81e6-6cf7-11ea-ac07-1244d5f7c7c6/
29. ABOUT US [Internet]. Enabling The Future. 2014 [cited 2021 Mar 17]. Available from: http://enablingthefuture.org/about/
30. Fu H, Zhang X, Wang X, Yang R, Li J, Wang L, et al. A novel prosthetic knee joint with a parallel spring and damping mechanism. Int J Adv Robot Syst. 2016 Aug 1;13(4):1729881416658174.
31. Thingiverse.com. Search Thingiverse - Thingiverse [Internet]. [cited 2021 Mar 17]. Available from: https://www.thingiverse.com/search?q=prosthetic+hand&type=things&sort=relevant
32. How is a lattice structure used in additive manufacturing? | Fast Radius [Internet]. [cited 2021 Mar 31]. Available from: https://www.fastradius.com/resources/understanding-3d-printed-lattices-performance-and-design-considerations/
33. Yan L, Zhu K, Zhang Y, Zhang C, Zheng X. Effect of Absorbent Foam Filling on Mechanical Behaviors of 3D-Printed Honeycombs. Polymers. 2020 Sep;12(9):2059.
34. (PDF) The anisotropic elastic behavior of the widely-used triply-periodic minimal surface based scaffolds [Internet]. [cited 2021 Sep 6]. Available from: https://www.researchgate.net/publication/334567288_The_anisotropic_elastic_behavior_of_the_widely-used_triply-periodic_minimal_surface_based_scaffolds/figures?lo=1&utm_source=google&utm_medium=organic
35. 3D Printing Technology Comparison: FDM vs. SLA vs. SLS [Internet]. Formlabs. [cited 2021 Mar 31]. Available from: https://formlabs.com/blog/fdm-vs-sla-vs-sls-how-to-choose-the-right-3d-printing-technology/

36. Guerra Silva R, Torres MJ, Zahr Viñuela J, Zamora AG. Manufacturing and Characterization of 3D Miniature Polymer Lattice Structures Using Fused Filament Fabrication. Polymers. 2021 Jan;13(4):635.
37. overhang.jpg (JPEG Image, 399 × 399 pixels) [Internet]. [cited 2021 Sep 6]. Available from: http://mae3.eng.ucsd.edu/_/rsrc/1472871033179/3d-printing/overhang.jpg?height=399&width=400
38. Kumar A, Verma S, Jeng J-Y. Supportless Lattice Structures for Energy Absorption Fabricated by Fused Deposition Modeling. 3D Print Addit Manuf. 2020 Mar 31;7.
39. Bates SRG, Farrow IR, Trask RS. 3D printed polyurethane honeycombs for repeated tailored energy absorption. Mater Des. 2016 Dec 15;112:172–83.
40. Bates S, Farrow I, Trask R. Compressive behaviour of 3D printed thermoplastic polyurethane honeycombs with graded densities. Mater Des. 2018 Nov 1;162.
41. The difference of PLA and PLA+ tested! (feat. Polymaker) [Internet]. CNC Kitchen. [cited 2021 Sep 7]. Available from: https://www.cnckitchen.com/blog/the-difference-of-pla-and-pla-tested-feat-polymaker
42. PLA vs PLA+/Plus Filament: The Differences [Internet]. All3DP. 2021 [cited 2021 Sep 7]. Available from: https://all3dp.com/2/pla-vs-pla-3d-printer-filament-compared/
43. eSUN 3D New Optimized PLA+ 3D Printing Filament | eSUN 3D Printing Materials [Internet]. [cited 2021 Aug 28]. Available from: https://www.esun3d.net/products/142.html
44. Slapnik J, Bobovnik R, Mešl M, Bolka S. Modified polylactide filaments for 3D printing with improved mechanical properties. Contemp Mater. 2017 Apr 26;VII:142–50.
45. Hamner S, Narayan V, Donaldson K. Designing for Scale: Development of the ReMotion Knee for Global Emerging Markets. Ann Biomed Eng. 2013 Mar 23;41.
46. Cool product: $20 artificial knee for patients in the developing world | Stanford News Release [Internet]. 2009 [cited 2021 Mar 18]. Available from: https://news.stanford.edu/pr/2009/pr-limbs-041509.html
47. ReMotion Knee - Future Health Systems [Internet]. [cited 2021 Mar 21]. Available from: http://cargocollective.com/futurehealth/ReMotion-Knee
48. Design of Mechanism for a Low-cost, Completely Passive Prosthetic Knee for Users with Above-knee Amputation | MIT Technology Licensing Office [Internet]. [cited 2021 Mar 17]. Available from: https://tlo.mit.edu/technologies/design-mechanism-low-cost-completely-passive-prosthetic-knee-users-above-knee
49. ReMotion Knee V3 | Engineering For Change [Internet]. [cited 2021 Sep 6]. Available from: https://www.engineeringforchange.org/solutions/product/remotion-knee/
50. Ramakrishnan T, Schlafly M, Reed K. Evaluation of 3D printed anatomically scalable transfemoral prosthetic knee. 2017 Int Conf Rehabil Robot ICORR. 2017;
51. Prosthetics | Artificial Limbs | Limb Replacement For Amputees [Internet]. [cited 2021 Sep 6]. Available from: https://www.llop.com/prosthetics/
52. 3R67 Knee joint for children [Internet]. [cited 2021 Sep 6]. Available from: https://www.ottobockus.com/products/3r67-knee-joint-for-children/
53. Prosthetic Knee Joints in Prosthetics [Internet]. Advantage Home Medical Equipment. [cited 2021 Sep 6]. Available from: https://shop.advantagehme.org/s/search/products/subcategory/Prosthetic%20Knee%20Joints/category/Prosthetics
54. Socket Adapter - titanium - | Adapters / Structural Components | Lower Limb Prosthetics | Prosthetics | Ottobock US Shop [Internet]. [cited 2021 Sep 6]. Available from: https://shop.ottobock.us/Prosthetics/Lower-Limb-Prosthetics/Adapters-Structural-Components/Socket-Adapter---titanium--/p/4R77
55. IB-ER | PROSTHETICS [Internet]. [cited 2021 Sep 6]. Available from: http://www.ib-er.com/products.html

56. How does part orientation affect a 3D print? [Internet]. Hubs. [cited 2021 Sep 16]. Available from: https://www.hubs.com/knowledge-base/how-does-part-orientation-affect-3d-print/
57. Thingiverse.com. Extrusion Width Testing of 3D Printed Specimens by MechEngineerMike [Internet]. [cited 2021 Sep 16]. Available from: https://www.thingiverse.com/thing:852315
58. The influence of layer height on the strength of FDM 3D prints [Internet]. CNC Kitchen. [cited 2021 Sep 16]. Available from: https://www.cnckitchen.com/blog/the-influence-of-layer-height-on-the-strength-of-fdm-3d-prints
59. Kuznetsov V. Strength of PLA Components Fabricated with Fused Deposition Technology Using a Desktop 3D Printer as a Function of Geometrical Parameters of the Process. Polymers. 2018 Mar 13;10.
60. Orthotropics - INDIVIDUAL DIFFERENCES IN WALKING PATTERNS ---------- ---------- www.orthotropics.co.uk ---------- Ectomorphic, mesomorphic, and endomorphic body types have different types of gait, and there is great variation within these general categories. It is not unusual to recognize a person at a distance strictly by his or her gait. Each of us has a characteristic walking pattern that is altered by both mood and environment. In addition, injury frequently alters normal axes of movement, restricting some and exaggerating others. Thus, any description of gait is a generalization that points out gross similarities of segmental motion. THE GAIT CYCLE The normal gait presents smoothness of function without any sign of impairment or affliction of parts of the body. The normal walking cycle is considered to have two phases: (1) a stance phase, when the foot is in contact with theground; and (2) a swing phase, when the foot is moving forward in the air (Fig. 4.19). During normal walking, one leg is in the stance phase while the other isin the swing phase. Muscles must contract to counterbalance the forces of gravity, to offer acceleration or deceleration to momentum forces, and to overcomethe resistance of the walking surface. The Stance Phase. About 60% of the walking cycle is used in the stance phase. Because the stance phase is the weight-bearing phase requiring the greatest stress, most problems will become apparent in its analysis. The stance phase is subdivided into: (1) heelstrike, (2) footflat, and (3) toe pushoff. Midstance is that weight-bearing period between footflat to toeoff. The duration of gait is usually measured from heelstrike to heelstrike, but any two identical points can be taken. The Swing Phase. This is subdivided into: (1) initial acceleration, (2) mid swing, and (3) final deceleration --depending upon the intent. The swing phase, about 40% of the gait cycle, begins with toeoff and ends with heelstrike. Midswing represents the transition period between acceleration and deceleration. Read more about fundamental orthodontic concepts at Prof John Mew`s new book of “The Cause & Cure of Malocclusion” at: www.lsfo.co.uk/eshop/The_Cause_and_Cure_of_Malocclusion.php Learn more about facial growth, malocclusion and its treatment by joining orthodontic-orthotropic course at: www.lsfo.co.uk/three-day-orthotropics-orthodontics-clinical-and-practice-course ---------- ---------- http://www.chiro.org/ACAPress/Body_Alignment.html ---------- | Facebook [Internet]. [cited 2022 Jan 28]. Available from: https://mbasic.facebook.com/orthotropics/photos/a.438740862823750/762751173756049/?type=3&__tn__=-R
61. Fig. 2 Range of movements (ROM) in the knee flexion and extension, the... [Internet]. ResearchGate. [cited 2021 Sep 21]. Available from: https://www.researchgate.net/figure/Range-of-movements-ROM-in-the-knee-flexion-and-extension-the-positioning-seat-with-the_fig2_268253519
62. Knee Range Of Motion & How To Measure & Improve [Internet]. Knee-Pain-Explained.com. [cited 2021 Sep 21]. Available from: https://www.knee-pain-explained.com/knee-range-of-motion.html
63. 14:00-17:00. ISO 10328:2016 [Internet]. ISO. [cited 2021 Mar 17]. Available from: https://www.iso.org/cms/render/live/en/sites/isoorg/contents/data/standard/07/02/70205.html

64. Shen F, Yuan S, Guo Y, Zhao B, Bai J, Qwamizadeh M, et al. Energy Absorption of Thermoplastic Polyurethane Lattice Structures via 3D Printing: Modeling and Prediction. Int J Appl Mech. 2016 Oct;08(07):1640006.
65. ISO 527-2:2012 Tensile Properties of Plastics; [Internet]. [cited 2021 Sep 12]. Available from: http://www.instron.com/en/testing-solutions/by-standard/iso/iso-527-2
66. What are the limitations of exporting lattice structures to CAD? [Internet]. nTopology. [cited 2021 Sep 17]. Available from: https://support.ntopology.com/hc/en-us/articles/360059299613-What-are-the-limitations-of-exporting-lattice-structures-to-CAD-
67. Download Ansys Student | Workbench-based Simulation Tools [Internet]. [cited 2021 Sep 19]. Available from: https://www.ansys.com/academic/students/ansys-student
68. Sharper Curve, Stronger Egg [Internet]. Inside Science. [cited 2021 Sep 17]. Available from: https://www.insidescience.org/news/sharper-curve-stronger-egg
69. How to calculate 3D printing costs? [Internet]. Prusa Printers. 2020 [cited 2021 Sep 25]. Available from: https://blog.prusaprinters.org/how-to-calculate-printing-costs_38650/
70. Minimum Wage | U.S. Department of Labor [Internet]. [cited 2021 Sep 25]. Available from: https://www.dol.gov/general/topic/wages/minimumwage
71. Minimum wage in South Africa: salaries and wage levels | Expatica [Internet]. [cited 2021 Sep 25]. Available from: https://www.expatica.com/za/working/employment-law/minimum-wage-in-south-africa-982321/
72. NadineL. How Much Does Electricity Cost Per KWh In South Africa 2020? [Internet]. [cited 2021 Oct 3]. Available from: https://jknvenergy.co.za/electricity-cost-per-kwh-south-africa/
73. Helicoils, Threaded Insets and Embedded Nuts in 3D Prints - Strength & Strength Assessment [Internet]. CNC Kitchen. [cited 2021 Sep 25]. Available from: https://www.cnckitchen.com/blog/helicoils-threaded-insets-and-embedded-nuts-in-3d-prints-strength-amp-strength-assessment
74. CNC Kitchen. INFILL pattern and SHELLS - How to get the maximum STRENGTH out of your 3D prints? [Internet]. 2018 [cited 2021 Sep 25]. Available from: https://www.youtube.com/watch?v=AmEaNAwFSfI